Nano Energy 133 (2025) 110447

Contents lists available at ScienceDirect

Nano Energy

journal homepage: www.elsevier.com/locate/nanoen

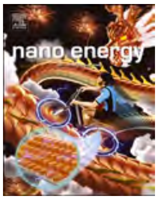

Structural engineering developments in sulfide solid-state electrolytes for lithium and sodium solid-state batteries

Mohammad Sufiyan Nafis [1], Zhiming Liang [1], Sehee Lee [*], Chunmei Ban [*]

Paul M Rady Department of Mechanical Engineering, University of Colorado Boulder, Boulder, CO 80309, USA

ARTICLE INFO

Keywords:
Energy storage
Solid-state electrolytes
Sulfide-based electrolytes
Solid-state lithium batteries
Solid-state sodium batteries
Argyrodite sulfides

ABSTRACT

Solid-state batteries (SSBs), especially those derived from lithium and sodium, show great promise as the next generation of energy storage devices due to their remarkable energy density, compact electrode architecture, nonflammability, and the use of metallic anodes. The solid-state electrolytes (SSEs), a significant part of SSBs, are essential to their functionality. A family of SSEs known as sulfide-based has been extensively studied for many years as a potential SSE for sodium and lithium SSBs. It offers excellent ionic conductivity, favorable mechanical properties, and ease of manufacturing. Notwithstanding its advantages, it also presents several problems, which require careful consideration for it to be successfully commercialized. This review summarizes the recent advancements in SSEs for lithium and sodium SSBs. It explores how structural engineering strategies impact the electrochemical properties of argyrodites SSEs for lithium SSBs and Na_3PS_4-based SSEs for sodium SSBs. The review provides comprehensive information on successful structural engineering approaches, such as introducing vacancies, mobile ions stuffing, and doping, for both lithium and sodium SSEs. It also discusses the air stability and electrochemical stability against electrodes, offering insights for designing and synthesizing next-generation SSEs that can lead to more durable and efficient energy storage systems.

1. Introduction

Lithium-ion batteries (LIBs) have significantly impacted on our daily routines due to the capability of providing portable electricity, lightweight nature, and environmentally considerate characteristics. Nevertheless, the safety-related necessity of utilizing materials with lower theoretical capacity in LIBs poses a challenge in meeting the growing requirements for electric vehicles and grid storage systems [1]. However, using high-capacity lithium metal anodes with non-aqueous electrolytes poses potential challenges, including flammability, risk of dendrite growth, and heat accumulation. These factors can lead to serious safety issues when LIBs are utilized in electric vehicles and portable devices [2–6]. All-solid-state batteries (ASSBs) stand out as one of the most promising competitors for the next generation of energy storage devices, allowing for the use of the metallic anodes, offering larger energy density, and posing a smaller safety challenge due to compact electrode architecture and the inherent nonflammability. The incorporation of the solid-state electrolytes (SSEs) significantly bolsters energy density, improves safety, enhances stability, offers a wider operating temperature range, and simplifies packaging [7–9].

Although ASSBs show promising potential as the next generation of energy storage, challenges such as low conductivity (both ionic and electronic), poor stability in ambient environments, and high materials fabrication cost still need to be addressed [10,11]. In the past decades, many types of SSEs have been developed for both lithium [12–15] and sodium [16–18] SSBs. These include oxides (e.g., LISICON, LLZO, LiPON, Na-ß-Al_2O_3, NASICON), sulfides (e.g., Li_3PS_4, Li_6PS_5Cl, Na_3PS_4, Na_2S-P_2S_5), polymers (e.g., PEO-Based, solvent-free polymer, ceramic fillers), and halides (e.g., Li_3InCl_6, $LiYCl_6$) *etc*. Tables 1 and 2 summarizes the developments of both lithium and sodium SSEs in the past decades. For example, lithium SSEs like LISICON [19–23], which is an oxide-type electrolyte, exhibit good electrochemical stability but has very low ionic conductivity at room temperature (RT), on the order of $\sim 10^{-5}$ S cm^{-1}. Similarly, perovskite-type electrolytes [24–29] such as $Li_{3x}La_{2/3-x}TiO_3$ ($x = 0.1$–0.5), have a poor ionic conductivity (10^{-6} S cm^{-1}) at RT and require extremely high synthesis temperatures of around 1200 °C [30]. LiPON electrolytes [31–34] show similar ionic conductivity to perovskite SSEs. In contrast, garnet-structure SSEs

---

[*] Corresponding authors.

E-mail addresses: sehee.lee@colorado.edu (S. Lee), chunmei.ban@colorado.edu (C. Ban).

[1] The authors contribute equally

https://doi.org/10.1016/j.nanoen.2024.110447
Received 30 August 2024; Received in revised form 23 October 2024; Accepted 1 November 2024

Table 1
Summary of representative lithium solid state electrolytes.

Type	Composition	Ionic Conductivity (RT)	Voltage *vs* Lithium
Oxides (LISICON)	$Li_{14}Zn(GeO4)_4$ [23]	$1.2*10^{-1}$ S cm^{-1} (300 °C)	-
	$Li_{3.5}Ge_{0.5}VO_4$ [21]	$4.0*10^{-5}$ S cm^{-1} (18 °C)	-
	$Li_{3.5}Si_{0.5}P_{0.5}O_4$ [76]	$1.0*10^{-6}$ S cm^{-1}	-
	$Li_{10.42}Si_{1.5}P_{1.5}Cl_{0.08}O_{11.92}$ [22]	$1.0*10^{-5}$ S cm^{-1}	0–9 V
	$Li_{10.42}Ge_{1.5}P_{1.5}Cl_{0.08}O_{11.92}$ [22]	$3.7*10^{-5}$ S cm^{-1}	0–9 V
	$Li_4Al_{1/3}Si_{1/6}Ge_{1/6}P_{1/3}O_4$ [77]	$9.0*10^{-4}$ S cm^{-1}	-
Oxides (Garnet)	$Li_5La_3Nb_2O_{12}$ [78]	$1.0*10^{-6}$ S cm^{-1}	-
	$Li_5La_3Ta_2O_{12}$ [78]	$1.0*10^{-6}$ S cm^{-1}	-
	$Li_6BaLa_2Ta_2O_{12}$ [79]	$4.0*10^{-5}$ S cm^{-1}	< 6 V
	$Li_7La_3Zr_2O_{12}$ [37]	$3.0*10^{-4}$ S cm^{-1}	-
	$Li_{6.4}La_3Zr_{1.4}Ta_{0.6}O_{12}$ [80]	$1.0*10^{-3}$ S cm^{-1}	0–5 V
	$Li_{6.25}Ga_{0.25}La_3Zr_2O_{12}$ [81]	$1.4*10^{-3}$ S cm^{-1}	-
	$Li_{6.20}Ga_{0.30}La_{2.95}Rb_{0.05}Zr_2O_{12}$ [41]	$1.6*10^{-3}$ S cm^{-1}	-
Oxides (Perovskite)	$Li_{0.34}La_{0.51}TiO_{2.94}$ [24]	$2.0*10^{-5}$ S cm^{-1}	-
	$LiSr_{1.65}Zr_{1.3}Ta_{1.7}O_9$ [82]	$1.3*10^{-5}$ S cm^{-1} (30 °C)	-
	$Li_{3/8}Sr_{7/16}Ta_{3/4}Zr_{1/4}O_3$ [83]	$2.0*10^{-4}$ S cm^{-1} (30 °C)	-
	$Li_{3/8}Sr_{7/16}Ta_{3/4}Hf_{1/4}O_3$ [84]	$3.8*10^{-4}$ S cm^{-1}	-
Sulfides (Glass)	$80Li_2S - 20\ P_2S_5$ (glass) [85]	$2.0*10^{-4}$ S cm^{-1}	-
	$80Li_2S-20\ P_2S_5$ (glass-ceramic) [85]	$9.0*10^{-4}$ S cm^{-1}	-
Sulfides (Ceramic)	$Li_{10}GeP_2S_{12}$ [86]	$1.2*10^{-2}$ S cm^{-1}	0–5 V
	Li_6PS_5Cl [87]	$1.3*10^{-3}$ S cm^{-1}	1.8 V – 2.3 V
	Li_6PS_5Br [88]	$6.6*10^{-3}$ S cm^{-1}	0–7 V
	Li_6PS_5I [89]	$3.6*10^{-7}$ S cm^{-1}	0–7 V
Polymer	PEO/LiTFSI+SiO_2 [43]	$1.0*10^{-5}$ S cm^{-1}	-
	PEO/$LiClO_4$+TiO_2 [44]	$1.4*10^{-4}$ S cm^{-1} (30 °C)	-
	PEO/LiTFSI+MOF−5 [45]	$3.1*10^{-5}$ S cm^{-1}	-
	PEO/$LiClO_4$+ $Li_{0.33}La_{0.56}TiO_3$ [90]	$1.0*10^{-3}$ S cm^{-1} (65 °C)	-
	PEO+$Li_{6.25}Ga_{0.25}La_3Zr_2O_{12}$ [91]	$7.2*10^{-5}$ S cm^{-1} (30 °C)	-
Halides	$Li_{2.5}Y_{0.5}Zr_{0.5}Cl_6$ [47]	$1.4*10^{-3}$ S cm^{-1}	-
	Li_3YbCl_6 [48]	$1.0*10^{-4}$ S cm^{-1} (300 °C)	-
	Li_3YBr_6 [49]	$2.2*10^{-3}$ S cm^{-1}	-
	Li_3ErI_6 [50]	$5.0*10^{-4}$ S cm^{-1}	-
	Li_3LaI_6 [92]	$1.1*10^{-3}$ S cm^{-1}	

Table 2
Summary of representative sodium solid state electrolytes.

Type	Composition	Ionic Conductivity (RT)	Voltage *vs* Sodium
Oxides (Al_2O_3)	Li_2O- β’’-Al_2O_3 [93]	1 mS cm^{-1}	-
	MgO-β/β’’-Al_2O_3 [94]	0.75 mS cm^{-1}	-
	β’’-Al_2O_3 [17]	2 mS cm^{-1}	-
Oxides (NASICON)	Zr_2O- β’’-Al_2O_3: Mg [95]	0.82 mS cm^{-1}	-
	$Na_3Zr_2Si_2PO_{12}$ [96]	0.67 mS cm^{-1}	< 6 V
	$Na_{3.4}Zr_{1.9}Zn_{0.1}Si_{2.2}P_{0.8}O_{12}$ [97]	5.27 mS cm^{-1}	< 6 V
	$Na_3Zr_{1.75}\ Mg_{0.25}Si_2PO_{12}$ [98]	2.4 mS cm^{-1}	< 6 V
	$Na_{3.3}Zr_{1.7}La_{0.3}Si_2PO_{12}$ [99]	3.4 mS cm^{-1}	-
	$Na_{3.3}Zr_{1.7}Lu_{0.3}Si_2PO_{12}$ [100]	0.83 mS cm^{-1}	-
	$Na_{3.3}Zr_{1.7}Eu_{0.3}Si_2PO_{12}$ [100]	1.08 mS cm^{-1}	-
	$Na_{3.3}Zr_{1.7}Pr_{0.3}Si_2PO_{12}$ [100]	1.27 mS cm^{-1}	< 5 V
	$Na_{3.1}Zr_{1.9}Ga_{0.1}Si_2PO_{12}$ [101]	1.06 mS cm^{-1}	< 5 V
	$Na_{3.4}Zr_{1.6}Sc_{0.4}Si_2PO_{12}$ [102]	4.05 mS cm^{-1}	< 6 V
Polymers	PEO-NaTFSI [103]	$4.5*10^{-3}$ mS cm^{-1}	-
	PEO-NAFSI [104]	$1.5*10^{-3}$ mS cm^{-1}	-
	PEO-NAFNFSI [105]	$2.0*10^{-3}$ mS cm^{-1}	-
	PEO-NATCP [106]	$6.9*10^{-2}$ mS cm^{-1}	-
	PEO-$NAPF_6$ [107]	$5.0*10^{-3}$ mS cm^{-1}	-
	PAN-$NACF_3SO_3$ [108]	0.73 mS cm^{-1}	-
	PVP-NaBr [109]	$1.36*10^{-3}$ mS cm^{-1}	-
	PVP-$NaClO_4$ [110]	$2.5*10^{-3}$ mS cm^{-1}	-
Sulfides	c-Na_3PS_4 [111]	0.2 mS cm^{-1} RT	1.39 V – 2.45 V
	Na_3SbS_4 [112]	2 mS cm^{-1} RT	1.45 V – 2.35 V
	$Na_{11}Si_2PS_{12}$ [113]	1.4 mS cm^{-1} RT	1.22 V – 2.21 V
	$Na_{11}Sn_2PS_{12}$ [114]	1 mS cm^{-1} RT	1.25 V – 2.25 V
	$Na_7P_3S_{11}$ [115]	10 mS cm^{-1} RT	-
	Na_4SiS_4 [116]	0.02 mS cm^{-1} RT	0.7 V – 2.2 V
	$94Na_3PS_4.6Na_4SiS_4$ [116]	0.74 mS cm^{-1} RT	-

[35–41], with a general formula of $Li_xM_3N_2O_{12}$ ($x = 3,5,6,7$; M = La, Y, Lu etc; N = Zr, W, Rb *etc*), demonstrate appreciable ionic conductivity ($\sim 10^{-4}$ S cm^{-1}) and a wide electrochemical voltage window, but they suffer from poor mechanical properties and high moisture sensitivity [42]. Polymer [43–46] SSEs offer good mechanical properties, high thermal stability, and a low elastic modulus, but their low Li^+ transference number, ionic conductivity, and poor stability with Li-metal hinder their commercialization. Halide SSEs [47–50] can achieve high RT ionic conductivity ($\sim 10^{-3}$ S cm^{-1}) and exhibit high oxidation stability against oxide cathodes, despite this, they face poor reduction stability with the Li-metal anode, higher grain boundary impedance, and sensitivity to air and humidity, which limit their large-scale use.

Similarly, the development of sodium SSEs encounters comparable challenges. As shown in Table 2, NASICON-type SSEs offer high conductivity ($\sim$1 mS cm^{-1}) due to their 3D migration pathways for Na^+ ions. However, NASICON SSEs face issues such as rough mechanical contact between electrode/electrolyte interface, leading to higher interfacial resistance, low interface conductivity ($\sim 10^{-5}$ S cm^{-1}) and severe dendritic growth, which limit their practicality [51,52]. Solid polymer electrolytes address some of these interfacial issues. A PVDF-gel polymer SSE demonstrates flexibility, easy production processes, and high ionic conductivity ($\sim 10^{-3}$ S cm^{-1}), but the Na^+ transference number is only 0.3, and gel presence raises safety concerns like leakage and volatilization [53–56]. These safety issues are mitigated by solvent-free solid polymer SSEs, although they offer very low ionic conductivity ($\sim 10^{-8}$ S cm^{-1}) at RT due to their dependence on the concentration of Na^+ ions, Na salts, and additives within the polymer matrix. Improvements can be made by incorporating polymer blends such as polyvinylpyrrolidone (PVP), plasticizers like succinonitrile (SN), or inorganic passive ceramic fillers such as TiO_2 and SiO_2 [57–60]. Ceramic-polymer composite electrolytes address conductivity issues by incorporating active ceramic fillers like NASICON, which provide higher ionic conductivity ($\sim 10^{-4}$ S cm^{-1}) compared to solvent-free polymer SSEs. However, their conductivity is highly dependent on the filler content and can suffer from agglomeration problems beyond the solubility limit [61–64]. A promising alternative for both lithium and sodium is the family of sulfide SSEs, which are favoured for their low-cost precursors, relatively easy synthesis procedures, good mechanical properties, and high ionic conductivity, making them the most promising candidates for ASSBs. For any SSEs to conduct mobile ions well, a few necessary conditions should be fulfilled. These include: (i) availability of sufficient vacant sites in the structure; (ii) presence of a good concentration of mobile ion charge carriers; (iii) a relatively similar energy barrier for the initial and transition states of the charge carriers; (iv) a favourable structure for ion transport, i.e., wider bottlenecks for ion migration and a softer lattice framework; and (v) high dimensionality of ion transfer pathways. Satisfying these conditions result in an optimal SSE. Sulfide SSEs stand out when compared to oxide-based systems, as they more effectively satisfy these structural requirements. For example, sulfide electrolytes generally exhibit ionic conductivities in the range of 10^{-3} to 10^{-2} S cm^{-1}, which is significantly higher than most oxide-based counterparts, making them highly favourable for practical applications. Additionally, sulfide-based SSEs can be synthesized at relatively low temperatures—sometimes as low as 300°C—which is much lower than typical oxide synthesis processes that require temperatures exceeding 1000°C [65,66]. This lower synthesis temperature makes sulfide electrolytes more cost-effective and scalable for commercial use. In terms of ion transport, sulfur atoms have lower electronegativity and binding energy to Li ions than oxygen atoms, which allows for increased ion mobility in the sulfide lattice. Furthermore, sulfur ions larger atomic radius results in wider pathways for Li ion conduction within the crystal structure, facilitating faster ion migration. Moreover, sulfide materials are softer and more malleable than oxides, allowing for dense packing through cold pressing, a process that minimizes grain boundary resistance by creating intimate particle contact. This unique mechanical property enables the fabrication of catholyte without a high-temperature sintering process, which is required for oxide SSEs. In terms of thermal stability, sulfide SSEs exhibit comparable stability to oxides. Compressed pellets of sulfide SSEs are thermally stable above 400 °C, effectively preventing melting and self-decomposition, as reported in numerous studies [67–71]. However, safety concerns at the interfacial and battery levels persist, especially when sulfide SSEs are paired with high-voltage cathodes (e.g., NMC811) and Li-metal anodes—issues that are also common with some oxide-based SSEs. Sulfide SSEs generally demonstrate cathode/SSE interface stability between 300 and 500 °C, slightly lower than oxides, which can withstand temperatures exceeding 500 °C. Despite this, sulfide SSEs remain stable within the operational temperature range of most battery applications. Additionally, the thermal runaway stability for both Li/Oxide and Li/Sulfide SSEs is comparable, typically around 300–400 °C [70]. This combination of high ionic conductivity, low synthesis temperature, and favourable structural and mechanical properties makes sulfide-based SSEs a very promising option for solid-state batteries.

Although sulfide SSEs demonstrate strong potential for commercialization due to their lower processing costs, higher softness, and improved ionic transport compared to other SSEs, they also have notable limitations as highlighted in the radar plots in Fig. 1. Their rate performance is constrained by a modest ionic conductivity of ~10^{-3} S cm^{-1}, which is insufficient for producing high-energy-density thick electrode cells. Moreover, the issues of dendritic growth, void generation and crack propagation, thickness of the SSE etc., are few notable limitations when compared to traditional liquid electrolytes. Additionally, their relatively low electrochemical stability (1.9 V–2.4 V) makes them particularly susceptible to interface reactions. These reactions can lead to poor long-term cycling stability, electrolyte oxidation at high voltages, breakdown of the crystal structure, and inadequate solid-solid ionic contact, among other issues if not properly addressed [72–75]. To support the community in better understanding strategies for

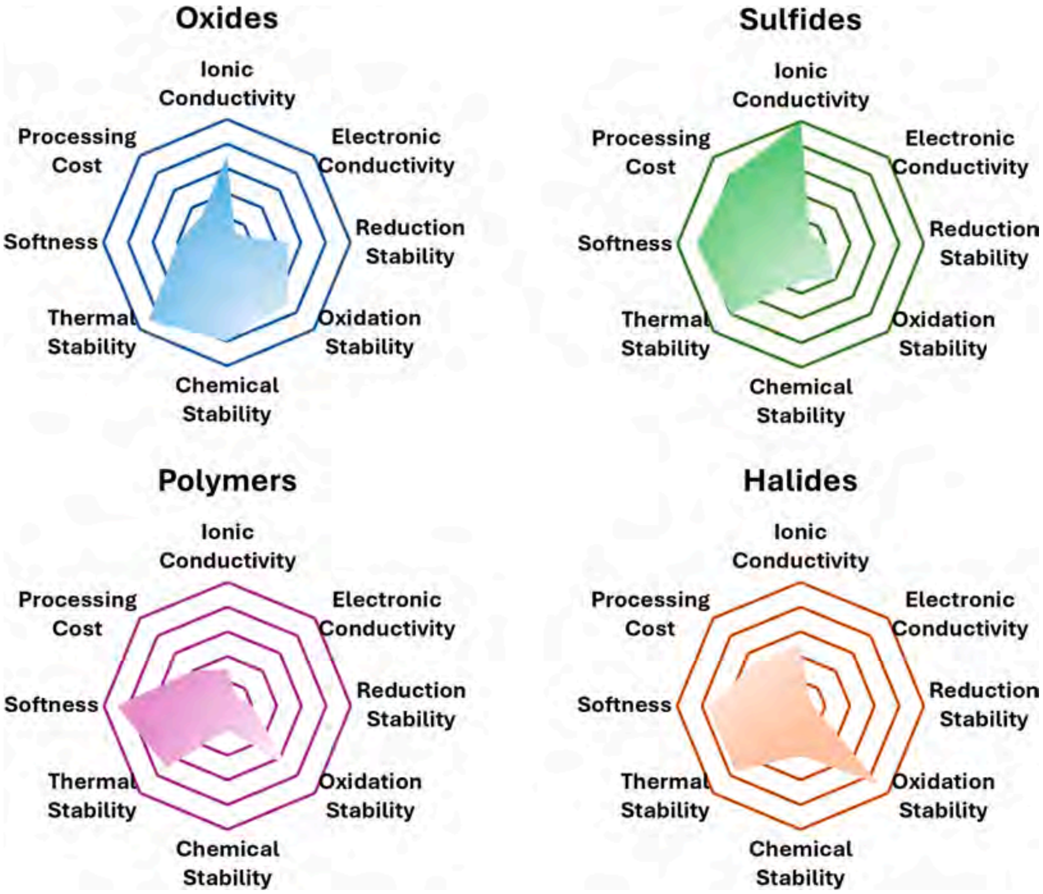

Fig. 1. Radar plots comparing oxide, sulfide, polymer, and halide SSEs across key characteristics, including ionic conductivity, electronic conductivity, reduction stability, oxidation stability, chemical stability, thermal stability, softness, and processing cost.

improving the performance of both lithium and sodium sulfide SSEs, this review thoroughly examines various approaches, including vacancy creation, excess mobile ion introduction, optimization of ion migration bottlenecks, the role of configurational entropy, and enhancement of lattice polarizability. These strategies are applied to enhance the conductivity, stability, and interfacial contacts of lithium and sodium SSEs. Through meticulous analysis, we elucidate the impacts of these strategies on the crystal structure and electrochemical performance of these SSEs.

2. Ion transport mechanisms in SSEs

SSEs, such as oxides, sulfides, halides, polymers etc., vary in structural compositions and the specific elements occupying different positions within the frameworks. Despite these differences, the fundamental ion transport mechanisms remain largely the same across these materials. Fig. 2a summarizes all the diffusion mechanisms that take place in the SSEs [117]. The interstitial mechanism involves ions moving through interstitial spaces within the lattice, without the need for vacancies. The vacancy mechanism operates when ions migrate into actual vacancies or missing ion sites, creating a chain-like movement as vacancies shift throughout the material. In the dissociative mechanism, an ion from the lattice dissociates into a mobile ion and occupies the existing vacant space to move through the structure. The concerted mechanism stands out by enabling multiple ions to move simultaneously in a coordinated manner, significantly reducing the energy barrier for ion transport and increasing ionic conductivity. The knock-off mechanism involves a mobile ion displacing another from its position, causing a cascading effect where the displaced ion moves into an adjacent site. Lastly, the interstitialcy mechanism combines aspects of interstitial and knock-off mechanisms, where the interstitial ion does not move directly from one interstitial site to another but instead displaces a regular lattice ion into an interstitial position, taking its place in the lattice and the newly formed interstitial ion creates a continuous cycle of movement. This mechanism exhibits lower activation energies as interstitial ions are formed that can navigate through pre-existing interstitial sites. In SSEs, the transport of mobile ions like Li^+ or Na^+ is a fundamental process dictating the electrochemical performance of ASSBs. Before migration, these ions reside in well-defined crystallographic sites, such as octahedral, tetrahedral, or other coordination sites determined by the electrolyte's crystal structure. These sites are termed as low-energy stable sites. The initiation of ion migration is driven by a combination of thermal energy, applied electric fields, and concentration gradients, all of which contribute to overcoming the potential energy barriers that restrict ion mobility. These barriers are associated with the lattice structure but also with electrostatic interactions between the mobile ions and the surrounding ions within the electrolyte matrix. Mobile ions must overcome the electrostatic forces exerted by neighbouring ions as well as the inherent lattice energy (stability of the crystallographic sites they occupy). This electrostatic energy represents a significant portion of the activation energy required for migration, as it opposes the movement of the ion from its stable site. As ions migrate, they transition through a series of unstable or partially stable intermediate positions, where the electrostatic environment is less favourable. These intermediate states are typically higher in energy, requiring the mobile ion to possess sufficient kinetic energy to escape the attractive forces binding it

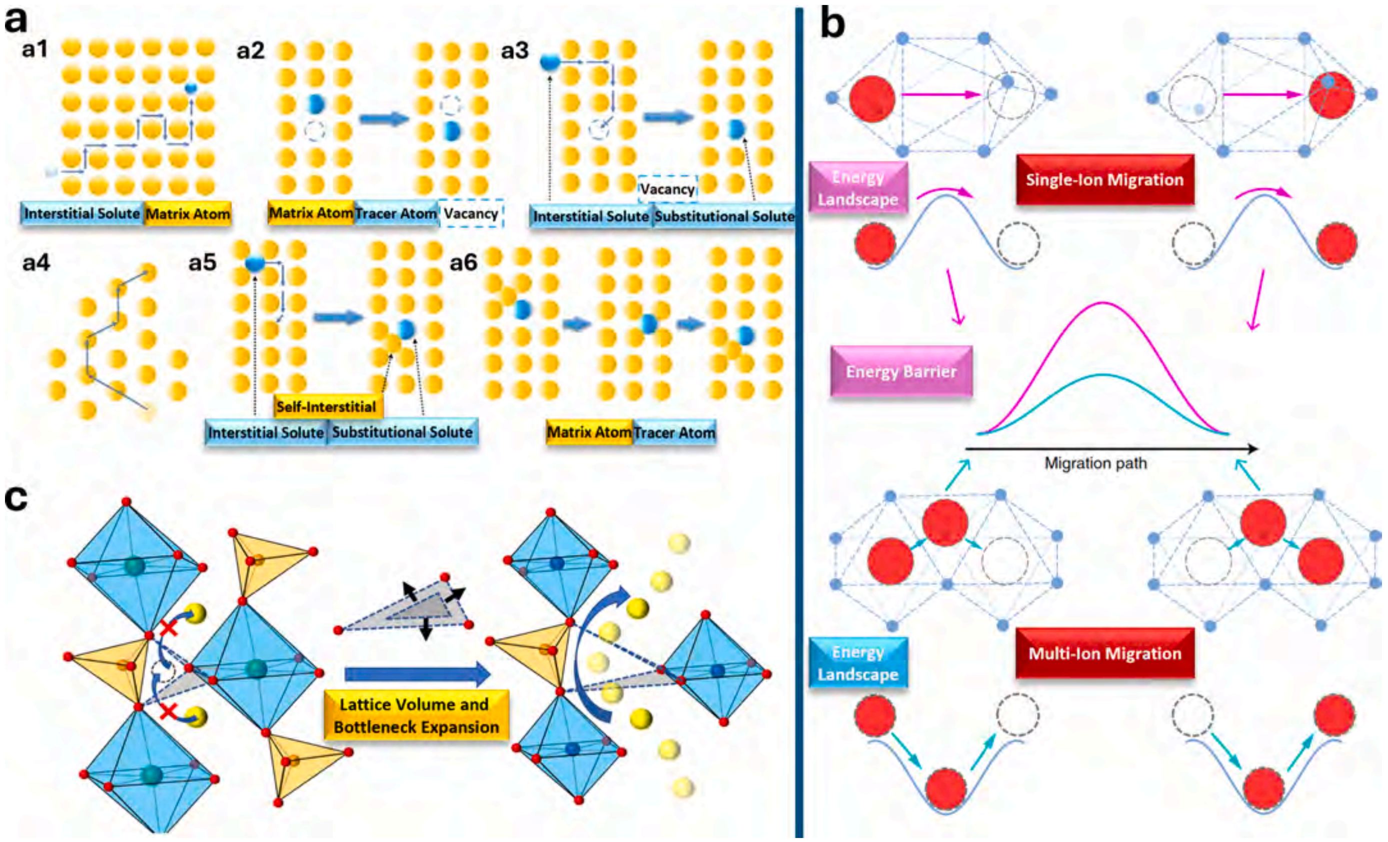

Fig. 2. (a) Ion transport mechanisms illustrated include: a1) Direct interstitial mechanism; a2) Vacancy mechanism; a3) Dissociative mechanism; a4) Concerted mechanism; a5) Knock-off mechanism; and a6) Interstitialcy mechanism. (b) Representation of ion migration pathways and corresponding activation energies for single-ion migration and multi-ion migration. (c) Illustration depicting the impact of static structural changes, such as lattice expansion, on the bottleneck region affecting ion hopping pathways.

(a) Reproduced with permission from [117], copyright 2010, Springer. (b) Reproduced with permission from [118], copyright 2017, the authors. (c) Reproduced with permission from [119], copyright 2023, Royal Society of Chemistry.

to its initial position. The following section discusses the two modes of ion migration: single-ion migration and multi-ion migration.

2.1. *Single-ion migration and multi-ion migration*

In SSEs, ion migration can occur through mechanisms known as single-ion and multi-ion migration. These processes involve the dissociation of ions from their stable low energy lattice position, allowing them to move through the inter-connected diffusion channels of the crystal structure. Ions can migrate via two principal pathways: vacancy diffusion and interstitial diffusion. Vacancy mechanism heavily relies on the availability of vacancies, which can be either naturally occurring or introduced through controlled doping. The activation energy required for this process is relatively high, as ions must overcome both their bonding energy and the energy barrier to migrate to adjacent vacant site through high energy intermediate state. On the other hand, interstitial diffusion tends to be more favourable in materials with a more loosely packed structure, where ions can easily occupy and move through available interstitial sites. As depicted in Fig. 2b top, single-ion migration requires high activation energy and limits the overall ionic conductivity. Whereas, the multi-ion migration, as presented by He *et al.* [118], describes the simultaneous movement of multiple ions in a synchronized manner, enabling more efficient traversal of the lattice. Multi-ion migration, also referred to as concerted migration, is significantly accelerated by increasing the concentration of mobile ion charge carriers within the sublattice. Initially, the lower energy sites, such as tetrahedral sites, are filled with the required number of mobile ions before migration occurs. Once these low-energy sites are saturated, any excess mobile ions are accommodated in intermediate high-energy metastable sites. As the mobile ions residing in these high-energy positions migrate downhill, they impart energy to the ions located in the low-energy sites, facilitating their uphill migration. This cooperative mechanism effectively triggers low energy barrier concerted migration (Fig. 2b bottom), resulting in enhanced ion transport efficiency within the solid-state electrolyte.

2.2. *Factors influencing ion mobility*

2.2.1. *Lattice expansion and contraction*

Lattice expansion and contraction are static structural features induced by doping an SSE with atoms that differ in size from the parent atom. This phenomenon alters the free volume within the lattice, facilitating the hopping of mobile ions to different sites. During discussions of lattice changes, the term "bottleneck region" is frequently employed to describe a triangular zone formed by three anions, which presents the highest activation energy barriers for mobile ion migration. Consequently, it is crucial to widen diffusion pathways and bottlenecks to promote low-barrier ion migration. Fig. 2c illustrates a schematic representation of unobstructed mobile ion migration facilitated by larger bottleneck sizes. However, designing a SSE with optimal static structural features is not a straightforward task. A finely tuned lattice must be developed, exhibiting appropriately sized diffusion bottlenecks and suitable concentrations of mobile ions. Moreover, the simultaneous doping of both cations and anions complicates efforts to distinguish which factors contribute positively or negatively to the performance of SSEs. In addition to these static properties, the continuous oscillation of skeletal anions affects the SSEs structural composition and can successfully lower the activation energy, mostly observed for anions that are larger and more polarizable. For instance, the energy barrier for Li^+ ions can be reduced in Li_6PS_5Cl when S^{2-} ions are substituted for larger and more polarizable Se^{2-} or Te^{2-} ions that creates a softer lattice [120]. Similar trend to Na^+ ion migration is also noticed in Na_3PS_4 [121]. Ultimately, understanding the interplay between static structural features and dynamic anion behaviours is essential for optimizing the design of SSEs, enabling enhanced ionic conductivity and improved performance in electrochemical applications.

2.2.2. *Polyanion rotation*

A significant portion of the understanding around robust mobile ion conduction has traditionally been based on static structural analysis, as outlined in the previous section. However, recent studies have introduced a new perspective, highlighting the critical role of cation-anion interactions within the lattice. Specifically, the "paddle-wheel mechanism" has been identified, which illustrates how the rotational dynamics of anions can enhance and facilitate cation movement [69,123–125]. A significant link between cation diffusional motion and the rotational dynamics of polyanions, such $[PS_4]^{3-}$ and $[PSe_4]^{3-}$, has been found in recent investigations on a novel class of crystalline polyanion-based $Na_{11}Sn_2PnX_{12}$ materials (where Pn = P, Sb and X = S, Se), known as the "NSPS" structure. A comprehensive study done by Zhang et al. [122] using maximum entropy method (MEM), neutron powder diffraction (NPD), and ab-initio molecular dynamics (AIMD) simulations, delved directly into understanding the rotation of the PnX_4^{3-} polyanions. Fig. 3a shows the nuclear density plots of $Na_{11}Sn_2PS_{12}$ along the (100) planes at axis z = 1/8. The $[PS_4]^{3-}$ tetrahedra is highlighted in blue, and in yellow are four maxima (S1a, S2a, S3a, S4a) around the initial S atom. Four additional maxima are observed (S1b, S2b, S3b, S4b) that are caused because of the rotation of $[PS_4]^{3-}$ polyanionic group. The MEM 2D plots at temperatures 3 K, 300 K, and 450 K are shown besides the nuclear density plots in Fig. 3**a**. Even at cryogenic temperatures of 3 K, static patches of high density (red) are still easily visible, suggesting a stationary reorientation of the $[PS_4]^{3-}$ units. On the other hand, the spherical distribution of the spread sulfur density at 300 K (RT) and 450 K indicates dynamic rotation of these $[PS_4]^{3-}$ units [126]. In contrast to this, very low intensity and localized anions reorientation of the $[SbS_4]^{3-}$ were visible in the less conductive analogue of $Na_{11}Sn_2SbS_{12}$ [127,128]. For $[SbS_4]^{3-}$, a slight but noticeable rotation was seen at higher temperatures of 300 K and 450 K, suggesting a higher temperatures requirement to activate rotation. The corresponding Helmholtz free energy surfaces of $[PS_4]^{3-}$, $[PSe_4]^{3-}$, $[SbS_4]^{3-}$ are shown in Fig. 3b. The rotation pathways and barriers are represented by the locations and heights of the local minima and transition states, respectively. A larger depth of the potential walls is calculated for $[SbS_4]^{3-}$ that corresponds to a high rotational barrier of 0.60–0.86 eV. Whereas the $[PS_4]^{3-}$ and $[PSe_4]^{3-}$ shows a low rotational energy barrier of 0.12–0.24 eV. The low rotational barrier of $[PS_4]^{3-}$ and $[PSe_4]^{3-}$ could also be a function of more covalent nature of P-S and P-Se bonds compared to Sb-S and Sb-Se bonds. Understanding the role of anion rotation, or the paddle-wheel effect, becomes increasingly valuable when it is associated with cationic motion in solid-state electrolytes (SSEs). AIMD simulations in Fig. 3c demonstrates a strong correlation between the rotation of $[PS_4]^{3-}/[PSe_4]^{3-}$ anions (indicated by red arrows) and Na^+ ion migration (represented by green arrows). This rotational movement introduces intrinsic disorder, and momentarily enlarges the triangular bottleneck to cationic motion of Na^+ ions residing within the octahedral cages along the diffusion pathways. This lowers the energy barrier and enhances cation mobility in $Na_{11}Sn_2PX_{12}$ (X = S, Se). Similar AIMD results for $Na_{11}Sn_2SbS_{12}$ are shown in Fig. 3d, however, no signs of polyanionic rotation are visible and neither the S ligands nor Na^+ cations are found to linger near each other, leading to trapping of Na^+ ions due to high energy barriers. This leads to poor diffusion, higher activation energy, and much lower ionic conductivity in $Na_{11}Sn_2SbS_{12}$. In the Fig. 3e, a larger triangular bottleneck area for cationic migration is evident for $Na_{11}Sn_2PS_{12}$ thus indicating robust performance [129,130].

The concept of paddle-wheel mechanism has also been observed in both Li and Na SSEs. A very high conducting $Li_{10}GeP_2S_{12}$ SSE was proposed to display some reorientation of the $[PS_4]^{3-}$ from the AIMD simulations of [86]. In the argyrodite class of Li SSEs that are high conducting, the ^{31}P nuclear magnetic resonance (NMR) displayed the rotation of the tetrahedrons, which was linked to their robust diffusion characteristics [131]. Apart from the sulfides, the Li and Na halides SSEs such as Li_3InX_6 (X = Cl, Br, I) and Na_3SCl_6 (S = Er, Y) have also shown

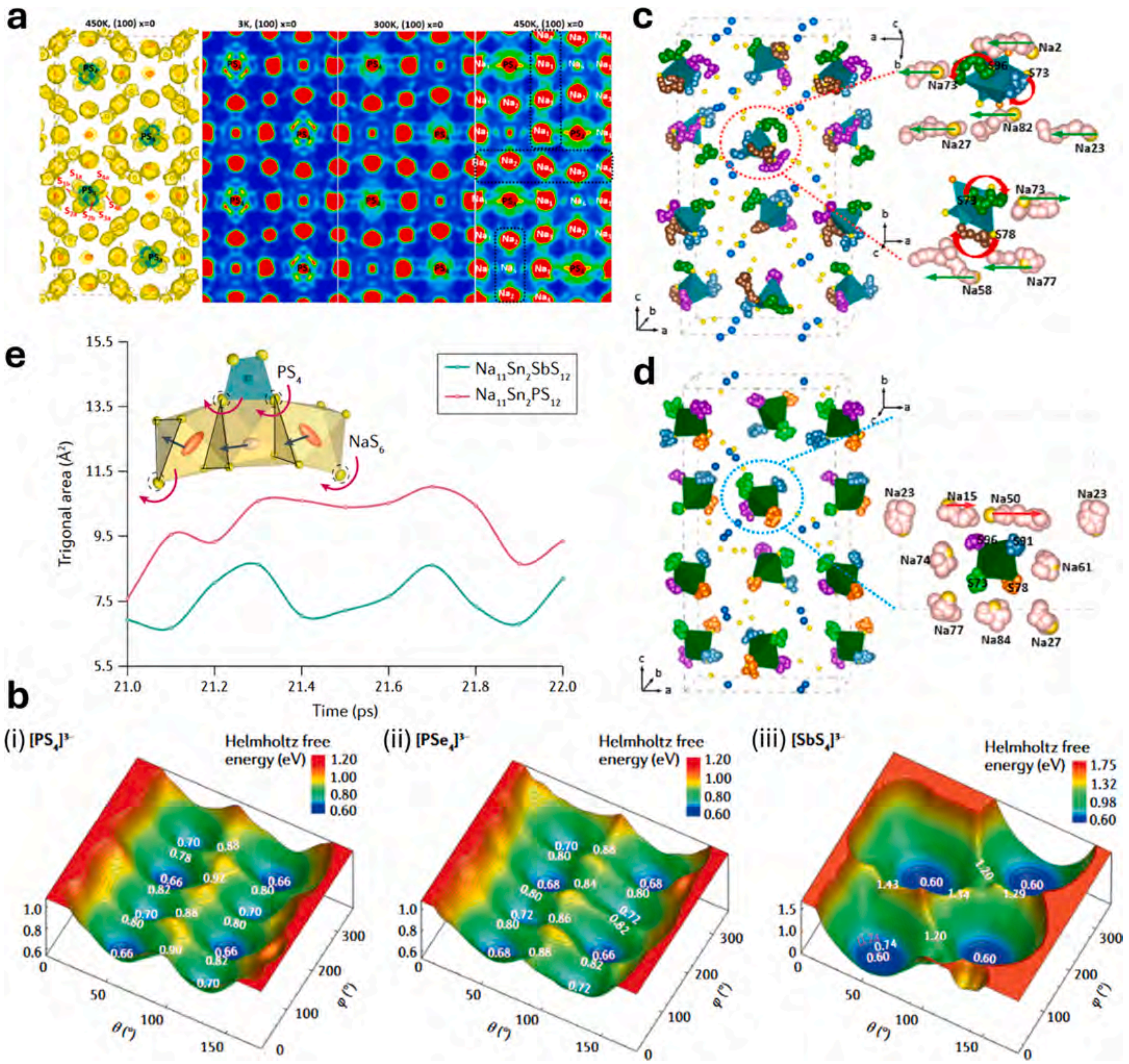

Fig. 3. (a) Nuclear density plot of $Na_{11}Sn_2PS_{12}$ obtained along the (100) plane at x = 0 at 450 K. Alongside are the 2D MEM plots displaying nuclear density at 3 K, 300 K, and 450 K, with red representing regions of high density and green for low density. (b) Helmholtz free energy surfaces as a function of θ and φ in degrees. The free energy surfaces of different groups are represented as: (i) $[PS_4]^{3-}$ group of $Na_{11}Sn_2PS_{12}$, (ii) $[PSe_4]^{3-}$ group of $Na_{11}Sn_2PSe_{12}$, and (iii) $[SbS_4]^{3-}$ group of $Na_{11}Sn_2SbS_{12}$ SSE. The formula for the calculation of the Helmholtz free energy A is $A(\theta, \varphi) = -k_BT\ln[\rho(\theta, \varphi)]$, where k_B is the Boltzmann constant, T is temperature, and $\rho(\theta, \varphi)$ is the probability density distribution of the S/Se ligands of $[PS_4]^{3-}$, $[PSe_4]^{3-}$, $[SbS_4]^{3-}$ anions from the AIMD simulations. (c) AIMD simulations elucidating the impacts of anion rotation on cationic motion for $Na_{11}Sn_2PS_{12}$ and (d) $Na_{11}Sn_2SbS_{12}$. The projection of a snippet on the right panel indicates the motion of Na cations in concerted manner (green arrows) and rotation of the $[PS_4]^{3-}$ anions group (red arrows). For the case of $Na_{11}Sn_2SbS_{12}$, no rotation of the $[SbS_4]^{3-}$ tetrahedron is observed and mobile Na ions, indicated by red arrows, do not come near the sulfur ions that are shown in yellow and orange colours, thereby leading to local trapping of the Na ions. (e) The size of the triangular bottleneck region for Na ion transport for both the SSEs. Enlargement of the bottleneck size for $Na_{11}Sn_2PS_{12}$ is evident (~11 Å^2), while $Na_{11}Sn_2SbS_{12}$ shows a smaller bottleneck region causing hinderance to cationic motion. Reproduced with permission from [122], copyright 2019, American Chemical Society.

these characteristics [132,133]. The NCl_6 (N = In, Er, Y) polyhedrons in both the Li and Na types have indicated rotational motion with different onset temperatures. Collectively, these findings emphasize the critical role of anion dynamics in enhancing ionic conductivity across a diverse range of solid-state electrolytes.

3. Structure engineering of lithium argyrodite SSEs

Sulfide SSEs are becoming promising candidates for the ASSBs due to their advantages seen above. The typical sulfide SSEs include glassy Li-P-S (LPS) sulfides [28], ceramics obtained from LPS sulfides [29], argyrodites (Li_6PS_5X) [30], thio-LISICONs [24], and $Li_{10}GeP_2S_{12}$ (LGPS) compounds [16,31]. Among the glassy LPS compounds, the binary *x*Li_2S.(100-*x*)P_2S_5 compound are well studied. Lower Li_2S concentration (x<60) LPS compounds show more di-tetrahedral $P_2S_7^{4-}$ units with one bridging S atoms and three terminal S atoms. Higher Li_2S amounts (x>70), typically glassy $75Li_2S.25P_2S_5$, only shows PS_4^{3-} units and highest conductivity of 0.28 mS cm^{-1} at RT [21,39]. Ceramic sulfides also evolve from the LPS system after heat treatments such as $Li_7P_3S_{11}$ (70Li2S·30P2S5), Li_3PS_4 ($75Li_2S·25\ P_2S_5$), Li_7PS_6 ($88Li_2S·12\ P_2S_5$), and $Li_4P_2S_6$ ($67Li_2S·33\ P_2S_5$) [134,135]. Ionic conductivity is largely a function of the composition of the binary compounds and their heat treatment synthesis protocols as these give rise to metastable crystalline phases that are ionically conducting. For instance, synchrotron XRD revealed the crystalline phase generated from $70Li_2S·30\ P_2S_5$ glass to be $Li_7P_3S_{11}$ after heat treating at 531–633 K. It had a triclinic cell and a space group *P-1*, with an ionic conductivity of 1 mS cm^{-1}. Another class, namely thio-LISICON, are also formed from the binary/ternary systems of Li_2S-GeS_2, Li_2S-GeS_2-ZnS, and Li_2S-GeS_2-Ga_2S_3. In these compounds, the Ge, Zn, Ga atoms occupy the tetrahedral sites, S atoms in the hexagonal close packing, and Li atoms in the octahedral sites. While the possible SSEs from these compounds are Li_2GeS_3, Li_4GeS_4, Li_2ZnGeS_4 etc., they do not feature sufficient conductivity [136]. However, aliovalent substitution of P^{5+} to prepare crystalline thio-LISICON $Li_{4-x}Ge_{1-x}P_xS_{4-x}$ (space group $P2_1/m$) can increase the conductivity to 2.2 mS cm^{-1} for (x = 0.75) [86]. The very famous tetragonal $Li_{10}GeP_2S_{12}$ (LGPS) compounds (space group $P4_2/nmc$) are also derived from the binary systems of (1-*x*)Li_4GeS_4-*x*Li_3PS_4 (0.5<*x*<0.67), similar to used in crystalline thio-LISICON [137]. The structure of LGPS has MS_4 (M = Ge, P) tetrahedra along the a and b axes. 1D conducting chains are formed by LiS_6 octahedra and edge sharing $(Ge_{0.5}P_{0.5})S_4$ tetrahedra. LiS_4 further helps interconnect this chain to form 1D Li conduction in the c-axis. LGPS SSE possess a high conductivity of 12 mS cm^{-1} at RT, 1 mS cm^{-1} at −30 °C, and 0.4 mS cm^{-1} at −45 °C. Despite these advantages, the LGPS and crystalline thio-LISICON systems possess high material costs due to the presence of Ge metal. Complete or partial substitution of Ge atom by Sn and Si to produce $Li_{10}SnP_2S_{12}$, $Li_{10}Sn_{0.7}Si_{0.3}P_2S_{12}$ has helped reduce material cost and maintain good conductivity [138,139]. In the Si-based LGPS-type structure ($Li_{11}Si_2PS_{12}$), the $Li_{9.54}Si_{1.74}P_{1.44}S_{11.7}Cl_{0.3}$ SSE possesses an exceptional conductivity of 25 mS cm^{-1}, which is attributed to the 3D conduction and extra Li ions located on the interstitial 16 *f*, 8 *f*, and 4*c* sites.

The final type of Li sulfide SSE is the argyrodite type, which is also the subject of this review, with the formula Li_6PS_5X (X = Cl, Br, I). It has a cubic structure (space group F43 *m*) with five different tetrahedral sites (Section 3.1) that enable 3D Li-ion conduction through face-sharing tetrahedral sites. While the superconducting LGPS-type structure possesses a BCC framework that allows easier migration through face-sharing tetrahedral sites, it supports only 1D conduction, which is inferior to the 3D conduction offered by the argyrodite structure. Additionally, argyrodites typically have favourable mechanical properties, allowing them to accommodate volume changes during cycling and reduce dendrite growth. Their 3D conduction also results in lower interface resistance, improving overall cell efficiency. Argyrodite structures can be easily doped with various elements, enabling tuneable ionic conductivity and enhanced stability without the use of expensive metals, as seen in LGPS [140]. Unlike the high material cost of Ge in potential counterparts, argyrodite offers high RT conductivity of 2 mS cm^{-1} in its pristine form and remains cost-effective and scalable for large-scale production. Overall, these features make the argyrodite structure a superior choice for SSEs compared to LGPS and other alternatives.

3.1. *Structures of lithium argyrodite SSEs*

Argyrodites, classified as ceramic structures, particularly Li_6PS_5X (X = Cl, Br, I), have garnered significant attention due to their distinctive crystal structures. These argyrodites are synthesized by substituting the chalcogenides in Ag argyrodite compounds (Ag_8GeS_6) with halogen [144]. In the pristine argyrodite structure, halide ions (Cl, Br, I) form a face-centered cubic (FCC) lattice, fully occupying all corner and face-centered positions, corresponding to the Wyckoff *4a* sites. When there is anion disorder between chalcogenide and halide ions, the halide ions can partially occupy the Wyckoff *4d* sites, as depicted in Fig. 4a [145,146]. All octahedral voids at the edge-centered positions are occupied by phosphorus ions, labelled as Wyckoff *4b* sites. These phosphorus ions further form PS_4^{3-} tetrahedra with sulfur ions located at the Wyckoff *16e* sites. Additionally, sulfur ions occupy half of the tetrahedral voids, which are also referenced by Wyckoff *4d* sites [135,147]. Within the anionic framework of Li_6PS_5X, there are 132 tetrahedral interstices per unit cell that can accommodate the 24 lithium ions. These interstices are condensed into five distinct tetrahedral lithium sites, determined by their interaction with the PS_4^{3-} tetrahedra as shown in Fig. 4a. These lithium sites are primarily formed around the free sulfur atoms at Wyckoff *4d* sites. In Li_6PS_5X (X = Cl, Br, I) stoichiometry, the occupancy of Cl atoms is partially shared between *4a* (39 %) and *4d* (62 %) sites due to a significant anions disorder. For Br substitution, the atoms are dispersed throughout the *4a* (78 %) and *4d* (22 %) sites, with the *4d* sites having lower occupancy compared to Cl. In I substituted Li_6PS_5I, the atoms solely occupy the *4a* sites due to the absence of any disorder [148]. The impact of this anions site disorder on the microscopic lithium mobility is very well explained by Minafra *et al.* [142]

From the molecular dynamics (MD) and density functional theory (DFT) simulations, the lithium mobility in Li_6PS_5Cl is seen to occur at different time and length scales that are classified into three distinct types of transitions [89,140]. These three transitions have activation energies between 0.2 and 0.3 eV. The overall conductivity of the SSE is limited by the transition having the highest activation energy (0.3 eV), which is also referred to as the rate-limiting transition of lithium ions. The transition of Li^+ ions is majorly understood from their jumps from the type 5 (*48 h*) site to type 5a (*24 g*) sites. These three transitions are classified as doublet jumps, intra-cage jumps, and inter-cage jumps. Doublet jumps are also called as the back and forth jumps within the same lithium cage as they involve Li motion between the face sharing tetrahedra of type 5 via the type 5a Li site. Intra-cage jumps involve Li jumps from one non-face sharing type 5 tetrahedra to another non-face sharing type 5 tetrahedra within the same Li cage centred around the *4d* sulfur atom. The inter-cage jumps involve Li motion from one type 5 cage to another type 5 cage centred around different *4d* sulfur atoms. The inter-cage jumping is the rate-limiting transition with highest energy barrier as it involves a difficult Li migration occurring across non-face sharing tetrahedra. Minafra *et al.* [142] investigated the role of non-type 5 Li sites in Li migration for Li_6PS_5X (X = Cl, Br, I) using NPD and Rietveld refinements. A new Li site at type 2 (*48 h*) was found for argyrodite samples containing Cl and Br as shown in Fig. 4a. The Li occupancy on this new T2 site increases as a function of temperature, while it decreases on the T5 site as shown in Fig. 4b. The concentration of Li occupation on these new T2 sites are directly related to the halide ion present in the lithium argyrodites. LPSI shows no T2 site occupancy, LPSCl shows moderate T2 site occupancy, while LPSBr shows highest T2 site occupancy as seen in Fig. 4b. T2 sites also promote improvement in the network of Li cages. Fig. 4c shows the importance of a T2 site in acting as an intermediate path along the intra-cage and inter-cage lithium jumps. T2 site helps in intra-cage motion by connecting two T5 sites within the same cage to form a continuous network for Li movement. Similarly, a pair of T2 sites help connect the T5 site in different cages. Thus, the revised motion of Li ions in intra-cage is T5-T2-T5 instead of older T5-T5 motion. Similarly, for inter-cage it is T5-T2-T2-T5 motion. However, the presence of T2 sites by itself is not beneficial for higher conductivity, rather it is also dependent on the T2-T2 jump distances. The T2-T2 jump distance for X = Cl was found to be significantly smaller due to higher anions disorder compared to X = Br, as also reported previously. This is consistent with the higher conductivity in the Li_6PS_5Cl as the inter-cage jumps are more likely to happen in this stoichiometry [149]. To gain more insights into the three

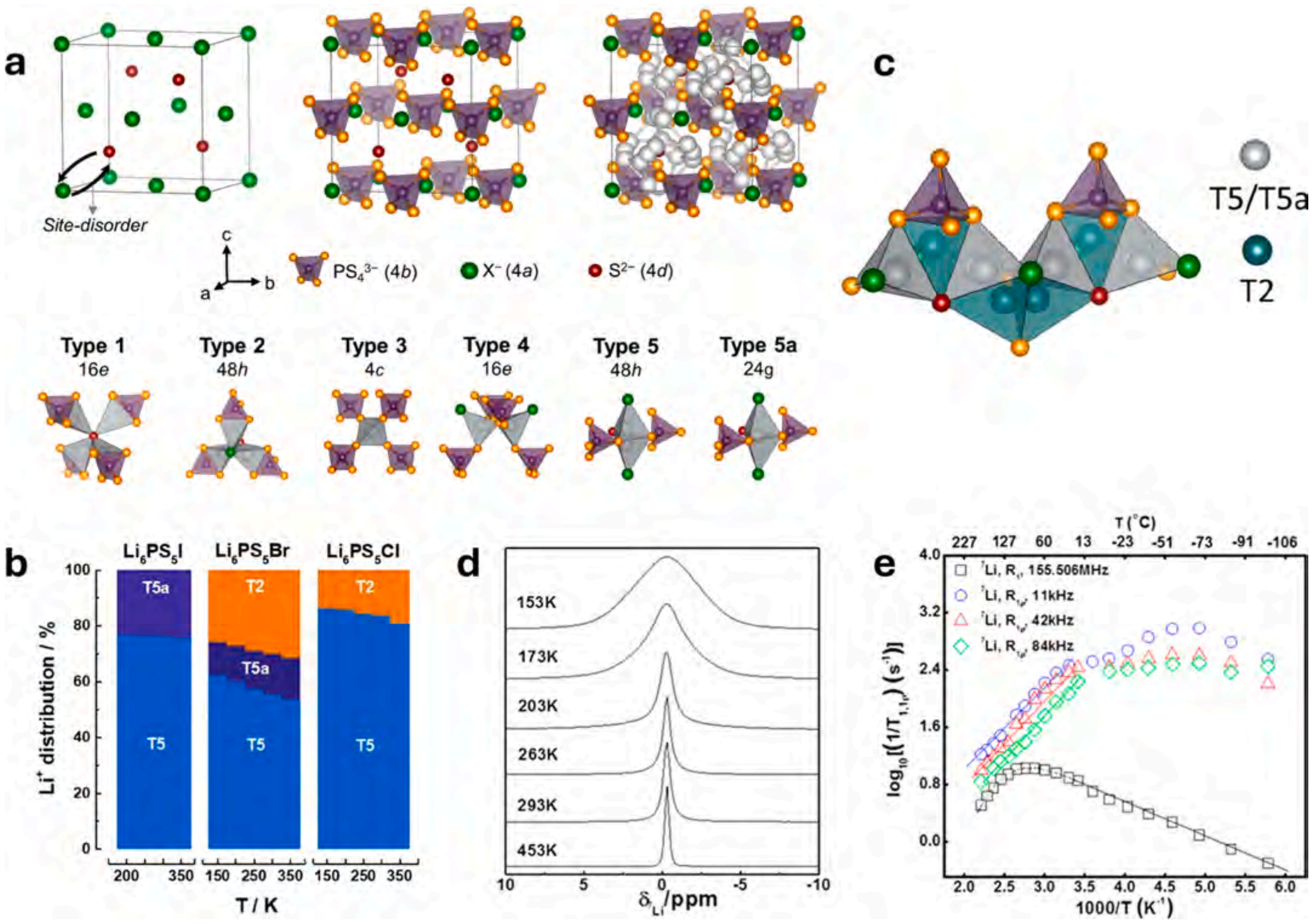

Fig. 4. (a) Unit cell and crystal structure of cubic symmetry argyrodite-type Li_6PS_5X crystallizing in space group F43 *m*. (b) Lithium distribution for Li_6PS_5X on the T5, T5a, and T2 sites, as a function of temperature. (c) Schematic of efficient lithium migration achieved with the presence of a new T2 site. (d) Li_6PS_5Cl motional narrowing curves for the static ^{7}Li NMR resonance. (e) SLR NMR rates for ^{7}Li, recorded in the rotating ($R_{1\rho}$) and the laboratory (R_1) frame of reference. The locking frequencies are 11, 42, and 84 kHz, respectively, while the Larmor frequency is 155.506 MHz.

(a) Reproduced with permission from [141], copyright 2021, American Chemical Society. (b-c) Reproduced with permission from [142], copyright 2020, American Chemical Society. (d-e) Reproduced with permission from [143], copyright 2016, American Chemical Society.

transition jump distances, Schlenker *et al.* [150] studied differential bond valence and MEM. Consistency of the bond valence method with MD simulations was observed [143]. They evaluated the site distances as: $d_{T5\text{-}T5a} = 1.46$ Å (doublet jump), $d_{T5\text{-}T2} = 2.03$ Å (intra-cage distance), $d_{T2\text{-}T2} = 1.31$ Å (inter-cage distance)

To understand the diffusion mechanisms, Yu *et al.* [143] utilized NMR spin-lattice relaxation (NMR-SLR) experiments coupled with MD simulations approach to gain insight into the bulk and interface Li-ion mobility in lithium argyrodites. NMR is a more accurate technique than EIS as it is more sensitive to local-scale mobility unlike EIS, which is to global mobility. It also has the advantage of being a non-destructive and contactless technique [151]. They measured the rates at the laboratory frame ($1/T_1$) and rotating frame ($1/T_{1/\rho}$). The laboratory frame is used to find out the jump frequencies of local Li-ions and the respective activation energy, whereas the rotating frame is used to get insights in the long-range Li^+ motion [152–154]. Fig. 4d indicates the motional narrowing of the static ^{7}Li NMR resonance with the increase in temperature of Li_6PS_5Cl. This is an indication of the high mobility at higher temperature as these Li-ions can cancel out the dipolar interactions effectively. From Fig. 4e, the NMR-SLR $1/T_1$ rates are asymmetric in the low and high temperature limit (R_1 data points in square boxes), which was also reported in the literature [150,155]. This reflects the Li-ionic motion happening at different length scales as a function of temperature, a feature also evident from the MD simulations. At the laboratory frame, the maximum SLR rate $1/T_1$ occurs at 345 K with a Larmor frequency (ω_0) of $\omega_0/2\pi = 155$ MHz. This corresponds to a Li^+ ion jump frequency of $9.8*10^8$ Hz. Low temperature region indicates the short-range motion whereas the high temperature reflects the long-range process. The activation energies calculated from the slopes of the SLR rates are 0.09 eV (short range) and 0.29 eV (long range), which are very close to the one reported by Schlenker *et al.* [150] from their NMR study. From the activation energy for the long range, its jump frequency can be calculated as $2*10^{13}$ Hz, at 345 K, which is like the one predicted by MD simulations. Diffusion coefficient can be calculated from the jump frequency using the Einstein Smoluchowski equation and the activation energy values [156,157]. Calculated diffusion coefficient at 298 K was $2.5*10^{-12}$ m^2 s^{-1}. Further, from Nernst-Einstein equation and the diffusion coefficients, the ionic conductivity of Li_6PS_5Cl using NMR can be calculated to be 3.9 mS cm^{-1} [117,158]. This value is near to the conductivity value of 3.4 mS cm^{-1}, calculated from the EIS and verified by other values in literature [87,88,143,147]. In the SLR rotating frame, the maximum jump rates calculated at the lock frequencies of 11, 42, and 84 kHz for the condition of $\tau_{1p}\omega_{lock} = 0.5$, are 1.38×10^5 Hz (at 200 K), 5.3×10^5 Hz (at 215 K), and 1.06×10^6 Hz (at 220 K), respectively. At 200 K, the jump frequency based on the $1/T_1$ relaxation rate is $7.4*10^5$ Hz, a value very close to the jump frequency calculated from the $1/T_{1/p}$ relaxation rate of $\omega_{lock} = 11$ kHz for the same temperature of 200 K, which is $1.38{*}10^5$ Hz. Good agreement between $1/T_1$ and $1/T_{1/p}$ results indicates the jump process observed in $1/T_1$ (local-hopping) measurements are also responsible for the long-range transport of Li^+ ions [150]. Additionally, most of the grains are captured in the long-range transport probe, which naturally also includes the grain boundaries. Consequently, the strong correlations between the $1/T_1$ and $1/T_{1/p}$ pair of findings also suggest that grain boundaries within the material have minimal effect on Li^+ transport in Li_6PS_5Cl.

3.2. Halogen site substitutions

One simple method to improve SSEs is by substituting halogen atoms (e.g., Cl, Br, I) in lithium argyrodites (Li_6PS_5X). This modification preserves the overall crystal structure and lithium-ion diffusion pathways while enabling precise adjustments to the polarizability of the anion sublattice—essentially, how easily the charge distribution within the anions can be distorted. This strategy addresses both the static properties of the host lattice and its dynamic behaviour—how atoms move and interact over time. Studying these dynamics offers valuable insights into the complex interplay between structural characteristics, ionic hopping, and ionic conductivity [13,159–161]. To better understand the influence of the anion sublattice on the ionic performance of lithium argyrodites, Kraft *et al.* [145] synthesized Li_6PS_5X with different halogen compositions of (X = Cl, $Cl_{0.75}Br_{0.25}$, $Cl_{0.5}Br_{0.5}$, $Cl_{0.25}Br_{0.75}$, Br, $Br_{0.75}I_{0.25}$, $Br_{0.5}I_{0.5}$, $Br_{0.25}I_{0.75}$, and I). In the case of I^- containing samples, no site disorder between I^-/S^{2-} anions could be observed and I^- atoms (220 pm) exclusively occupied the Wyckoff *4a* position, as shown in Fig. 5a. However, in Cl^- and Br^- containing samples, significant anion disorder between X^-/S^{2-} is noted, primarily due to the similar ionic radii of Cl^- (181 pm), Br^- (196 pm), and S^{2-} (184 pm) [140,144,149,162,163]. Refinements of the NPD data reveals a linear increase in the lattice edge length as the substitution progressively favours iodine, consistent with Vegard's law, which states that the lattice parameter of an alloy is a linear function of the concentrations of its constituent elements. The increase in lattice length and unit cell volume also expands the distances for Li^+-Li^+ jumps within and between the cages. The Li(*24 g*)S_3 triangular bottleneck plane also enlarges due to increased Li-S bond lengths that further promotes excess Li^+ ions on the Wyckoff *24 g* site as shown in Fig. 5b. Correspondingly, the Li^+ concentration decreases on the Wyckoff *48 h* site. The anion polarizability is also affected with different sized halogen ions. Lower reported Debye frequencies as well as speed of sound values is an indication of the decrease in polarizability. Since completely dense samples reflect greater sound speeds, lower values here suggest that the lattice is softening with I^- substitution (Fig. 5c) [164]. Moreover, it has been demonstrated that softer lattices reduce the activation energy and increase ionic conductivity. However, the Arrhenius pre-factor (σ_0) is also directly responsible for the ionic conductivity calculation (Eqs. 1 and 2). An increase in the Arrhenius pre-factor and a decrease in activation energy are essential to achieving higher conductivity values. However, according to the Meyer-Neldel rule, a decrease in one quantity generally follows the other, which may indicate lattice softening or other structural factors [165–169]. In the case of Br- substitution, both the activation energy and the Arrhenius pre-factor decrease as expected, following the Meyer-Neldel rule, as shown in Fig. 5d. The $Li_6PS_5Cl_{0.5}Br_{0.5}$ composition still achieves the highest ionic conductivity because the drop in activation energy (due to optimal anion mixing) is much greater than the smaller reduction in the Arrhenius pre-factor (due to softer lattices), as seen in Fig. 5e. However, as I- substitution increases, the pre-factor continues to decrease due to further lattice softening, but the activation energy rises, likely because of minimal anion site disorder [149], defying the Meyer-Neldel rule. As a result, I^- doped samples show the lowest conductivities due to the higher activation barrier.

$$\sigma T = \sigma_0 \exp\left(\frac{-E_a}{k_B T}\right) \tag{1}$$

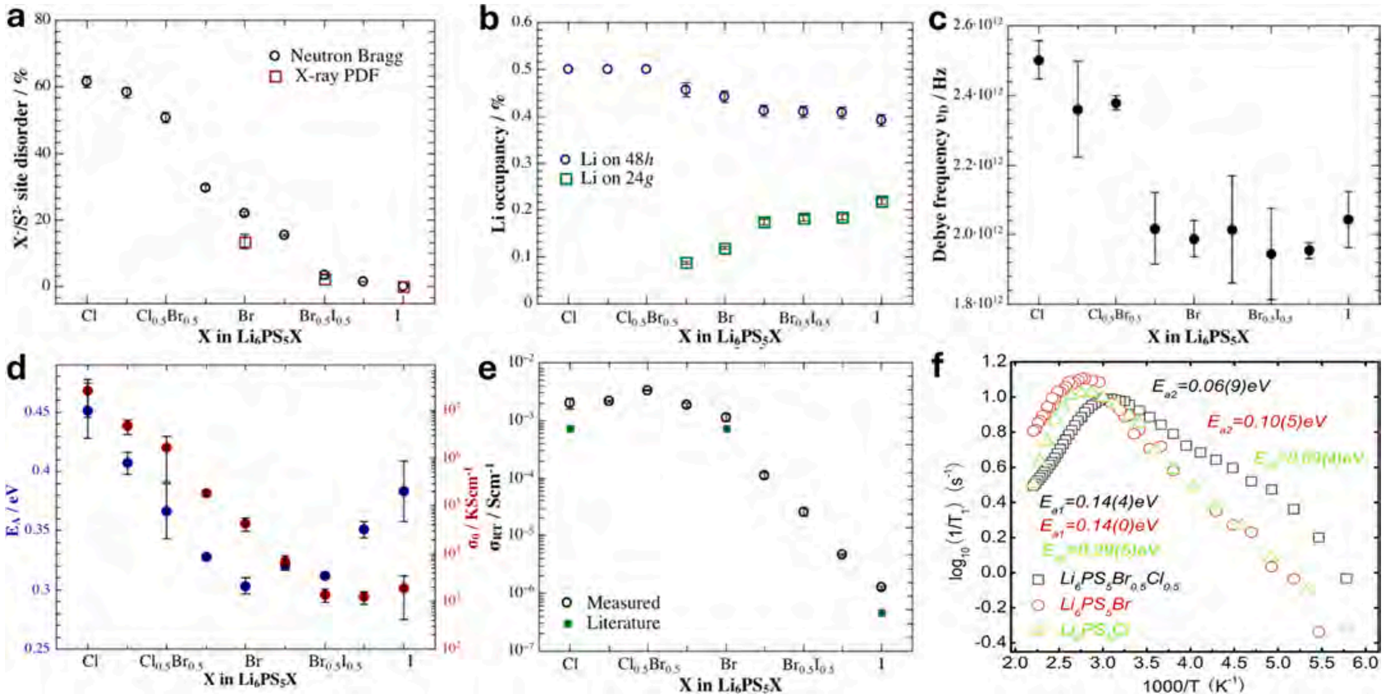

Fig. 5. (a) Impact of mixed halogens substitution on the X^-/S^{2-} disorder. (b) Changes in the lithium occupancy over Wyckoff *48 h* and *24 g* sites. (c) Variation in the Debye frequency for Li_6PS_5X (X=Cl, $Cl_{0.5}Br_{0.5}$, Br, $Br_{0.5}I_{0.5}$, I). (d) Changes in activation energy and Arrhenius pre-factor with mixed halogens doping. (e) Ionic conductivity for different halogen substituted samples. (f) ^{7}Li NMR SLR rates in rotating time frame for LPSCl, LPSBr, and $LPSCl_{0.5}Br_{0.5}$.
(a-e) Reproduced with permission from [145], copyright 2017, American Chemical Society. (f) Reproduced with permission from [170], copyright 2019, Elsevier.

$$\sigma_0 = \frac{zn(Ze)^2}{k_B} e^{\Delta s_m/k_B} a_0^2 \nu_0 \qquad (2)$$

Heng *et al.* [170] carried out a comparable study two years later, synthesizing $Li_6PS_5Cl_{0.5}Br_{0.5}$ using a ball-milling process and characterizing it using NMR and EIS. For $LPSCl_{0.5}Br_{0.5}$, the EIS observed ionic conductivities were 3.63 mS cm^{-1} at 32 °C that is higher than LPSCl (0.79 mS cm^{-1}) and LPSBr (0.36 mS cm^{-1}). The ^{7}Li NMR SLR rates in the rotating frames (R_{1p}) are depicted in Fig. 5 f for LPSCl, LPSBr, $LPSCl_{0.5}Br_{0.5}$. The SLR rate for $LPSCl_{0.5}Br_{0.5}$ reaches a maximum at 323 K, whereas it reaches the maximum at 348 K and 363 K for LPSCl and LPSBr, respectively. This suggests robust Li-ion diffusivity for optimally anion polarized $LPSCl_{0.5}Br_{0.5}$ composition. The activation energy calculated from Arrhenius law was 0.44, 0.39, and 0.31 eV for LPSCl, LPSBr, $LPSCl_{0.5}Br_{0.5}$. The mixed halogen doping provided anions exchange on the sulfur (Wyckoff *4d* sites) that caused optimal polarizability and improved conductivity. Better than single halogen LPSCl and LPSBr or even glass-ceramic Li_2S-P_2S_5 [171–175], enhanced cycling was reported using $LPSCl_{0.5}Br_{0.5}$ as SSE, Li_2S as cathode, and Li-In as anode.

3.3. Lithium site substitutions and vacancies

Achieving higher ionic conductivity and lower activation energy requires deliberate manipulation of anion polarizability in conjunction with increased disorder on the Wyckoff *4d* sites, as the previous work made clear. Interestingly, disorder on the S^{2-} site decreases with increasing halide ion size because it cannot hold bigger ions. Another important factor to consider is the lithium deficiency in the structure and composition. Inducing Li^+ vacancies have resulted in enhancement of the conductivity. The influence of Li^+ vacancies has been thoroughly examined by De Klerk *et al.* [149] by comparing the jump statistics plot from the MD simulations on artificial Li_6PS_6 (lithium deficient) and Li_7PS_5Cl (lithium rich) SSEs. There were differences seen in the doublet and intra-cage jumps but not in the inter-cage jumps. The lithium deficient version of Li_7PS_5Cl, namely Li_6PS_5Cl, showed higher conductivity, and to understand the rationale behind increased conductivity in Li^+ deficient samples, the radial distribution function at the atoms on the *4a* and *4d* sites was measured. It is found that the Li^+ ions surrounding the S site are higher (7 ions) than the Cl^- site (5 ions). As a result, an empty doublet always forms around Cl^-, facilitating multiple inter-cage hops for the Li^+ deficient composition, resulting in higher conductivity. Therefore, Li vacancies along with the replacement of the S atom with Cl atoms and its placement is necessary for improved conductivity. The recent study of Eva *et al.* [176] examined the consequences of over chlorinating $Li_{7-x}PS_{6-x}Cl_x$ (x = 1, 1.5, 2) and to also understand the impact of lithium vacancies on the performance. The activation energies of Li_6PS_5Cl, $Li_{5.5}PS_{4.5}Cl_{1.5}$, and $Li_5PS_4Cl_2$ were determined from the AIMD simulations to be 325.48 meV, 230.24 meV, and 292.62 meV, respectively. Ionic conductivity values were measured at 0.43, 14.55, and 1.69 mS cm^{-1}.

The lithium-ion probability density distribution in Fig. 6a shows that the increased quantity of Cl^- on the *4c* sites and abundant inter-cage jumps were the cause of a 100 meV reduced activation energy and a 30-fold increase in conductivity for $Li_{5.5}PS_{4.5}Cl_{1.5}$. Since the Li-Cl bonds are weaker than the Li-S bonds due to less negative charge, the electrostatic energy decreases as the Cl^- concentration increases, which is also a probable reason for decreased activation energy [179]. By the same logic, the $Li_5PS_4Cl_2$ stoichiometry should have an even greater ionic conductivity but the parent crystal structure shifts from F43m to C2mm for 1.5<x<2, as reported by [180]. The Ionic diffusion in C2mm

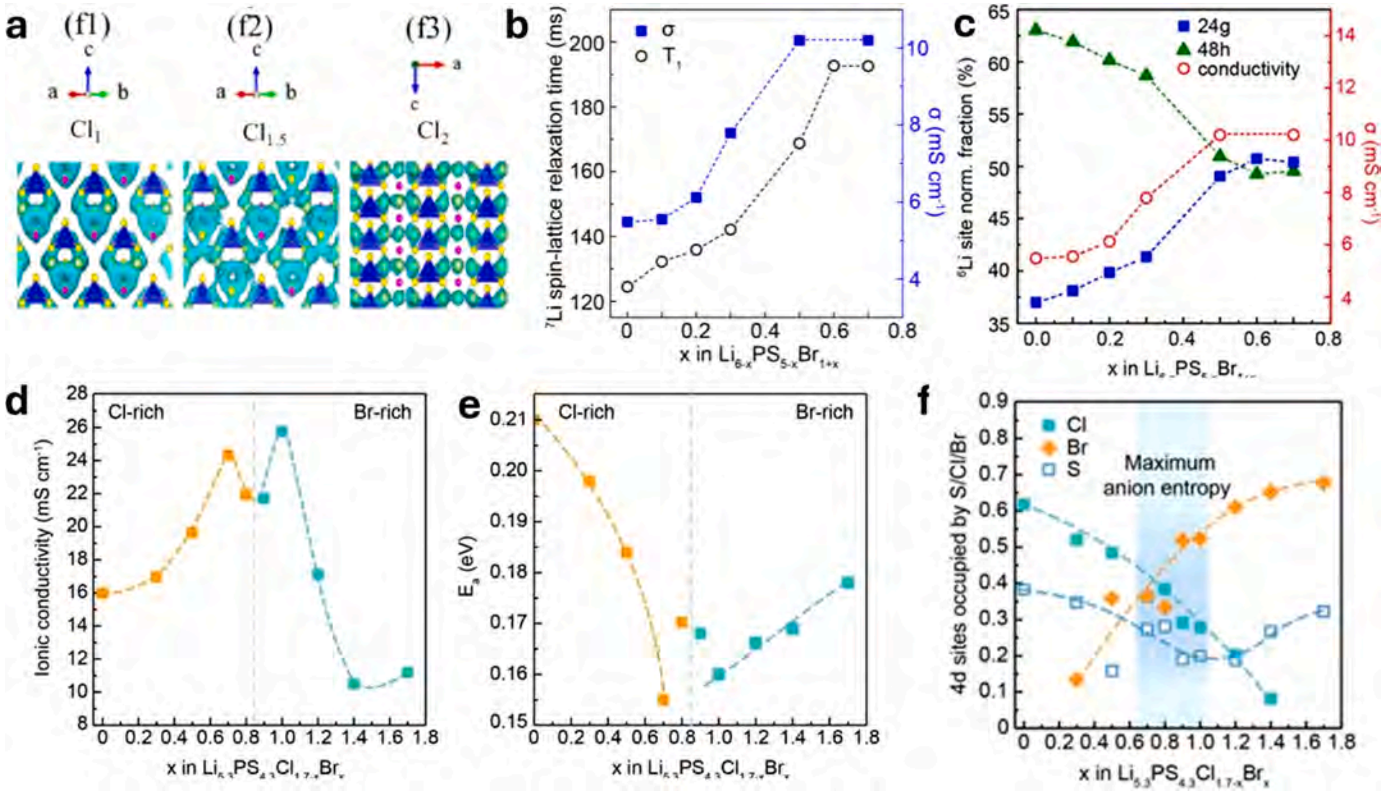

Fig. 6. (a) Li-ion probability density distribution from 900 K AIMD simulations. (b) Plot of ^{7}Li NMR SLR relaxation time (T_1) as a function of Br concentration to probe Li-ion dynamics. (c) Lithium site normalized occupancy at *24 g* and *48 h* site as obtained from ^{6}Li NMR and the corresponding ionic conductivity. (d-e) Variation in ionic conductivity and activation energy in the Cl-rich (x=0–0.8) and Br-rich (0.8–1.8) region. (f) Occupation of Cl (cyan), Br (orange), and S (blue) on the Wyckoff 4d sites as observed from ^{31}P NMR analysis.

(a) Reproduced with permission from [176], copyright 2022, Elsevier. (b-c) Reproduced with permission from [177], copyright 2020, American Chemical Society. (d-f) Reproduced with permission from [178], copyright 2023, Wiley.

is only strong in the c-direction with extremely low energy barrier, however in the a-b plane, it is exceedingly sluggish. Therefore, the diffusion is primarily 1-D diffusion. To still know the conductivity of $Li_5PS_4Cl_2$ for the probable F43m structure, the AIMD simulations calculate it to be 26.6 mS cm^{-1}. Lower conductivities for $Li_5PS_4Cl_2$ and $Li_5PS_4Br_2$ for C2mm structure from MD simulations were also observed by De Klerk *et al.* [149]. Analogous experimental study conducted by Adeli *et al.* [181] demonstrated validation between the MD simulations. For $Li_{5.5}PS_{4.5}Cl_{1.5}$, ultrafast Li^+ conductivity of 9.4 mS cm^{-1} with an activation energy of 0.29 eV was achieved. Higher NMR SLR rates at lower temperatures were also observed for $Li_{5.5}PS_{4.5}Cl_{1.5}$ compared to Li_6PS_5Cl. This implies that $Li_{5.5}PS_{4.5}Cl_{1.5}$ has faster Li-ion kinetics and jump frequency even at lower temperatures than the Li_6PS_5Cl SSE. To further investigate the impacts of inducing lithium vacancy by tailoring the halogen content, Feng *et al.* [182] synthesized a series of $Li_{6-x}PS_{5-x}Cl_{1+x}$ ($x = 0, 0.3, 0.5, 0.7, 0.8$) samples. Preservation of the parent crystal structure was observed even for $x>0.5$, unlike reported by Eva *et al.* [176]. A contraction in the lattice happens with an increase in lithium vacancy, observed from the XRD peak shift to higher angles with a maximum solubility limit of $x = 0.7$. A linear rise in conductivity is seen when Li^+ deficiency and Cl^- concentration increases [183,184]. For $x = 0.7$, the highest measured RT ionic conductivity of 17 mS cm^{-1} and the lowest energy barrier of 0.218 eV were found. As reported in [185], increased conductivity at $x=0.7$ is again linked to higher S^{2-}/Cl^- anions mixing at Wyckoff *4d* sites, further causing redistribution and an increase in the Li^+ ion occupancy from the *48 h* sites to the *24 g* transition sites. Excess concentration at the *24 g* transition site has shown to reduce the inter-cage jump distances and make the long-distance migration easier. Overchlorinated $Li_{5.5}PS_{4.5}Cl_{1.5}$ has also shown to display ineffective stripping plating with Li-metal anode. Wei *et al.* [186] stabilized the interface of $Li_{5.5}PS_{4.5}Cl_{1.5}$ by constructing a hybrid SEI interface consisting of LiCl/LiF/LiZn.

To further test with Br^-, Yu *et al.* [184] tuned the Br in $Li_{6-x}PS_{5-x}Br_{1+x}$ ($x = 0$–0.7). Annealing temperatures had a significant impact on the anions disorder that occurred in the case of Br. The maximum disorder was found to occur at 400 °C, which produced the greatest ionic conductivity of 4.17 mS cm^{-1} for $Li_{5.5}PS_{4.5}Br_{1.5}$ ($x = 0.5$), a value that was four times greater than for $x = 0$. In a follow-on study done by Pengbo *et al.* [177], they could synthesize $Li_{5.3}PS_{4.3}Br_{1.7}$ (higher solubility limit) without impurities, a composition similar to the one prepared by [182] in the same group by utilizing chlorine. Higher Br^- concentration and Li^+ deficiency leads to almost three-fold increase in conductivity (11 mS cm^{-1}) with a lower barrier of 0.18 eV. Ionic conductivity closely follows the trend of the amount of Li^+ residing on the *24 g* sites. A 35 % increase in lithium occupancy at transition *24 g* sites and 50 % higher ^7Li NMR SLR relaxation time for $x=0.7$ promotes the robust ionic conductivity in the sample as shown in Fig. 6b-c. Recently, Pengbo *et al.* [178] conducted another study that concentrated on changing the Cl^- and Br^- concentration while maintaining a stable Li^+ composition. In contrast to the mono-halide argyrodite study in the previous work, this study could dissociate the effects of different anions structural disorder and Li^+ deficiencies on the performance and offer insights into mixed and excess halogen doping. The group synthesized $Li_{5.3}PS_{4.3}Cl_{1.7-x}Br_x$ ($0 \leq x \leq 1.7$) in varying compositions while achieving the parent structure and obtained high phase purity (>96 %) for the middle region ($0.7<x<1.2$). Interestingly, dual-halide argyrodite phases yield higher conductivity than reported for the mono-halide argyrodite by the same group previously. Fig. 6d-e show the maximum conductivities as 24 and 26 mS cm^{-1}, reached with $x = 0.7$ ($Li_{5.3}PS_{4.3}Cl_{1.0}Br_{0.7}$) and $x = 1.0$ ($Li_{5.3}PS_{4.3}Cl_{0.7}Br_{1.0}$), respectively. In the region rich in chlorine, activation energy is likewise significantly decreased with bromination; the lowest value is 155 meV at $x = 0.7$. This is explained by a softer lattice that results from the substitution of the more polarizable element Br^- for the less polarizable element Cl^-. Since excessive bromination results in a softer but more organized lattice without significant disorder (unfavourable for activation energy) the activation energy in the bromine-rich area did not significantly change. This excessively high conductivity is attributed to the concerted migration by excess Li ions at the *24 g* site and maximum anions mixing or no-preference of site occupancy by S^{2-}, Cl^-, and Br^- at Wyckoff *4a* and *4d* site as obtained from the ^{31}P NMR and presented in Fig. 6 f. Wu *et al.* [187] synthesized a mixed anions SSE consisting of In, Cl, O, and S ($Li_{5.54}In_{0.02}PS_{4.47}O_{0.03}Cl_{1.5}$) that shows a high conductivity of 7.5 mS cm^{-1} with improved interfacial stability.

Zhang *et al.* [188] performed partial substitution of Li^+ ion by a trivalent Al^{3+} ion in $Li_{6-3x}Al_xPS_5Br$ ($x = 0.1, 0.15, 0.2, 0.25$, and 0.3). Al^{3+} could substitute Li^+ in the structure for up to $x = 0.2$, after which Al_2S_3 impurity phases starts to form. In addition to Al occupying the *24 g* site of Li, a decrease in the lattice size happens due to a smaller Al^{3+} ionic radius. As a result, coulombic repulsions in the doublet jump (*48h-24g-48h*) increases with increasing concentrations of mobile ions on the *24 g* locations. These repulsions increase the doublet jump distance as shown in Fig. 7a-b, but also cause a shrinking effect on the inter-cage and intra-cage jump distances. Ionic conductivity reported for $Li_{5.4}Al_{0.2}PS_5Br$ was 2.4 mS cm^{-1} compared to 1 mS cm^{-1} for Li_6PS_5Br, particularly due to shorter inter-cage jumping distance. In a similar strategy, Adeli *et al.* [189] explored the impact of substituting divalent Ca^{2+} for Li^+ in $Li_{6-2y}Ca_yPS_5Cl$. Unlike Al^{3+}, Ca^{2+} substitution alone didn’t affect the Cl^-/S^{2-} disorder or occupy Li^+ *24 g* sites. However excessive chlorination with Ca^{2+} doping in $Li_{6-x-2y}Ca_yPS_5Cl_{1+x}$ ($x = 0.25, y = 0.1$; $x = 0.25, y = 0.15$; $x = 0.375, y = 0.1$; and $x = 0.5, y = 0.1$) results in phase purity over 97 % with a constant Ca^{2+} concentration of $y = 0.1$. But beyond $y = 0.1$, impurities form, suggesting limitations at the Li^+ sites for substitution of divalent cations in Cl-rich argyrodites. The "super Cl-rich" variant ($x = 0.55$, $y = 0.1$) exhibits the highest ionic conductivity (10 mS cm^{-1}) with an energy barrier of 0.30 eV, mainly due to induced disorder in the SSE upon Cl-substitution and reduced electrostatic interactions as evident in Fig. 7c. Divalent Ca^{2+} doping on the Li^+ site also helps in shrinking the unit cell that reduces the rate-limiting inter-cage jumps and increases the diffusivity of the Li^+ ions, as shown in Fig. 7d. Dual modification strategy in Li_6PS_5Cl (x and y) provides promising structural features that gives: 3.3 times increase in conductivity for the “super-Cl rich” SSE over pure Li_6PS_5Cl, and 33 % higher than $x = 0.5$, $y = 0.1$.

3.4. *Chalcogenide site substitutions*

In Li_6PS_5X, chalcogenide ions occupy the free *4c/4d* sites, and *16e* positions in the PS_4^{3-} tetrahedra. As halogen concentration increases, disorder occurs at the *4a/4d* sites between chalcogenide and halogen ions, reducing energy barriers and enhancing conductivity, as previously noticed. In a theoretical study [120], it was concluded that the performance of lithium argyrodite could be improved by substituting the sulfur atom with a larger, more polarizable chalcogenide atom. The underlying concept is that ionic conductivity can be enhanced by introducing larger and less electronegative atoms. These larger, more polarizable anions reduce the interactions between Li^+ ions and the anion framework, thereby facilitating more efficient lithium diffusion pathways. Bonding in Li_6PA_5X (A = Chalcogen, X = Halogen) mainly arises due to electrostatic interactions between Li^+ ions and chalcogenide ions. The halogen ions interaction with Li^+ ions is weaker due to its location between the polyhedral units. While chalcogen anions with lower electronegativity prefer to coordinate with Li ions to produce octahedral configurations like Li_6A, phosphorus cations selectively connect with highly electronegative bivalent chalcogen anions (O > S > Se > Te > P) to generate tetrahedral units like PA_4^{3-}. Fig. 8a shows the structure of the Li_6PS_5I where Li^+ ions have halfway transitioned in the inter-octahedral migration (different Li_6S units) through the triangular bottleneck made of one I^- ion and two S^{2-} ions. Intra-octahedral migration (within Li_6S units) is represented by red arrows. From climbing image nudged elastic band (CI-NEB) simulation, energy barriers for intra-octahedral and inter-octahedral transport of Li^+ ions were influenced by partial iso-valent substitution at sulfur sites. For the

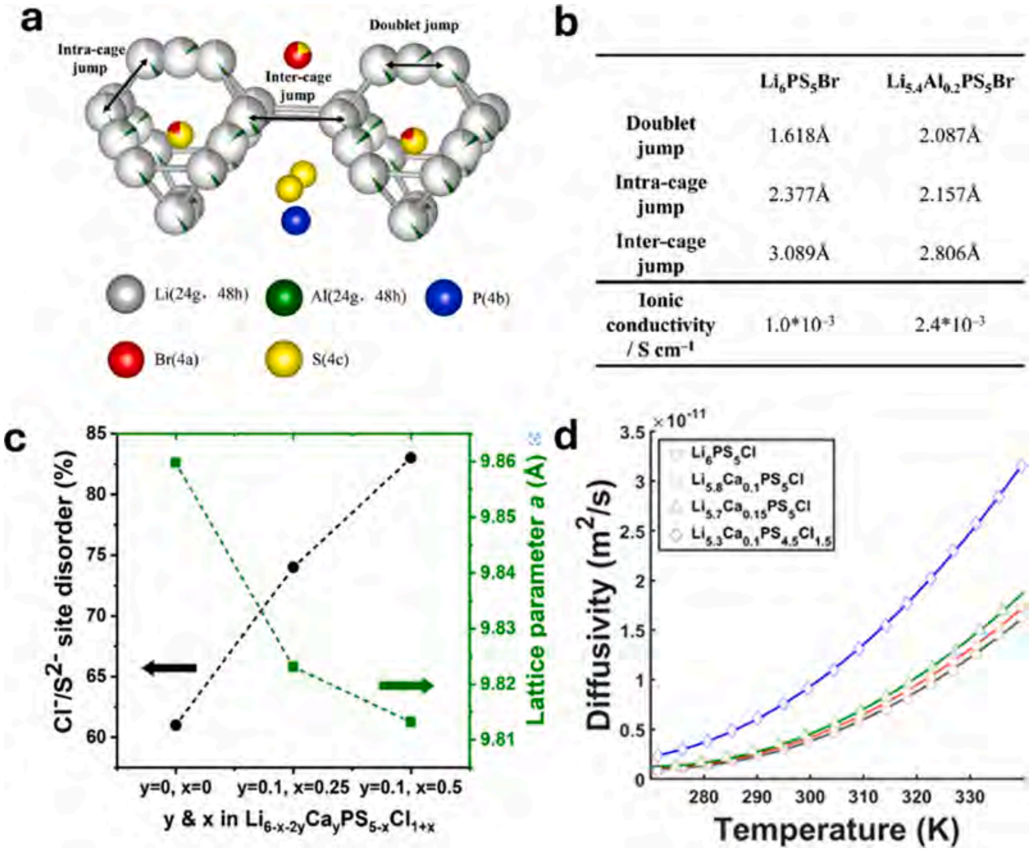

Fig. 7. Schematic representation of Li⁺ jumps (a) and corresponding data (b) in $Li_{6-3x}Al_xPS_5Br$, along with the jump distance values before and after Al^{3+} substitution. (c) Cl^-/S^{2-} site disorder as a function of x and y in $Li_{6-x-2y}Ca_yPS_{5-x}Cl_{1+x}$. (d) Diffusivity of Li-ions obtained from PFG NMR for cation and cation-anion modified stoichiometry in $Li_{6-x-2y}Ca_yPS_{5-x}Cl_{1+x}$.
(a-b) Reproduced with permission from [188], copyright 2020, Elsevier. (c-d) Reproduced with permission from [189], copyright 2021, American Chemical Society.

intra-octahedral migration (Fig. 8b) Li_6PSeS_4I shows the lowest energy barrier in contrast to Li_6PSO_4I. Thus, migration of Li^+ ions are inversely related to the electronegativity of the chalcogen ion in the Li_6A octahedra or PA_4 tetrahedra (A = O, S, Se, Te, P). Similar results are true for the inter-octahedral migration as shown in Fig. 8c with Li_6PTeS_4I having the lowest energy barrier due to least electronegativity of Te.

To experimentally test this hypothesis, Bernges *et al.* [190] substituted Se^{2-} ions for S^{2-} ions in Li_6PS_5Br. The increase in lattice parameter of the unit cell was attributed to the larger ionic radius of Se^{2-} (198 pm) compared to S^{2-} (184 pm). The expansion of the PS_4^{3-} tetrahedra due to the occupation of *16e* sulfur sites by selenium ions aligned with theoretical predictions. Contrary to previous research that showed that a greater anion size mismatch between two anions (sulfur and iodine) caused the site disorder to lessen, in this case, selenium doping also reduced anion disorder while not creating a larger anion size mismatch than sulfur ion. As higher anions disorder decreases the Li^+ site occupancy at *48 h* site, lower disorder with Se^{2-} doping increases the Li⁺ occupancy at the Wyckoff *48 h* site and leads to greater Coulombic repulsions during doublet jumps that consequently reduces inter-cage distances. The diffusion pathways, indicated by LiA_3Br (A = chalcogenide) polyhedral units and LiS_3 triangular planar regions shows an increase in volume, suggesting a broadening of the diffusion bottleneck channels. However, despite the sharp reduction in anion site disorder, there is no significant increase in ionic conductivity or a decrease in activation energy. A higher ionic conductivity was still measured for Li_6PS_4SeBr as 3.9 mS cm^{-1}. Se substitution was also examined in $Li_6PS_{5-x}Se_xI$ (x = 0–5) system [191]. Interestingly, the disorder between S^{2-}/I^- could be induced up to 7 % with the addition of Se^{2-} ion along with similar broadening of the diffusion pathways in the previous work ($Li-(S/Se)_3$ triangular transition region and $Li-(S/Se)_3I$ tetrahedra), illustrating wider pathways of the doublet and intra-cage jump (Fig. 8d). Moreover, lattice polarizability is induced with a bigger chalcogen ion as reflected by the measurement of lower speed of sound and Debye frequencies, which decreases the activation barrier from 0.38 eV (x = 0) to 0.28 eV (x = 5). Ionic conductivity of 0.28 mS cm^{-1} can be achieved for fully Se-substituted Li_6PSe_5I compared to 0.0025 mS cm^{-1} for Li_6PS_5I. Overall, $Li_6PS_{5-x}Se_xI$ exemplifies how broadening of diffusion channels, coupled with lattice softening, impacts ionic transport.

Xuan *et al.* [192] further explored the impact of Te doping on S sites in the off-stoichiometric $Li_{6.25}PS_{5.25-x}Te_xCl_{0.75}$ (x=0.125). Off-stoichiometric composition allows for higher Li^+ content in the structure and facilitates Li^+ transport [193]. Similar observations in increasing bond-lengths and diffusion channels were made. Total resistance from EIS for the three compounds was: Li_6PS_5Cl (266.2 Ω), $Li_{6.25}PS_{5.25}Cl_{0.75}$ (72.5 Ω), and $Li_{6.25}PTe_{0.125}S_{5.125}Cl_{0.75}$ (16.56 Ω). Conductivity of Li_6PS_5Cl was 0.28 mS cm^{-1}, $Li_{6.25}PS_{5.25}Cl_{0.75}$ was 1.03 mS cm^{-1}, and $Li_{6.25}PTe_{0.125}S_{5.125}Cl_{0.75}$ was 4.5 mS cm^{-1}, all at RT. Additionally, this electrolyte demonstrated electrochemical compatibility over a wide potential window, up to 7 V, with a Li anode. These findings underscore the potential of the broadened diffusion pathways, loosened cation-anion bonds, and polarizability of the structure on the ionic conductivity and activation energy of the lithium argyrodites.

3.5. Phosphorus site substitutions

The introduction of vacancies on the Li⁺ site, along with multi-halogen and chalcogenide substitutions on the S^{2-} site has significantly enhanced the performance of lithium argyrodites. Similarly, the

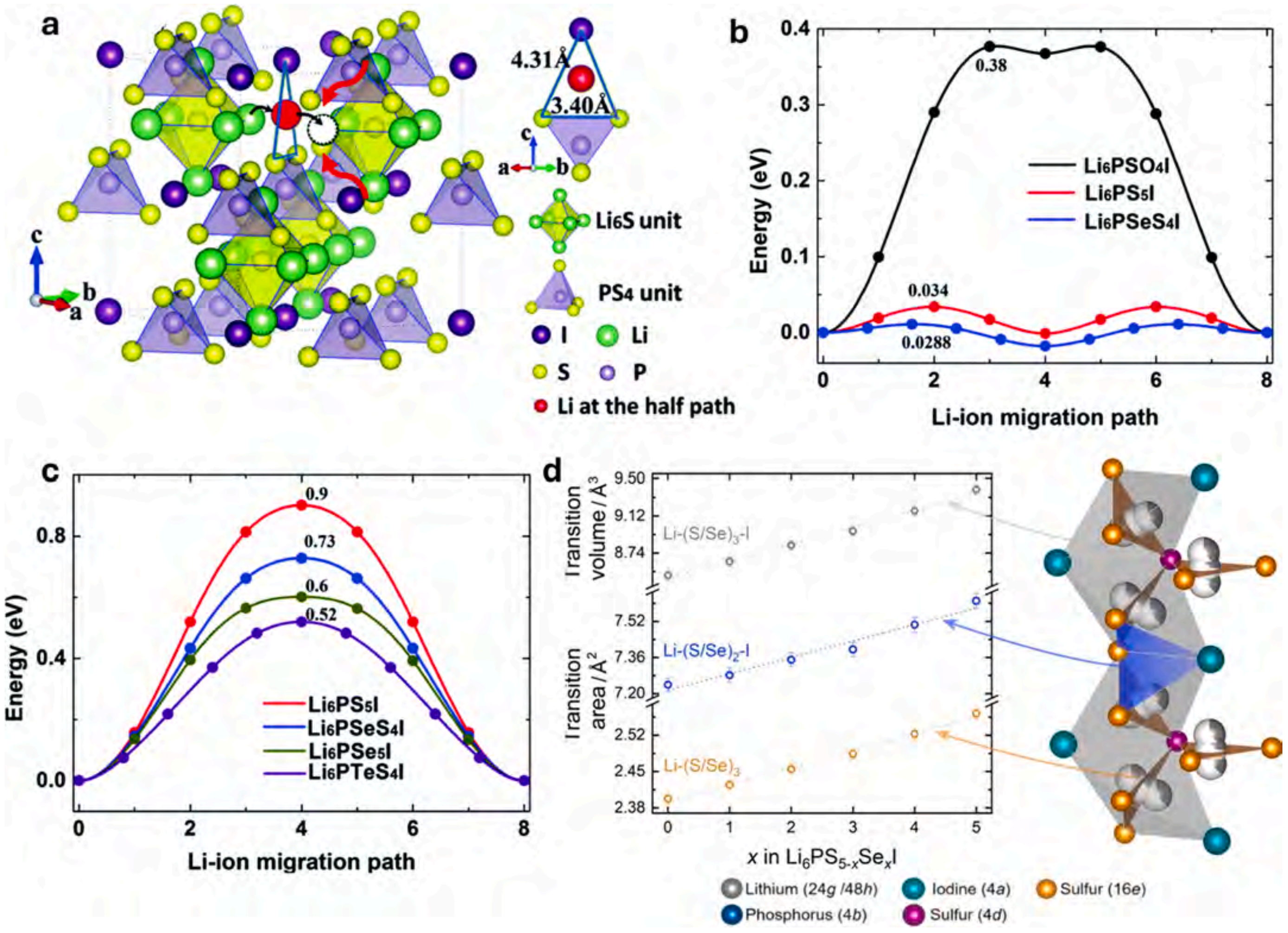

Fig. 8. (a) Li_6PS_5I structure depicting partial Li-ion inter-octahedral migration through a triangular $Li(S/I)_3$ plane. Red arrows indicate the pathway of intra-octahedral migration. (b-c) Energy barriers of Li^+ intra-octahedral and inter-octahedral migrations, respectively. (d) Variation in the diffusion channels area and volume as a function of Se-doping in Li_6PS_5I.

(a-c) Reproduced with permission from [120], copyright 2017, Royal Society of Chemistry. (d) Reproduced with permission from [191], copyright 2020, American Chemical Society.

impact of Li^+ stuffing in the crystal structure has also proved to be a significant improvement. One additional potential site for crystal structure modification *via* substitution remains to be the P^{5+} site. Specifically, aliovalent substitution on the P^{5+} site has caused great improvements in the performance as it also includes the introduction of extra Li^+ in the structure to maintain charge neutrality. Aliovalent substitution of Si^{4+} was performed on the P^{5+} site in the $Li_{6+x}P_{1-x}Si_xS_5Br$ crystal structure [194]. Due to the larger ionic radius of Si^{4+} than P^{5+} (260 pm vs 170 pm) [195], an 0.7 % increase in the lattice size and 8 % increase in the volume of the $P_{1-x}Si_xS_4^{3-}$ tetrahedra was noticed at the maximum solubility of Si^{4+} substitution at $x = 0.3$ mol. Additionally, there exists a disorder already between the S^{2-}/Br^- anions in Li_6PS_5Br, so the Si^{4+} substitution does not induce any extra disorder and the Li^+ jump distances remain unimpacted. Si^{4+} substitution results in a four-fold increase in the ionic conductivity at $x = 0.3$ (2.4 mS cm^{-1} vs 0.7 mS cm^{-1}), which is mainly a result of induced correlated motion of Li^+ ions by their increased density on the *24 g* transition site [118]. In the similar approach, promising characteristics are known by substituting Si^{4+} ions on the P^{5+} site in $Li_{6+x}P_{1-x}Si_xS_5I$ ($x = 0$–0.6) [196]. The fully ordered structure and negligible anions disorder in Li_6PS_5I can be altered to display some S^{2-}/I^- anions disorder with Si doping. A larger Li_6PS_5I lattice also incorporates higher concentration of Si ($x = 0.6$) compared to Li_6PS_5Br compound ($x = 0.3$), primarily because of a bigger sized crystal. An increase in the P/Si-S bond length happens in the $(P_{1-x}Si)S_4^{3-}$ polyhedra due to repulsions faced between the P and Si atoms because of lower relative electronegativity of the Si compared to P atom. A report of 1.1 mS cm^{-1} for the highest RT ionic conductivity is observed for $x = 0.3$, which is four orders of magnitude greater than the undoped counterpart with a completely ordered structure. In a follow on study to provide further evidence, Ohno *et al.* [197] again synthesized $Li_{6+x}P_{1-x}Si_xS_5I$ and recorded a 12 % site disorder between S^{2-}/I^- and 8.5 % increase in the P^{5+} polyhedral volume from NPD. The bottlenecks for the long-range diffusion are the Li(*48 h*)S_3I polyhedra and the area of the Li(*24 g*)S_3 triangular plane. This study records a 38 % increase and 8 % decrease in the Li^+ occupancy on the *24 g* and *48 h* sites, which altogether increases the conductivity to 2 mS cm^{-1} and validates the previous research. It could be concluded from these studies that a local ordering of I^- and S^{2-} is disadvantageous to the long-range jumps. However, if the disorder is induced due to substitution, then it is thought that it will creates paths for low-energy inter-cage jumps, which can be attributed to the expansion of the diffusion pathways, bottleneck regions, and excess lithiation on *24 g* sites

Kraft *et al.* [146] performed the aliovalent substitution of a slightly bigger element, germanium, from the carbon family, in $Li_{6+x}P_{1-x}Ge_xS_5I$ ($x = 0$–0.8). The bigger Ge^{4+} could be successfully substituted up to $x = 0.7$, which is higher than smaller Si^{4+} as seen in previous reports. Ge substitution also resulted in 7 % site disorder at x = 0.7. Induced disorder is lower compared to higher solubility of Ge^{4+} when compared to higher disorder through Si^{4+} and its lower solubility. The on-set of disorder directly correlates with the reduction in the activation energy and increase in ionic conductivity (Fig. 9a-b). Highest conductivity of 5.4 mS cm^{-1} and an activation energy of 0.24 eV is measured for $Li_{6.6}P_{0.4}Ge_{0.6}S_5I$, which is 2.8 times higher than $Li_{6.46}P_{0.54}Si_{0.46}S_5I$. Sintering at 823 K for 10 mins results in a slightly more than tripled ionic conductivity of 18.4 ± 2.7 mS cm^{-1}. In addition, authors attempted the doping of bigger sized Sn ion, however its limited solubility in the structure did not provide any considerable results as reported by [197]. These tests show that the varying ionic radii elements in aliovalent doping do not significantly alter the structure; rather, the main factor affecting performance is the Li^+ concentration and its long-range diffusion producing substructure.

Recently, [198] performed the synthesis of a multi-element and equimolar substitution on the P^{5+} site in Li_6PS_5I. Multi-element substituted materials are also referred to as the high-entropy materials (HEM's) if more than 5 elements share a single crystallographic site. ΔS_{config} (configurational entropy) is used to determine the high-entropy materials when ΔS_{config} is greater than or equal to 1.5 R [200]. Cationic substitution of Si, Ge, Sb atoms on the P^{5+} site to form $Li_{6.5}[P_{0.25}Si_{0.25}Ge_{0.25}Sb_{0.25}]S_5I$, calculates the $\Delta S_{config} = 2.77$ R, which renders it as a high entropy material. Structurally, the electrolyte preserves the *F43m* phase as shown in Fig. 9c. The energy dispersive X-ray spectroscopy (EDS) mapping from the scanning electron microscopy (SEM) image shows the uniform distribution of all elements in the SSE. A polyanionic tetrahedra is formed with S^{2-}, P^{5+}, and the aliovalent substitued multi-elemets. From the crystal structure in the Fig. 9c, the S^{2-} and I^- anions form a FCC sublattice with S^{2-} ions residing in partial tetrahedral voids at *16e* positions. S^{2-} ions further forms a $[P_{0.25}Si_{0.25}Ge_{0.25}Sb_{0.25}S_4]^{3.5-}$, $[PS_4]^{3-}$, $[SiS_4]^{4-}$,$[GeS_4]^{4-}$, and $[SbS_4]^{3-}$ anion groups. NPD estimates the S^{2-}/I^- anions diorder to be 11 %. Further, decreased inter-cage distance increases the diffusion to $7.09*10^{-12}$ m^2 s^{-1} and the reported ionic conductivity at RT is 13.2 mS cm^{-1} with an enegry barrier of 0.2 eV. Measured electronic conductivity was 2–3 orders of magnitude higher than other conductors [201,202]. From Fig. 9d, the SSE displays stable cycling at C/2 rate for upto 200 cycles.

Significant enhancements in the ionic conductivity can be very well observed from the long list of experiments done in the previous half-decade. Typical ionic conductivities of 2–3 mS cm^{-1} for Li_6PS_5Cl have been increased and approaching to 10 mS cm^{-1}, even for the Li_6PS_5I variant which exhibits ~10^{-7} S cm^{-1} in the pristine form. However, the conductivity in the cold pressed state is still lower. Sintered electrolytes show higher conductivity but that often comes with increased side

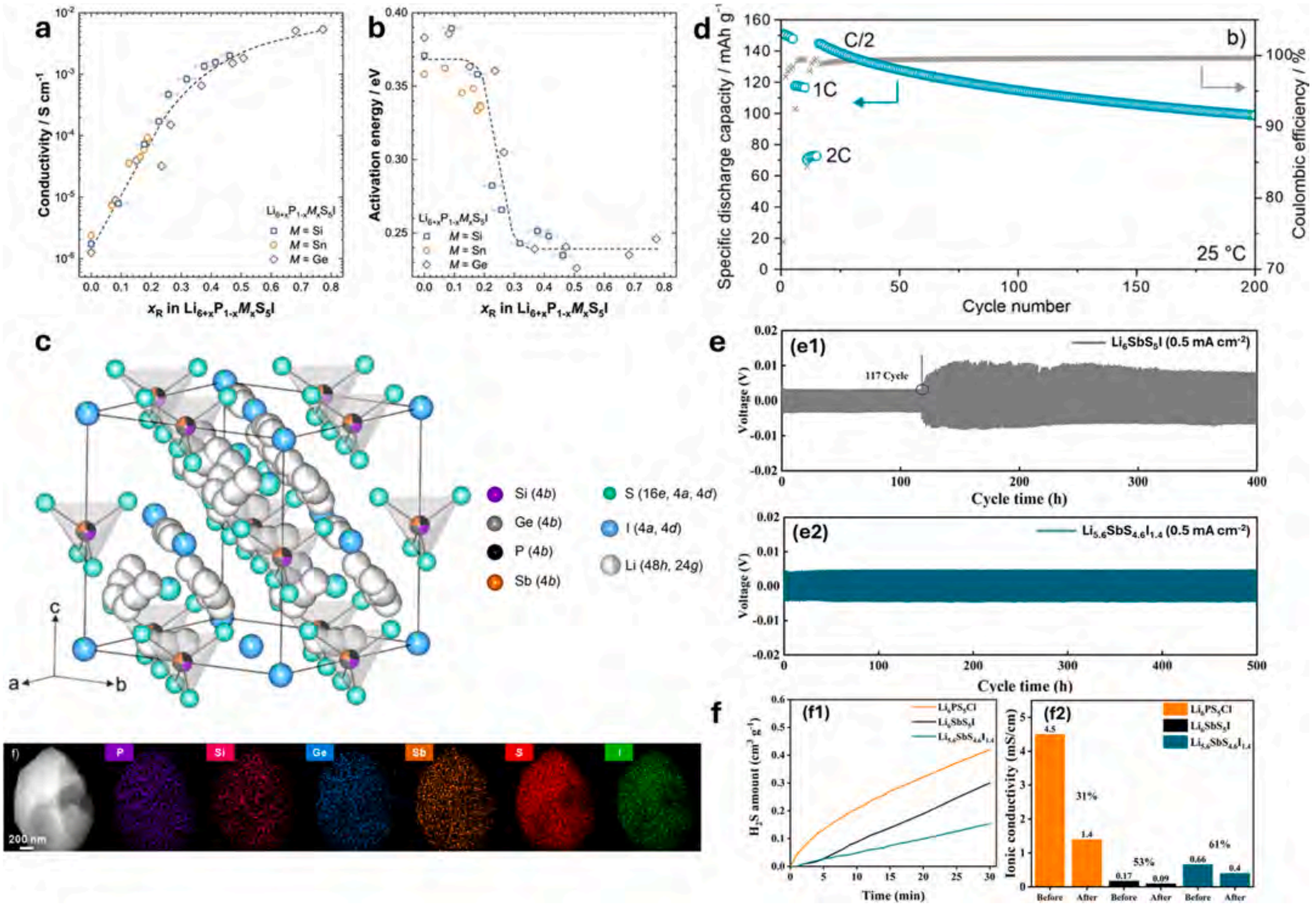

Fig. 9. Ionic conductivity (a) and activation energy (b) as a function of mol% substitution of M in $Li_{6+x}P_{1-x}M_xS_5I$ (M = Si, Ge, Sn). (c) Crystal structure of $Li_{6.5}[P_{0.25}Si_{0.25}Ge_{0.25}Sb_{0.25}]S_5I$ with Wyckoff positions of different elements and the SEM-EDS mapping of each element of the multi-element equimolar SSE. (d) Cycling stability and coulombic efficiency of ASSB cell containing $LiNbO_3$-NMC(85 %Ni)/$Li_{6.5}[P_{0.25}Si_{0.25}Ge_{0.25}Sb_{0.25}]S_5I/Li_4Ti_5O_{12}$ at C/2 rate for 200 cycles. (e) Li^+ stripping and plating of (e1) Li_6SbS_5I and (e2) I-rich glass ceramic $Li_{5.6}SbS_{4.6}I_{1.4}$ SSE. (f) H_2S evolution results (f1) for Li_6PS_5Cl, Li_6SbS_5I, and $Li_{5.6}SbS_{4.6}I_{1.4}$ at 25 °C and 10 % humidity and (f2) ionic conductivity retention (%) after 30 minutes air exposure.

(a-b) Reproduced with permission from [197], copyright 2019, American Chemical Society. (c-d) Reproduced with permission from [198], copyright 2022, American Chemical Society. (e-f) Reproduced with permission from [199], copyright 2023, American Chemical Society.

reactions at the electrode/electrolyte interface, which is not desirable for the commercial solid-state batteries. To broaden the horizon of the lithium argyrodites, a new class of thio-antimonate argyrodites have been developed recently by several different groups in the quest of beating the saturation observed in the typical lithium argyrodites. Interestingly, this new variety of lithium argyrodites possess improved air stability with the replacement of phosphorus (a hard acid) with antimony (a soft acid) element. Based on the hard-soft acid-base theory (HSAB), the Sb-S bonds have proven to have higher resistance with the water molecules than the P-S bonds, as also reported in [203–205], which makes them better stability wise. Kimura et al. [206] synthesized Li_6SbS_5X (X = Cl, Br, I). However, the synthesis of only Li_6SbS_5I (X = I) could be achieved whereas for (X = Cl, Br), solid solutions of Li_3SbS_4 and Li_2S were crystallized potentially due to significant size mismatch between Cl and Br halogens and the SbS_4 tetrahedra. Ionic conductivities of the Li_6SbS_5I and Li_6PS_5I did not seem to differ much (~10^{-6} mS cm^{-1}).

Kim *et al.* [199] synthesized I-rich glass-ceramic argyrodite $Li_{6\text{-}x}SbS_{5\text{-}x}I_{1+x}$ (x = 0, 0.2, 0.4, 0.6) using Sb atom based on the recent findings showing the possibility of I^- substituting on the S^{2-} site of Wyckoff *4d* in the Li_6PS_5I system. Liu *et al.* [207] achieved I^- incorporation up to x = 0.4 in the stoichiometric $Li_{5.6}PS_{4.6}I_{1.4}$. They used glass-ceramic synthesis approach that involved using ultimate high-energy mechanical milling method (UHEMM) at 1500 rpm for 1 h. This process does not include crystallizing the electrolyte by sintering methods at high temperatures and also reduces the synthesis time against traditional mechanical milling and annealing for *ca.* 20 hours [207,208]. They reported a high conductivity of 2 mS cm^{-1} for $Li_{5.6}PS_{4.6}I_{1.4}$ as opposed to 0.5 mS cm^{-1} for Li_6PS_5I using UHEMM process. Synthesis of the thio-antimonate version using this UHEMM method reveals a conductivity of 0.66 mS cm^{-1} for same mol% of I substitution in $Li_{5.6}SbS_{4.6}I_{1.4}$ versus 0.17 mS cm^{-1} for Li_6SbS_5I, which is

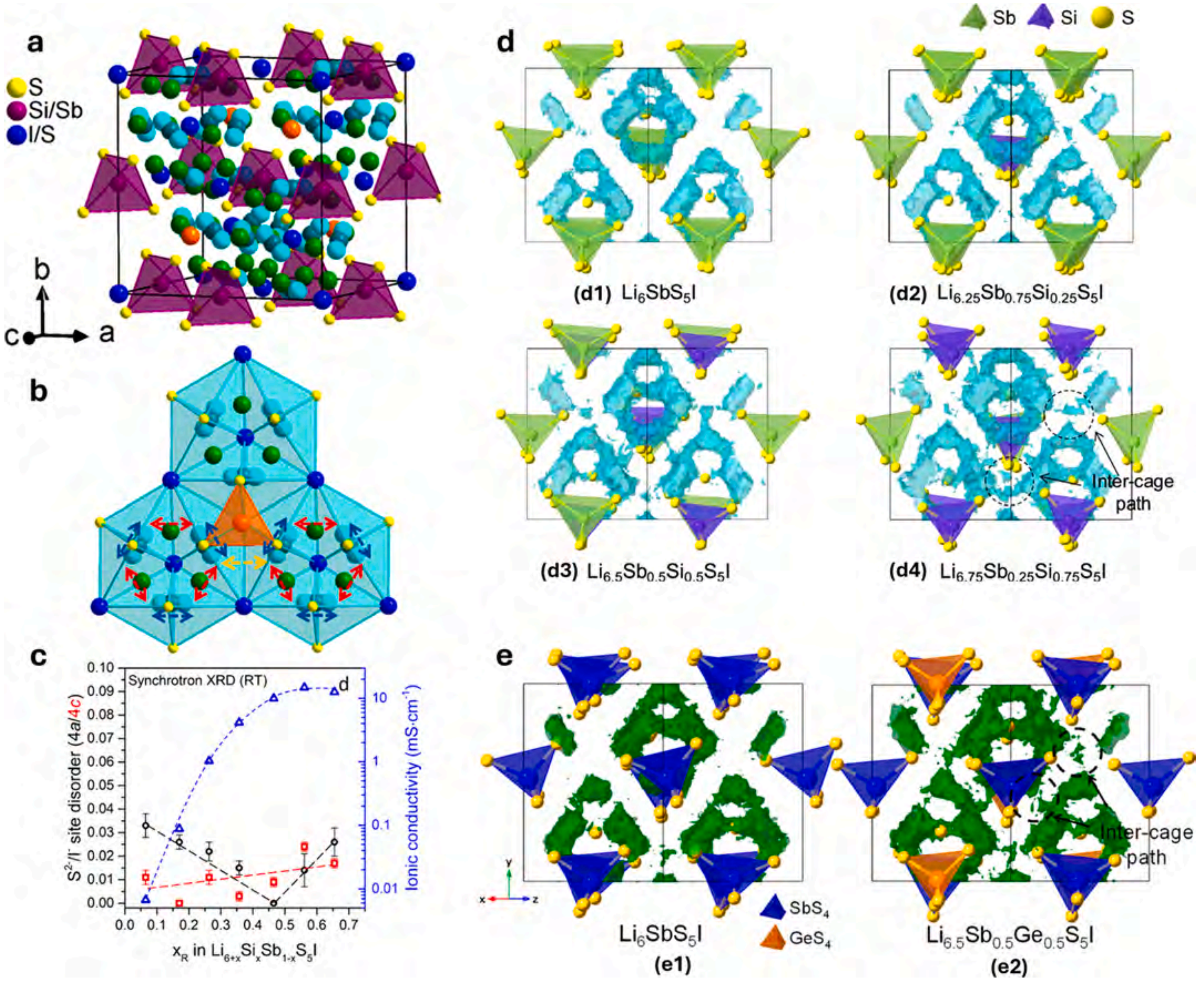

Fig. 10. (a) Crystal structure of the new thio-antimonate $Li_{6.7}Si_{0.7}Sb_{0.3}S_5I$ SSE at 300 K from NPD. (b) Schematic of the Li^+ ion sites: Li1(*48 h*) - turquoise, Li2(*24 g*) – teal, newly found Li3(*48 h*) - green, Li4(*4 d*) – orange. Jump pathways: the doublet jump (Li1(*48 h*)–Li1(*48 h*) within bipyramids passing through Li2(*24 g*), blue arrow), the intra-cage jump (Li1(*48 h*)–Li1(*48 h*) within the cage passing through the newly found Li3(*48 h*) site, red arrow) and inter-cage jumps (Li1(*48 h*)–Li1 (*48 h*), Li3(*48 h*)-Li3(*48 h*) between cages, orange arrow). (c) Ionic conductivity and S^{2-}/I^- disorder on the *4a* and *4c* sites with Si doping. (d) Iso-surfaces of Li+ ion probability densities at 1000 K for Si doping of x = 0, 0.25, 0.5, and 0.75 in $Li_{6+x}Sb_{1\text{-}x}Si_xS_5I$. (e) Iso-surfaces of Li^+ ion probability densities of Li_6SbS_5I and $Li_{6.5}Sb_{0.5}Ge_{0.5}S_5I$.

(a-c) Reproduced with permission from [204], copyright 2019, American Chemical Society. (d) Reproduced with permission from [203], copyright (2021), American Chemical Society. (e) Reproduced with permission from [205], copyright 2022, American Chemical Society.

lower than the P^{5+} based lithium argyrodites prepared using UHEMM process. Liu *et al.* also estimated the anions mixing of about 44 % in the glass-ceramic electrolyte. A similar trend in anions mixing could be accepted for Sb-based lithium argyrodites containing I due to better conductivity observation. Both the $Li_{5.6}PS_{4.6}I_{1.4}$ and $Li_{5.6}SbS_{4.6}I_{1.4}$ displayed significantly improved Li stripping and plating. The stripping/-plating plot of Li_6SbS_5I and $Li_{5.6}SbS_{4.6}I_{1.4}$ are shown in Fig. 9e(e1,e2). In addition, better H_2S stability after exposure to air for 30 mins at RT, and better ionic conductivity retention after air exposure was shown by Kim *et al.* [199] for $Li_{5.6}SbS_{4.6}I_{1.4}$, indicating the working impact of HSAB theory (Fig. 9 f(f1,f2).

Replacement of P^{5+} with Sb^{5+} has shown considerable improvements in the stability and hydrolysis areas however their ionic conductivity is still not up to the expectations already met by the aliovalent doped P^{5+} type argyrodites. Using the similar strategy, Nazar group [204] has synthesized thio-antimonate argyrodites along with aliovalent doping of carbon-family elements with the general formula of $Li_{6+x}M_xSb_{1-x}S_5I$ (M = Si, Ge, Sn). The solubility limit observed for Si, Ge and Sn was 0.7, 0.4, and 0.2 mol%, respectively. The crystal structure with aliovalent doping successfully maintained the same cubic space *F43m* group even after sintering (Fig. 10a). Shrinking of the lattice happens as Si^{4+} has lower ionic radius than Sb^{5+}. Like the P^{5+} structure, anions disorder is also increased to *ca.* 3 % with Si and Ge substitution. A tremendous improvement in conductivity is seen for $Li_{6.7}Si_{0.7}Sb_{0.3}S_5I$, which records to 11.2 mS cm^{-1} at RT with an energy barrier of 0.25 eV as shown in Fig. 10c. Further annealing and sintering can induce conductivities up to 14.8 mS cm^{-1} and 24 mS cm^{-1}, respectively, owing to the enhanced grain boundary contact [209–212]. A three-order increase in conductivity from 0.01 mS cm^{-1} for x = 0 (Li_6SbS_5I) has been intricately linked to the increased Li^+ concentration, altered distribution of anions – increasing disorder on *4c/4d* sites, and the discovery of a new Li (*48 h*) site as explained by Nazar's group from the NPD data. As shown in Fig. 10b, the crystal structure has 4 distinct Li^+ sites: Li1(*48 h*) - turquoise, Li2(*24 g*) – teal, newly found Li3(*48 h*) – green, Li4(*4d*) – orange. The distinct jumps involved in Li⁺ diffusion are: the doublet jump (Li1(*48 h*)–Li1(*48 h*) within bipyramids, passing through the Li2 (*24 g*) site, indicated by the blue arrow), the intra-cage jump (Li1(*48 h*)–Li1(*48 h*) within the cage, passing through the newly identified Li3 (*48 h*) site, shown by the red arrow), and the inter-cage jump (Li1 (*48 h*)–Li1(*48 h*) between cages, marked by the orange arrow). The newly found Li3(*48 h*) site also facilitates the inter-cage jump from Li3 (*48 h*)-Li3(*48 h*), as shown by the orange arrow. To maintain charge neutrality, the concentration of Li^+ increases with Si^{4+} substitution, and this forces more Li^+ ions onto the newly found high energy interstitial Li3(*48 h*) sites while creating vacancies on the Li1(*48 h*)–Li2(*24 g*)–Li1 (*48 h*) doublet jump sites. These high energy interstitial positions (Li3) act like the low energy positions (Li1). The induced coulombic repulsions on the doublet site leads to the long-range concerted migration through the low energy (Li3) site with low barrier. In a follow-on work next year by the Yu group, Lee *et al.* [203] showed a higher solubility limit of Si^{4+} to x = 0.75 using high-energy ball milling, thereby forming a $Li_{6.75}Si_{0.75}Sb_{0.25}S_5I$. Higher solubility of Si^{4+} recorded an even higher conductivity of 13.1 mS cm^{-1} with a barrier of 0.17 eV. Lee *et al.* also demonstrated a conductivity of 1.4 mS cm^{-1} at a low temperature of −20 °C. This reasoning was understood from the Li-ion probability density iso-surfaces obtained from the AIMD simulation that showed very well connected iso-surfaces between the cages for x = 0.75, which did not exist for x = 0, 0.25, 0.5 (Fig. 10d(d1-d4)). These interconnections are vital for long-range inter-cage jumps. For the Ge substitution, Nazar group [204] showed the solubility up to x = 0.4, which yielded a conductivity of 6.3 mS cm^{-1}. Lee *et al.* [205] demonstrated a higher solubility limit up to x = 0.5, with the formula $Li_{6.5}Sb_{0.5}Ge_{0.5}S_5I$, which also preserved highly symmetric argyrodite phase. They obtained the highest reported ionic conductivity so far of 16.1 mS cm^{-1} in the cold-pressed state for the thio-antimonate argyrodites. The synthesis procedure used here was a high-energy ball milling and further annealing to 450 °C, as also used in Si^{4+} substitution. Similar well-connected iso-surfaces from the AIMD simulations for high percentage of Ge^{4+} doping, and concerted ion-migration were ascribed as the main reason for highest ionic conductivity (Fig. 10e(e1-e2)).

As argyrodite materials evolve to meet ever-increasing conductivity demands, there's a growing concern regarding the mechanical properties that are essential for practical application, especially in advanced SSBs [213,214]. While the pursuit of higher ionic conductivity remains a primary objective in SSEs development, the preservation of intrinsic mechanical properties, such as flexibility and low modulus in sulfide argyrodites becomes increasingly crucial. These properties are vital for ensuring the SSE can effectively accommodate the dynamic structural changes occurring during battery operation. However, the conventional method of annealing sulfide SSEs at elevated temperatures to promote crystallinity inadvertently alters their mechanical characteristics [86, 182,204,215–217]. Specifically, this annealing process induces grain growth and promotes long-range ordering within the SSE structure, leading to an increase in elastic modulus. This rise in elastic modulus poses significant challenges, particularly in the context of accommodating the volumetric changes inherent in the cycling of high-energy-density batteries [218]. Therefore, the delicate balance between optimizing ionic conductivity and preserving mechanical resilience necessitates innovative approaches that mitigate the detrimental effects of crystallinity enhancement on the mechanical properties of sulfide argyrodites. These advancements are critical for ensuring the long-term performance and reliability of advanced SSBs in demanding applications.

In the pursuit of enhancing SSEs, partial halogen substitution in Li-argyrodite sulfides has shown promise, yielding high room temperature ionic conductivity. However, challenges arise with increased substitution, leading to decreased conductivity. Computational studies suggest fully halogenated argyrodites (FHAs) as ideal lithium-ion solid conductors (LISCs) [149,180,182,217,219], and very recently, Jung *et al.* [220] achieved a breakthrough by synthesizing a thio-antimonate argyrodite SSE with high conductivity and deformability, and low elastic modulus (E) using an FHA structure and annealing-free mechanochemical synthesis. The general formula of the FHA SSE proposed is $Li_{5+x}Si_xSb_{1-x}S_4Br_yI_{2-y}$ (x = 0–0.3, y = 0–0.4). The researchers explored three key approaches for substituting cations and anions within the SSE structure. First, replace the central P^{5+} cation in the tetrahedron with a larger Sb^{5+} cation to create sufficient lattice space for halogen insertion. Second, utilize halogens with varying ionic radii to achieve bi-halogen tight packing, maximizing the incorporation of monovalent anion clusters between tetrahedra. Finally, partially substitute pentavalent Sb^{5+} with tetravalent Si^{4+} to enhance conductivity and increase Li-ion concentration through charge compensation. Notably, the SSE structure was optimized in large part due to the halogen selection. To optimize the mixed halogen effect, Br^- ions were added as a supporting role to the I^- ions. I^- ions were selected as the primary halogen element in the synthesized FHA225 material. The maximum conductivity of the $Li_{5.2}Si_{0.2}Sb_{0.8}S_4Br_{0.25}I_{1.75}$ (FHA225) was 13.23 mS cm^{-1} with lowest elastic modulus (Fig. 11a). The Wyckoff *4c* sites could also achieve an astounding total halogen occupancy of almost 90.67 %, breaking previous records [216]. This increased halogen occupancy promotes Li-ion hopping across cages, which lead to the conductivity increase that is seen. Fig. 11b shows the comparison of porosity as a function of compaction pressure between the partially halogenated $Li_{5.5}PS_{4.5}Cl$ (PHA1.5) and FHA225 SSEs. Due to higher halogen content inducing softness in the material, the porosity is found to be minimal for FHA225, which is beneficial for SSEs. Stable rate performance is also shown by FHA225 in Fig. 11c. Table 3 summarizes all the structural engineering strategies adopted for Li SSEs.

4. Structural engineering of sodium sulfide-based SSEs

Sodium and lithium, both alkali metals from Group 1 of the periodic

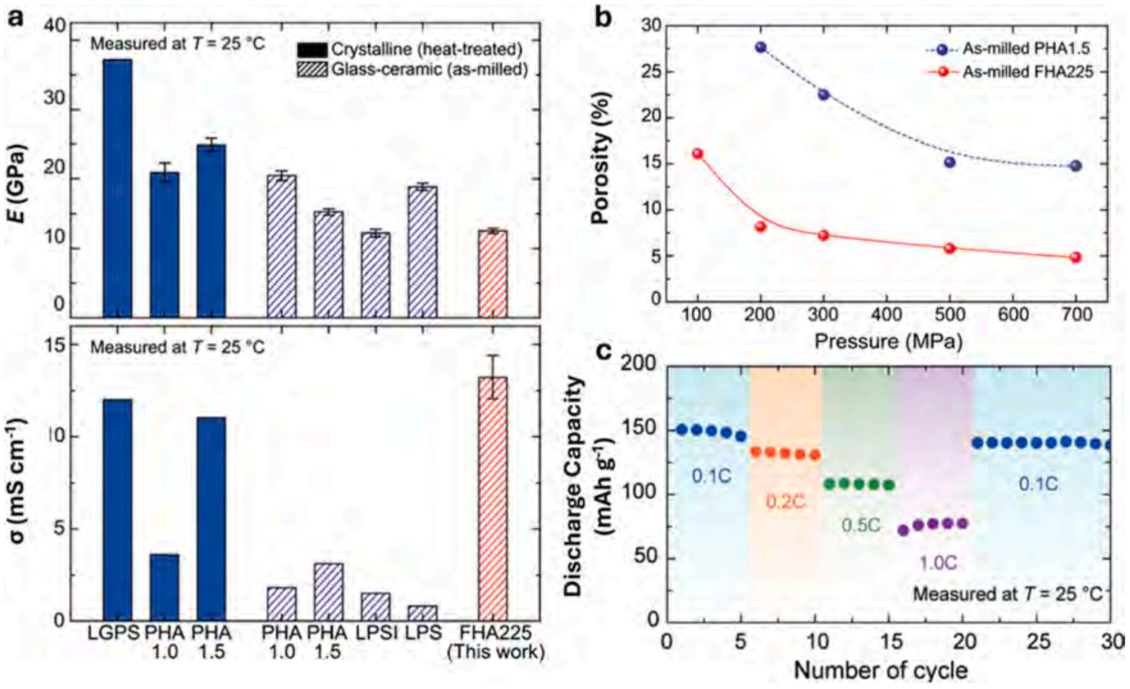

Fig. 11. (a) Comparison of elastic modulus and ionic conductivity of different crystalline/glass-ceramic sulfides, partially halogenated (PHA) and fully halogenated (FHA) SSEs. (b) Comparison of porosity as a function of compaction pressure for PHA1.5 and FHA225. (c) Rate performance (0.1 C, 0.2 C, 0.5 C, 1.0 C) of Nb-NMC811/FHA225/Li-In ASSB at T = 25 °C. Reproduced with permission from [220], copyright 2023, Wiley.

table, exhibit similar chemical properties due to their analogous electronic configurations. The development of sodium SSEs has closely followed that of lithium SSEs, including a range of materials such as oxides, sulfides, and polymers. While the fundamental principles governing ion transport and stability are comparable, sodium SSEs present unique challenges and opportunities due to differences in ionic radii, electronegativity, and material abundance [221–223]. Sodium SSEs, which contain mobile Na ions, have a lower electronegativity compared to Li ions. Consequently, sodium SSEs experience weaker electrostatic interactions with oxide or sulfide species in the crystal structure, which facilitates faster Na^+ diffusion. Additionally, the abundance and low cost of sodium make it a promising, sustainable alternative to lithium, further highlighting the need for tailored approaches to optimize the electrochemical performance and stability of sodium SSEs. Sodium sulfides SSEs stand out as one of the most promising candidates for commercial use due to their distinct advantages, including low synthesis temperatures of around 500 °C and rapid sodium-ion conduction at ambient temperatures. Additionally, they offer favourable mechanical properties such as softness, good ductility, and a low elastic modulus [16,224,225]. More importantly, cold pressing alone can form intimate electrode-electrolyte contact with reduced grain boundary resistance in the full cell assembly. This contrasts with the high temperature hot pressing requirements posed by the oxide-based SSEs. These characteristics not only simplify electrode-electrolyte contact during battery assembly but also reduce the production costs by avoiding lot of the high energy demanding synthesis processes like sintering and annealing. The unique combination of these properties presents an opportunity for researchers to innovate and develop novel and fast ion conducting sulfide sodium SSEs. However, sulfide-based electrolytes are challenged by issues related to their chemical stability, impossible air exposure, narrow electrochemical voltage window, limiting their applicability in sodium-ion batteries (SIBs) like LIBs. Nevertheless, addressing these stability concerns through continued materials discovery and modification efforts holds promise for unlocking the full potential of sulfide sodium SSEs in future sodium battery technologies [226].

The dominant type of sulfide SSEs include Na_3PS_4 and its isostructural compounds like Na_3PSe_4, Na_3SbS_4 etc. Na_3PS_4 crystallizes in three different crystal structures: (i) RT tetragonal α-phase ($P42_1c$), (ii) the high-temperature cubic β-phase ($I43m$), or (iii) the orthorhombic γ-phase (Fddd) [69]. Na_3SbS_4 offers a high conductivity of 2 mS cm^{-1} that surpasses many other oxide, polymers, and NASICON-type SSEs [227]. Another class is the $Na_{11}Sn_2PS_{12}$-type, synthesized by inspiration from the LGPS version by direct substitution of Li^+ with Na^+ ions. First principles calculations yielded the conductivity for $Na_{10}GeP_2S_{12}$ as 4.7 mS cm^{-1}, $Na_{10}SnP_2S_{12}$ as 0.94 mS cm^{-1}, and $Na_{10}SiP_2S_{12}$ as 10.3 mS cm^{-1} [228–230]. However, these greatly deviated from the experimental results due to greater number of impurity phases [231]. In addition, recent studies are seen on a new type of sulfide SSEs with elements from Group IIIA (e.g., B, Ga) such as Na_3BS_3 that can form insulating interlayer between the Na metal and the SSEs [232]. Thio-borate based $Na_3B_5S_9$ are also reported that contains super-tetrahedral clusters for facilitating 3D conduction [233]. For argyrodite Na SSEs, only a few computational studies suggest the potential for this structures, as experimental data is currently lacking [234]. Consequently, this section will primarily focus on Na_3PS_4 SSEs, which are more extensively covered in the available literature.

4.1. Structures of sodium sulfide SSEs

The tetragonal phase of sodium sulfide Na_3PS_4 SSEs, synthesized via the solid-state reaction method by Jansen *et al.* [111] in 1992, was indexed to the space group $P42_1c$ (No. 114) with lattice parameters a = 6.952 Å and c = 7.707 Å. The reported ionic conductivity was *ca.* 10^{-6} S cm^{-1} at 50 °C. Further experimentation revealed a phase transition from tetragonal to cubic at temperatures above 250 °C. For the cubic phase, the ionic conductivity at 510 °C was measured at 8.5×10^{-2} S cm^{-1}. The cubic phase, which presents a lower activation barrier than the tetragonal phase, is considered the preferred phase for Na_3PS_4. Jansen *et al.* also reported the tetragonal distortion in the crystal structure of Na_3PS_4, which was predicted to be absent in the cubic phase. Fig. 12a shows that sodium atoms are located at both face-centred and edge-centred positions. Specifically, sodium occupies the Na1(*6b*) (face- and

Table 3
Summary of structural engineering strategies to lithium sulfide solid state electrolytes.

Substitution Sites	**Composition**	**Ionic Conductivity (RT)**	**Voltage *vs* Lodium**
Halide	Li_6PS_5Cl [145]	0.79 mS cm^{-1}	1.3 V – 2.3 V
	$Li_6PS_5Cl_{0.5}Br_{0.5}$ [170]	3.63 mS cm^{-1}	-
	$Li_6PS_5Br_{0.5}I_{0.5}$ [145]	0.04 mS cm^{-1}	-
Lithium Vacancy (Excess halogenation)	$Li_{5.5}PS_{4.5}Cl_{1.5}$ [176]	14.5 mS cm^{-1}	1.8 V – 2.5 V
	$Li_5PS_4Cl_2$ [176]	1.69 mS cm^{-1}	1.8 V – 2.5 V
	$Li_{5.3}PS_{4.3}Cl_{1.7}$ [182]	17.0 mS cm^{-1}	-
	$Li_{5.5}PS_{4.5}Br_{1.5}$ [184]	4.17 mS cm^{-1}	-
	$Li_{5.3}PS_{4.3}Br_{1.7}$ [177]	11.0 mS cm^{-1}	-
	$Li_{5.3}PS_{4.3}Cl_{1.0}Br_{0.7}$ [178]	24.0 mS cm^{-1}	-
	$Li_{5.3}PS_{4.3}Cl_{0.7}Br_{1.0}$ [178]	26.0 mS cm^{-1}	-
	$Li_{5.4}Al_{0.2}PS_5Cl$ [188]	2.40 mS cm^{-1}	0.5 V – 5.0 V
	$Li_{5.7}Ca_{0.15}PS_5Cl$ [189]	5.20 mS cm^{-1}	-
	$Li_{5.55}Ca_{0.1}PS_{4.75}Cl_{1.25}$ [189]	6.80 mS cm^{-1}	-
	$Li_{5.3}Ca_{0.1}PS_{4.5}Cl_{1.5}$	7.70 mS cm^{-1}	-
	$Li_{5.35}Ca_{0.1}PS_{4.5}Cl_{1.55}$	10.2 mS cm^{-1}	-
Chalcogenide	Li_6PS_4SeBr [190]	3.90 mS cm^{-1}	-
	Li_6PSe_5I [191]	0.28 mS cm^{-1}	-
	$Li_{6.25}PS_{5.25-x}Te_xCl_{0.75}$ [192]	4.50 mS cm^{-1}	< 7.0 V
	$Li_{5.6}PS_{4.6}I_{1.4}$ [207]	2.00 mS cm^{-1}	-
Phosphorus	$Li_{6.3}P_{0.7}Si_{0.3}S_5Br$ [194]	2.40 mS cm^{-1}	-
	$Li_{6.3}P_{0.7}Si_{0.3}S_5I$ [196]	1.10 mS cm^{-1}	< 6.0 V
	$Li_{6.46}P_{0.54}Si_{0.46}S_5I$ [197]	2.00 mS cm^{-1}	-
	$Li_{6.6}P_{0.4}Ge_{0.6}S_5I$ [146]	5.40 mS cm^{-1}	-
	$Li_{6.5}[P_{0.25}Si_{0.25}Ge_{0.25}Sb_{0.25}]S_5I$ [198]	13.2 mS cm^{-1}	-
	$Li_{5.6}SbS_{4.6}I_{1.4}$ [199]	0.66 mS cm^{-1}	< 5.0 V
	Li_6SbS_5I [199]	0.17 mS cm^{-1}	3.0 V – 5.0 V
	$Li_{6.6}Si_{0.6}Sb_{0.4}S_5I$ [204]	14.8 mS cm^{-1}	-
	$Li_{6.75}Si_{0.75}Sb_{0.25}S_5I$ [203]	13.1 mS cm^{-1}	< 7.0 V
	$Li_{6.4}Ge_{0.4}Sb_{0.6}S_5I$ [204]	6.30 mS cm^{-1}	-
	$Li_{6.5}Ge_{0.5}Sb_{0.5}S_5I$ [205]	16.1 mS cm^{-1}	1.6 V – 2.6 V
	$Li_{5.2}Si_{0.2}Sb_{0.8}S_4Br_{0.25}I_{1.75}$ [220]	13.2 mS cm^{-1}	1.6 V – 2.6 V

edge-centred) and interstitial site Na2(*12d*) (between Na1(*6b*) sites) position in the cubic phase. However, in the tetragonal phases, only Na1 (*6b*) site is present as shown in white colour, which is bifurcated into two distinct sites: Na1(*2a*) and Na2(*4d*) sites (Fig. 12b) [235,236]. As the cubic structure contains extra Na^+ sites, it has significant positive impacts on Na^+ hopping and ionic conductivity compared to tetragonal structure. Further, phosphorus resides on the Wyckoff *2a* site while sulfur resides on Wyckoff *8c* sites. The PS_4^{3-} tetrahedra occupies the BCC structure and a total of two units are present per unit cell for both phases. The transport of Na^+ ions differ in both the phases. The jump in the cubic phase is from one Na1(*6b*) site to another Na1(*6b*) via face-sharing and distorted tetrahedron through a tiny deformed tetrahedral site Na2(*12d*). This results in an optimal 3D diffusion pathway, enabled by face sharing. In the tetrahedral phase, the Na ion diffusion is through the direct jump processes occurring between Na1(*2a*) and Na2 (*4d*) through a triangular plane as shown in Fig. 12b. The other route of the jump process would be through Na2(*4d*) – Na2(*4d*) jumps, however, it is generally not possible in the structure as they have an edge-sharing tetrahedra.

To identify the energy barrier of Na ion jumps in both the structure, Wang *et al.* [236] performed NEB based DFT simulation. The transition energy barrier of Na^+ jump in the tetragonal Na_3PS_4 between Na1(*2a*) and Na2(*4d*) sites is recorded at 0.100 eV, surpassing the barrier observed in cubic Na_3PS_4, which stands at 0.058 eV, for jumps between Na1(*6b*) and Na1(*6b*) via Na2(*12d*) in the face sharing tetrahedra, as clearly shown in Fig. 12c-d. This conveys that 3D diffusion in cubic phase is beneficial and poses lower activation energy barrier. These findings align with the notable conductivity disparity observed between the two phases: while the desired cubic electrolyte demonstrates a room temperature ionic conductivity of 2×10^{-4} S cm^{-1}, the tetragonal electrolyte exhibits a significantly lower conductivity of 1×10^{-7} S cm^{-1}. Famprikis *et al.* [69] identified an orthorhombic crystal structured Na_3PS_4 that evolved above 500 °C, as observed from the XRD patterns. The phase transition temperatures identified by them are tetragonal to cubic (above 220 °C) and cubic to orthorhombic (above 500 °C). This orthorhombic Na_3PS_4 SSE is indexed to the Fddd space group with lattice parameters of a = 6.6055 Å, b = 11.7143 Å, and c = 20.7378 Å. The proposed complex crystal structure of the orthorhombic Na_3PS_4 as obtained from AIMD simulations is shown in Fig. 12e. Owing to the complex structure with multiple Na^+ diffusion pathways, the recorded conductivity was an order of magnitude higher than cubic phase (*ca.* 400 mS cm^{-1} with 0.11 eV at 550 °C (orthorhombic) *vs.* 40 mS cm^{-1} with 0.39 eV at 450 °C (cubic)). Extreme high temperature conductivity tests provide information on the structural resilience, maximum mobility of carrier ions possible and the corresponding performance achievable.

The RT conductivities of tetragonal, cubic, and complex orthorhombic Na_3PS_4 SSE phases are currently insufficient for commercialization in sodium SSBs. However, given their promising performance at high temperatures, there is potential to improve RT conductivity through strategic modifications. Among these three phases, the cubic phase is the most promising for rapid Na^+ ion conduction due to its favourable crystal structure, which provides abundant Na^+ ion sites and well-defined 3D diffusion pathways. Its relatively simple structure also facilitates further modifications. Like Li^+ ion SSEs, various structural engineering methods have been applied to Na^+ SSEs, including inducing vacancies, and substitutions at halide, chalcogenide, and phosphorus sites.

4.2. Sodium site substitutions and vacancy engineering

Klerk *et al.* [235] provided further insights into the impact of inducing Na^+ vacancies in the sulfide sodium SSE (Na_3PS_4). Without Na vacancy, almost negligible Na-ion mobility between the Na1(*6b*) sites was seen because of deficiency of the interstitial sites in the transition pathways for both the t/c-Na_3PS_4. However, as the vacancy was induced up to a concentration of 2 % for the stoichiometry $Na_{2.94}PS_4$, the MD simulations indicated the initiation of Na ion mobility by the creation of interconnections between the Na1(*6b*) and Na2(*12b*) pathways in both crystal structures, as visible from Fig. 13a-b. Highest conductivity of both phases was observed for $Na_{2.5}PS_4$ (17 % vacancy) to be 0.42 S cm^{-1} in comparison to 0.01 S cm^{-1} at 523 K for 0 % vacancy. To elaborate more on the impact of Na^+ vacancy by substituting halogen ions on the sulfur sites, Chu *et al.* [238] reported the Cl^- substitution charge compensated vacancies in t-Na_3PS_4 SSE with the general formula t-$Na_{3-x}PS_{4-x}Cl_x$. With Cl^- substitution of 0.0625 mol or 6.25 % in the structure yields the stoichiometry as t-$Na_{2.9375}PS_{3.9375}Cl_{0.0625}$. It showed a high conductivity of 1.14 mS cm^{-1} at 303 K with a barrier of 0.24 eV, which is 21 times higher conductive than t-Na_3PS_4. Huang *et al.* [239] provided further insights using first principles MD investigations and a conductivity of 1.07 mS cm^{-1} for 1.56 % of Cl^- substitution, consistent with Chu *et al.* Additionally, they estimated an even higher conductivity of 2.37 mS cm^{-1} with lowest barrier of 0.24 eV for Br-doped $Na_{47}P_{16}S_{63}Br$.

Feng *et al.* [240] developed a method to selectively substitute Cl^- ions on S^{2-} ions without creating Na^+ ion vacancies, resulting in a t-$Na_3PS_{3.8}Cl_{0.2}$ (Cl = 0.2 mol or 20 %) stoichiometry. It provided reduced energy barrier and a room temperature ionic conductivity of 1.96 mS cm^{-1}. This substitution strategy, which does not induce Na^+ vacancies but still enhances conductivity, is primarily effective due to the identification of defects that facilitate rapid ion transport. Maximizing of these functional defects is shown to be crucial for ion conduction. The study identified defective structural sites labelled as Na3

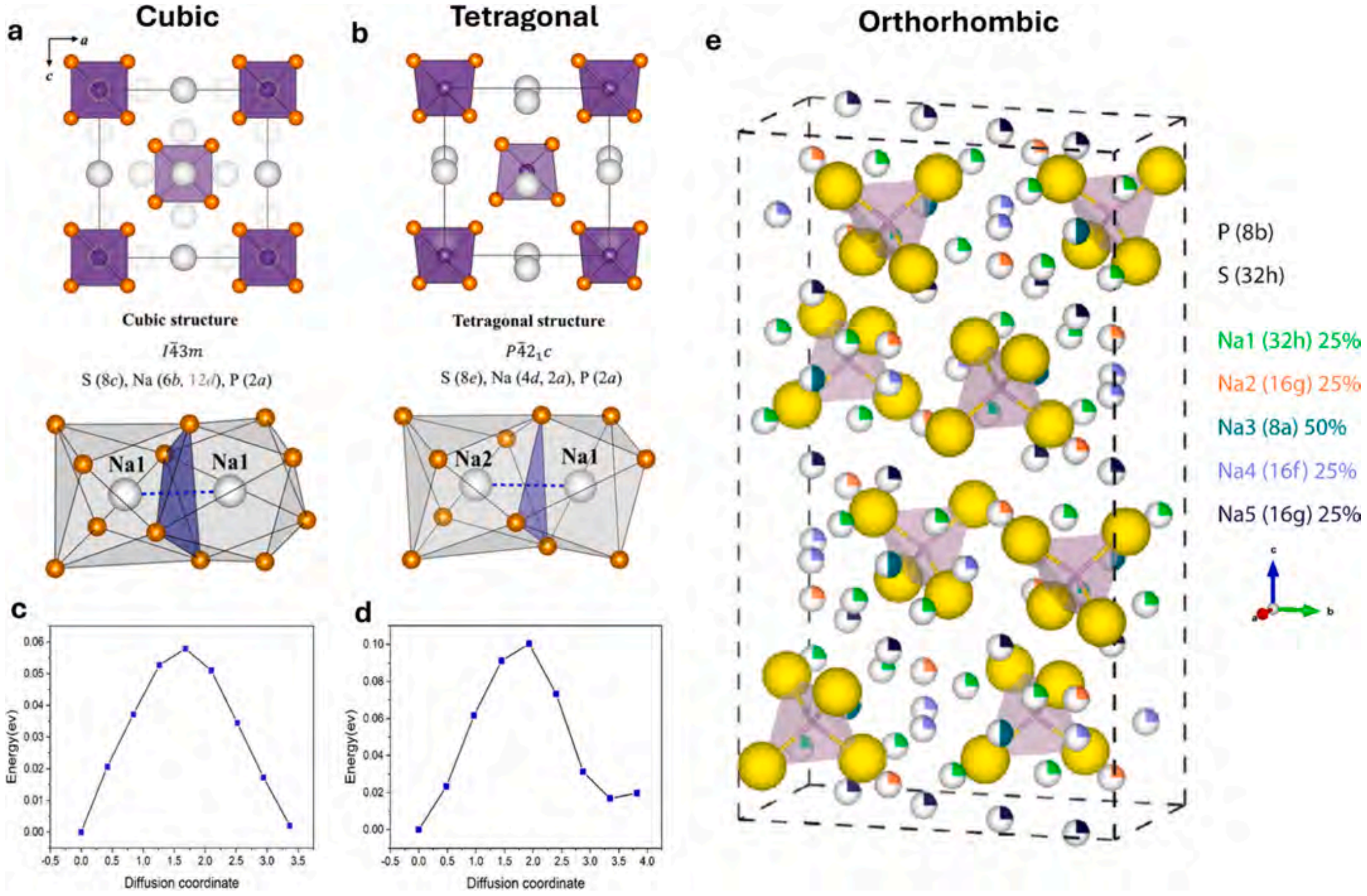

Fig. 12. Crystal structure of c-Na_3PS_4 (a) and t-Na_3PS_4 (b), respectively and the positions of phosphorus (purple), sulfur (orange), Na1(*6b*) (white) and Na2(*12d*) (transparent white) sites. Na ion migration pathways are also indicated under respective crystal structure. (c) Sodium ion activation energy barrier for the tetragonal and (d) cubic phased Na_3PS_4, respectively. (e) Orthorhombic structure of Na_3PS_4 as obtained from ab initio calculations.
(a-b) Reproduced with permission from [237], copyright 2016, American Chemical Society. (c-d) Reproduced with permission from [236], copyright 2021, Institute of Physics. (e) Reproduced with permission from [69], copyright 2019, American Chemical Society.

and Na4 with Cl^- substitution in the charge balanced t-$Na_{3-x}PS_{4-x}Cl_x$ using high-resolution solid-state magic-angle-spinning (MAS) ^{23}Na NMR (Fig. 13c). Further, tracer-exchange NMR experiments with Li^+ ions replacing the Na^+ ions under a biased electric potential were performed on t-$Na_{3-x}PS_{4-x}Cl_x$. This technique is performed by sandwiching the sodium SSE between the two Li-metal foils. Under applied potential, Li^+ ions are allowed to diffuse through the SSE wherein they replace the active Na^+ ions. Fig. 13d illustrates the comparison of ^7Li with ^{23}Na tracer exchange and it shows the reduction in the Na3 and Na4 resonances and an increase in the Na1 and Na2 sites resonances. In t-$Na_{2.8}PS_{3.8}Cl_{0.2}$, the introduction of Li ions into Na vacancies (Na4 site) leads to a transformation of vacancies to neighbouring Na sites, specifically from Na4 to Na1 and Na2, thus an increase in the intensity of Na1/Na2 and consequent decrease in Na4 intensity. Consequently, the reduction in active Na3 ions signal arises from the replacement of ^{23}Na with ^7Li, thus showing that Na3, positioned adjacent to Cl, serves as the pivotal site for ion conduction within the system. Thus, minimizing Na vacancy formation to prevent Na1 and Na2 sites formation while maximizing Na3 sites for ionic transport is a beneficial optimization strategy for ionic conductivity. To further test this, the Na vacancies in t-$Na_{2.9}PS_{3.9}Cl_{0.1}$ were filled by introducing controlled NaCl amount experimentally (t-$Na_{2.9}PS_{3.9}Cl_{0.1}$/zNaCl (z = 0.1, 0.3, 0.5)). For z = 0.1, the stoichiometry is t-$Na_3PS_{3.8}Cl_{0.2}$, ionic conductivity increased to 1.96 mS cm^{-1} at RT. Another method for inducing vacancies in Na_3PS_4 is doping with alkaline earth metals that have higher valence states. Moon *et al.* [241] experimentally substituted the Ca^{2+} ions on the Na(*2a*) sites in the t-$Na_{3-2x}Ca_xPS_4$ SE. They observed tetragonal to cubic phase transformation upon substitution, which further increased the conductivity to 0.94 mS cm^{-1} for c-$Na_{2.73}Ca_{0.135}PS_4$ (Fig. 13e). Remarkably, the activation energy rose as the Ca^{2+} concentration did as well. This was explained by the fact that the surrounding Na^+ vacancies were trapped by the more positively charged Ca^{2+} ions, creating a high migration barrier. The full cell performance with TiS_2/Na-Sn electrodes showed remarkable cycling stability and delivered a high specific capacity of 150 mAh g^{-1} at 0.11 C even after 120 cycles, as shown in Fig. 13f.

4.3. *Chalcogenide sites substitution*

In solid-state materials, replacing sulfur with a bigger chalcogenide ion, like selenium, shows great potential for improving ion conductivity as seen in Li^+ argyrodites case. Due to selenium's higher ionic size, this deliberate replacement may offer more advantageous ion transport paths to much larger Na^+ ions because of wider diffusion pathways and polarizable lattice. Cedar's group [121] reported the first synthesis of a selenium replaced sulfur, c-Na_3PSe_4 that yielded a conductivity of 0.11 mS cm^{-1} at RT and a low barrier of 27 KJ mol^{-1} in the cold-pressed state. This is comparable to the Na_3PS_4 version. Another advantage of using bigger chalcogenide ions is that it eliminates the need for high temperature sintering thus preventing associated side reactions. DFT and AIMD simulations reveal that pure Na_3PSe_4 exhibits negligible Na^+ ion diffusivity, even at 900 K, making it a very poor ion conductor. However, introducing a small amount of Na vacancies (2 %) significantly enhances Na^+ ion diffusion greatly. To further confirm these results of AIMD, NEB calculations were performed by Bo *et al.* [121].

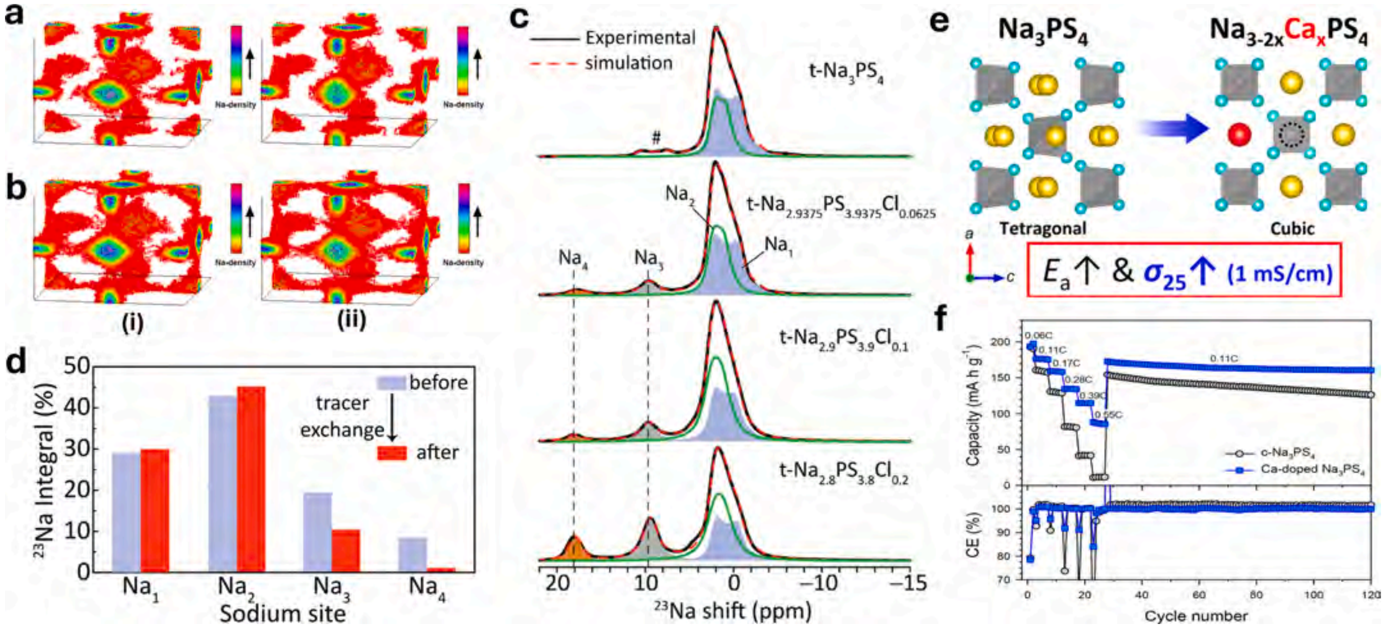

Fig. 13. (a) Na-ion density distribution from MD simulation at 523 K for (i) c-Na$_3$PS$_4$ and (ii) t-Na$_3$PS$_4$. (b) After inducing sodium vacancies for (i) c-Na$_{2.94}$PS$_4$ and (ii) t-Na$_{2.94}$PS$_4$. (c) Impact of Cl$^-$ substitution on the evolution of functional defects (Na3 and Na4) in t-Na$_{3\text{-}x}$PS$_{4\text{-}x}$Cl$_x$ (x = 0, 0.0625, 0.1, and 0.2) from ^{23}Na MAS NMR. (d) Comparison of ^{7}Li with ^{23}Na tracer exchange experiments on the resonances of all Na sites. (e) Structural schematic after Ca^{2+} doping on Na$^+$ site in Na$_3$PS$_4$ showing the evolution of Na vacancy and structural transformation from tetragonal to cubic. (f) Electrochemical cycling performance of TiS$_2$/Na$_{2.7}$Ca$_{0.15}$PS$_4$/Na-Sn for different c-rates at 30 °C.

(a-b) Reproduced with permission from [235], copyright 2016, American Chemical Society. (c-d) Reproduced with permission from [240], copyright 2019, Wiley. (e-f) Reproduced with permission from [241], copyright 2018, American Chemical Society.

Fig. 14a shows the plot of Na ion vacancy migration as a function of activation energy in Na$_3$PSe$_4$. In the transition state, the activation energy for Na vacancy migration is slightly less than 0.05 eV. This corresponds to an ionic conductivity of 29 mS cm^{-1} at room temperature, indicating that selenide-based defective systems are superior to S doped Na$_3$PX$_4$ (X = S, Se) systems and they provide efficient and larger pathways for rapid Na$^+$ diffusion. Following on this, the same group [242] showed that a number of variables, including temperature, reaction vessel, and precursor mass, affect the synthesis process of c-Na$_3$PSe$_4$. As the amount of selenium increases, there is a steady expansion of volume along with a shift from tetragonal to cubic phase change.

Zeier's group [237,243] investigated the changes in the lattice dynamics with Se doping. A decrease in the speed of sound and Debye frequencies with Se-doping are the first observations, like the Li$^+$ case, that indicate the softening of the anion's framework. Although lattice polarizability expands the diffusion channels and decreases the activation energy, the ionic conductivity is not much enhanced. This happens due to the accompanying fall in the Debye frequencies and Arrhenius pre-factor, as also seen in Li$_6$PS$_{5\text{-}x}$Se$_x$Cl [191,244]. Upon seeing the better impacts of Sb-doping in the Na$_3$PS$_4$ SSE (discussed in the next section), Wang *et al.* [245] synthesized a single phase Sb-substituted c-Na$_3$P$_{1\text{-}x}$Sb$_x$Se$_4$. These compounds exhibit excellent ionic conductivity and low activation energy; the substitution of Sb enlarges the unit cell and improves ion transport. Reported ionic conductivity was 3.7 mS cm^{-1} at RT for x = 1. A very recent study by the Zeier group [246] explored the impacts of static (structural changes) and dynamic (bonding interactions) changes in a cationic and anionic substitution series involving Na$_3$P$_{1-x}$Sb$_x$S$_4$, Na$_3$P$_{1-x}$Sb$_x$Se$_4$, Na$_3$PS$_{4-y}$Se$_y$, and Na$_3$SbS$_{4-y}$Se$_y$ systems. Fig. 14b represents the Arrhenius plot of all the systems. Structural analyses of these systems after cationic and anionic doping reveal complex changes in unit cell volumes, PnCh$_4^{3-}$ (Pn = P, Sb; Ch = S, Se) polyhedral volumes, Ch-Ch bond distances. Obtained results indicated that volume changes behave differently with different types of modifications and that monotonic increase/decrease cannot be expected. While comparing the impacts of static changes on the activation barrier, the authors considered Ch-Ch distance to represent the bottleneck size of the diffusion channels (Fig. 14c). A clear reducing trend in activation energy as a function of bottleneck size is obvious from the plot for both cationic and anionic substitution as both lead to increase in the diffusional channel volumes. However, inconsistency in the rate of decrease in the activation energy is observed (cationic substitution has steeper drop in barrier). The authors argue that if larger Ch–Ch bottleneck distances were the sole determinant of reduced activation energy, then the largest drop in activation energy should occur in systems where substitution leads to the greatest increase in Ch–Ch distances. However, this is not consistently observed. For instance, in anion substitutions like Na$_3$PS$_{4-y}$Se$_y$ and Na$_3$SbS$_{4-y}$Se$_y$, a 4 % increase in the Ch–Ch distance is present, but a significant reduction in activation energy is only noted in Na$_3$PS$_{4-y}$Se$_y$. This discrepancy suggests that relying solely on geometric descriptors—such as diffusion pathways and bottleneck sizes—provides an incomplete explanation of activation energy variations. Instead, the authors propose the use of macroscopic thermodynamic descriptors, such as melting temperature and anharmonic bulk modulus (Bγ), as more reliable indicators of lattice dynamics. These properties, determined for Na$_3$PS$_4$, Na$_3$SbS$_4$, Na$_3$PSe$_4$, and Na$_3$SbSe$_4$, reveal a clear correlation between decreasing melting temperatures, softer lattices, and reduced activation barriers (Fig. 14d). Weaker bonding interactions in softer lattices lead to flattened vibrational potentials and lower energy requirements for ion migration. Furthermore, the correlation between Bγ and activation energy demonstrates that softer lattices with lower Bγ values exhibit reduced activation barriers, particularly in Sb-substituted compounds as shown in Fig. 14e. This highlights that lattice dynamics, characterized by softer structures and weaker bonding, play a crucial role in lowering the energy barrier for ion transport. In contrast, geometric factors such as Ch–Ch distances do not show a consistent relationship with activation energy, reinforcing that dynamic descriptors like Bγ and melting temperatures are more reliable predictors of ion conductivity in SSEs. The authors emphasize the importance of considering these dynamic properties over geometric ones when assessing activation barrier trends.

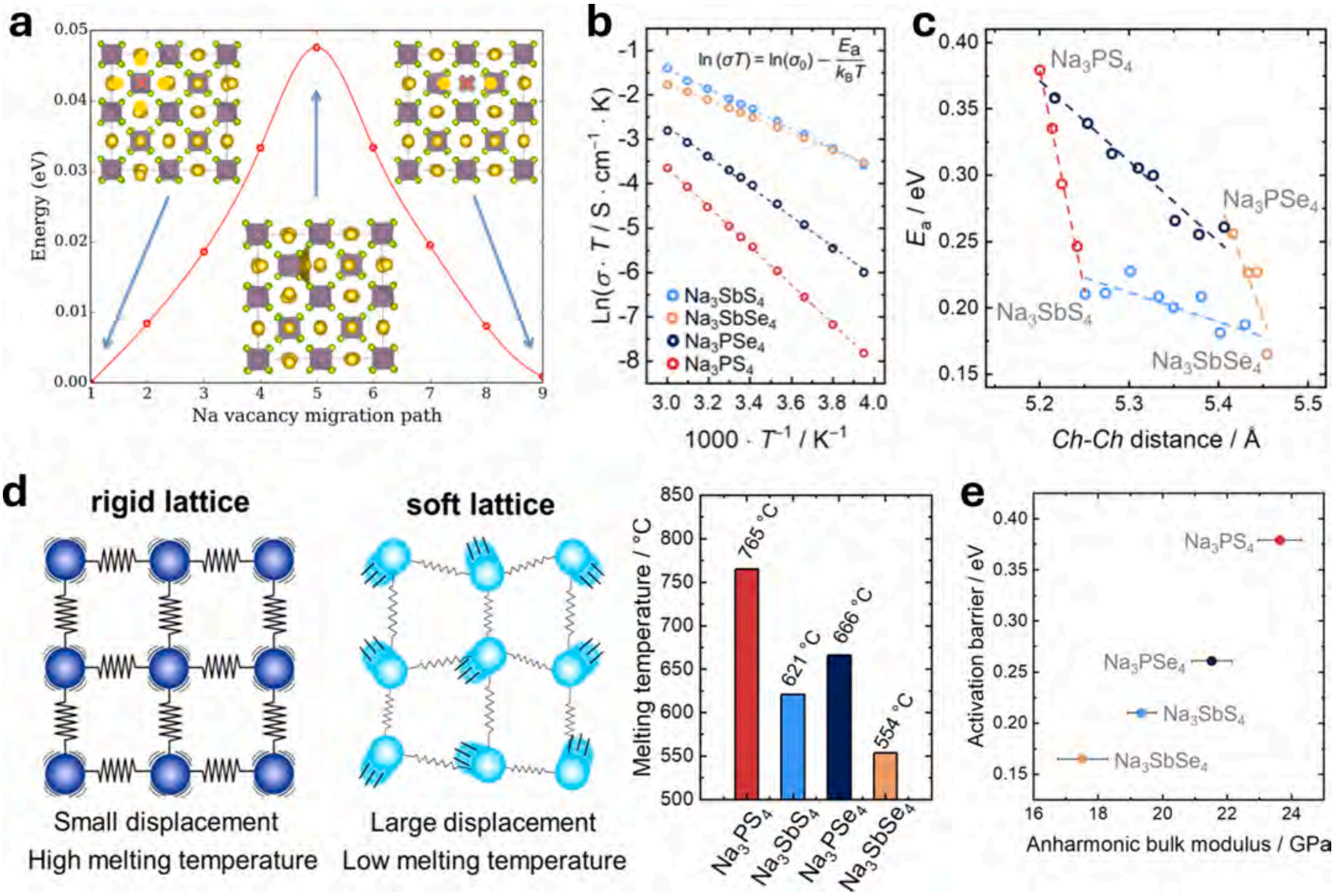

Fig. 14. (a) Na ion vacancy migration as a function of activation energy in Na_3PSe_4. Final states are represented on the left and right sides and transition state in the middle. Na atoms are represented in yellow, Se atoms in green, and Na vacancy is represented by a cross mark. (b) Arrhenius plots in the temperature range of −20–60 °C for Na_3PS_4, Na_3SbS_4, Na_3PSe_4, and Na_3SbSe_4. (c) Plot of activation energy changes as a function of Ch-Ch (Ch = S, Se) distances, a potential measure of diffusional channel bottleneck size. (d) Schematic of the relationship between displacement and melting temperature for hard and soft lattices. Rigid lattice is displayed by stronger spring to indicate greater bond strength and vice versa in soft lattices. Corresponding melting temperature for different system is shown. (e) Variation of activation energy with anharmonic bulk modulus, a potential benchmark of dynamic changes like lattice softening and bond strengths in truly accessing activation energy variation.

(a) Reproduced with permission from [121], copyright 2016, American Chemical Society. (b-e) Reproduced with permission from [246], copyright 2022, American Chemical Society.

4.4. *Phosphorus site substitutions*

Substitutions at the phosphorus site enhance ionic conductivity and improve air and moisture stability. This approach, like those used in lithium-ion SSEs, involves substituting the P^{5+} ions in the sodium sulfide Na_3PS_4 SSE with aliovalent cations. This approach can either introduce excess Na^+ ions or induce vacancies, depending on the oxidation state of the dopant. For examples the substitution of 6 % of a lower valence Si^{4+} ion on the P^{5+} ion site in c-Na_3PS_4 induces extra Na ions in the structure and leads to an increase in ionic conductivity to 0.74 mS cm^{-1}, as shown by Tanibata *et al.* [247]. This was mainly attributed to the increased Na site occupancy on the Na2(*12b*) transition site in $94Na_3PS_4{\cdot}6Na_4SiS_4$ glass ceramic SSE [248]. With the increase of the Si^{4+} dopant to 10 %, enhanced thermodynamic stability was further seen for $94Na_3PS_4{\cdot}10Na_4SiS_4$. In addition, the introduction of larger aliovalent dopants like (M = Ge^{4+}, Sn^{4+}, Ti^{4+}), in contrast to smaller Si^{4+}, on the P^{5+} site in the general formula $Na_{3+x}M_xP_{1-x}S_4$ (x = 0.1) displays overcrowding of the Na sites and is proven to be important in enhancing the ionic conductivity and Na migration by Rao *et al.* [249]. Highest conductivity is observed only with Sn-doped $Na_{3.1}Sn_{0.1}P_{0.9}S_4$ (x = 0.1), which is 0.25 mS cm^{-1} and with improved cyclability at 2 C. However, this experimental results deviated from the AIMD simulation performed by Zhu *et al.* [250] that predicted a conductivity of 10 mS cm^{-1} for 6.25 % of Sn doping. Their results convey lowest activation energy for 6.25 % Sn-doped sample. The van Hove correlation function G_d at 800 K is shown in the Fig. 15a for Si, Ge, and Sn dopants at same concentrations. The Van Hove function describes the probability of finding a particle at a certain distance from a reference point over time, helping to analyze particle dynamics in a system. It consists of two parts: the self-part $G_s(r,t)$, which represents the likelihood of finding the same particle at a distance r, after time t, given that it was at the origin at time t = 0 and the distinct-part $G_d(r,t)$, which indicates the probability of finding a different particle at distance r, at time t, with the original particle located at the origin at t = 0. In the figure, the $G_d(r,t)$ for all dopants show an intense peak at r = 0, indicating that Na^+ ions are exhibiting correlated motion. However, for the Sn-doped sample, $G_d(r,t)$ starts to exhibit a strong peak starting nearly at 1 picosecond, in contrast to 7–11 picoseconds for other samples. This indicates that the correlated motion in Sn-doped sample is happening very earlier with higher diffusion constant. Authors relate this to increasing free channel volume with larger Sn doping. Despite these computational findings, the lower valence ion substitutions (oxidation state of +4) have not shown to be particularly encouraging in the Na_3PS_4 systems mainly because it fails to attain the higher solubility limit as it introduces additional Na^+ ions into

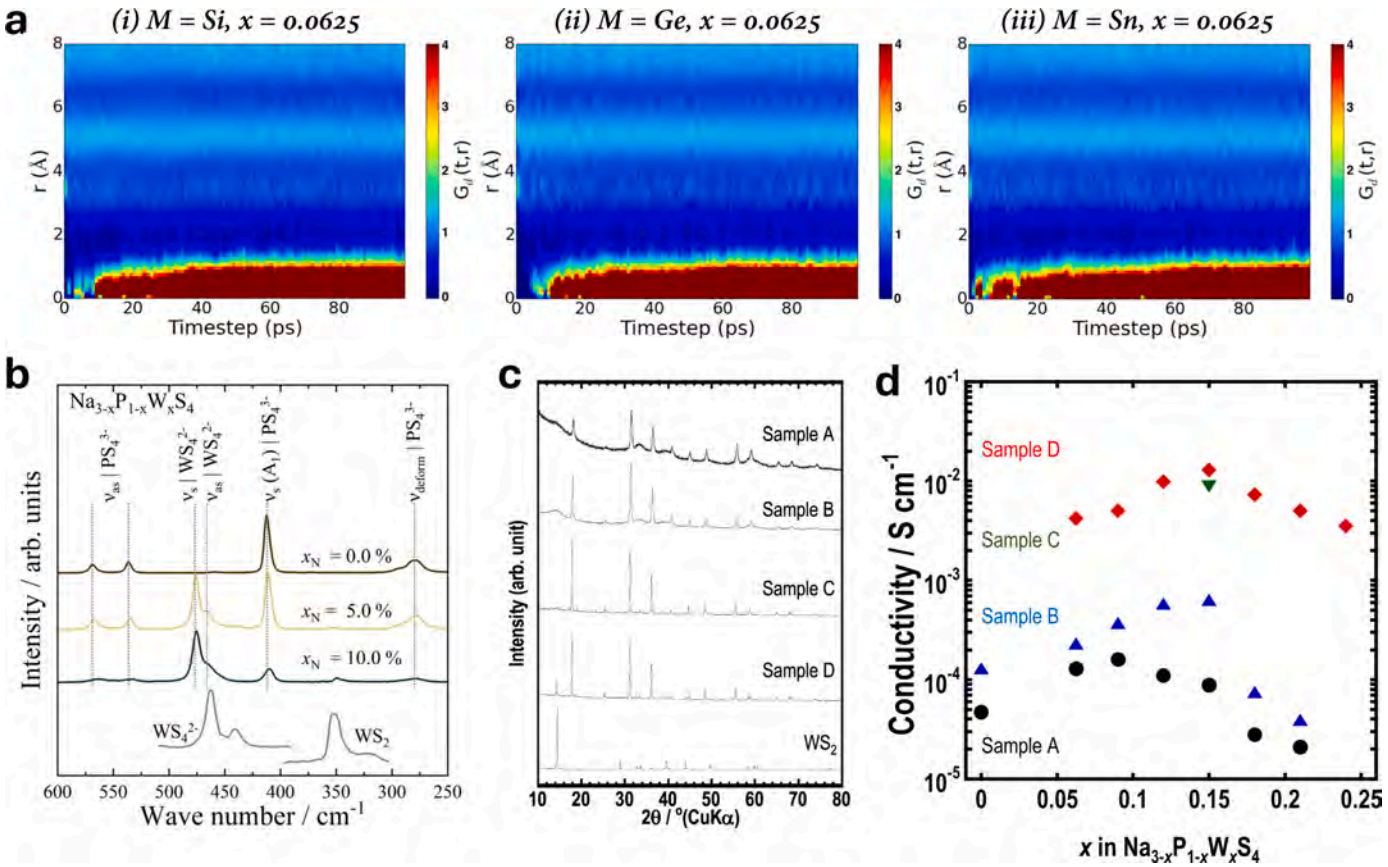

Fig. 15. (a) van Hove correlation functions $G_d(r,t)$ for (i) $Na_{3.0625}Si_{0.0625}P_{0.9375}S_4$, (ii) $Na_{3.0625}Ge_{0.0625}P_{0.9375}S_4$, and (iii) $Na_{3.0625}Sn_{0.0625}P_{0.9375}S_4$. All samples indicate intense peak at r = 0, implying correlated motion. (b) Raman spectrum of $Na_{3\text{-}x}P_{1\text{-}x}W_xS_4$ for x = 0, 5, and 10 mol%. Presence of $WS_4^{2\text{-}}$ polyanion is confirmed for all mol% along with the starting precursor WS_2. (c) XRD patterns of $Na_{2.85}P_{0.85}W_{0.15}S_4$ for different sample preparation methods and (d) their respective ionic conductivity values at RT.

(a) Reproduced with permission from [250], copyright 2015, American Chemical Society. (b) Reproduced with permission from [253], copyright 2020, American Chemical Society. (c-d) Reproduced with permission from [254], copyright 2021, Elsevier.

the smaller structure of Na_3PS_4.

An alternative approach is to introduce an even higher valence state ions such as, W^{6+}, that also results in the creation of sodium vacancies, which is found to be crucial for fast mobility in the previous sections and also presented in literature [239,251,252]. Fuchs *et al.* [253] performed this interesting study by substituting W^{6+} in Na_3PS_4 and obtaining $Na_{2.9}P_{0.9}W_{0.1}S_4$ (x = 0.1) via solid-state method. This substitution strategy resulted in the highest ionic conductivity of 13 mS cm^{-1} at RT. However, their Raman spectra of the as-synthesized SSE show the presence of the starting precursor WS_2 (Fig. 15b). Synthesis of the homogenous Na-ion SSE without any residual elements is crucial for the long term cyclability. Thus, in the following year, Tsuji *et al.* [254] experimented four different synthesis procedures to obtain the homogeneous W^{6+} substituted Na_3PS_4. Four different synthesis procedures included mechanochemical milling of precursors at 510 rpm for 15 hours [sample A], heat-treatment in Argon at 220 °C for 2 hours [sample B], heat-treatment in vacuum at 550 °C for 20 hours [sample C], and a direct solid-state method involving heat treatment in vacuum for 20 hours at 550 °C [sample D]. From the XRD spectra of each synthesis process (Fig. 15c), the crystallinity of the SSE clearly increases with temperature. While the sample C and sample D has the same heat treatment protocol, the full width at half maximum (FWHM) at 2θ = 31.2° for sample D was 0.1173°, lower than 0.1205° for sample C. This indicates that sample D has slightly higher crystallinity. Despite that, the lattice parameters of all samples are relatively same. Interestingly, the WS_2 crystals are not observed in the samples A, B, and C, but sample D did exhibit 7 % crystalline WS_2. This was mainly the cause of the pre-mechanochemical milling that reacted all the starting precursors. Interestingly, the solubility limit of W^{6+} was increased in their experiment up to 15 mol% ($Na_{2.85}P_{0.85}W_{0.15}S_4$), that yielded a conductivity of 13.7 mS cm^{-1} and 8.8 mS cm^{-1} at RT for samples D and C (sample C is semi crystalline), respectively (Fig. 15d). These results underscore the importance of crystallinity of the synthesized electrolyte, synthesis procedures, and compositional control in optimizing the conductivity.

Aliovalent doping in the sulfide Na SSEs structure impacts the ionic conductivity by either increasing or decreasing the mobile ion concentrations and defects. Majorly, doping of heavier aliovalent elements is done to enlarge the parent structure for larger diffusion channels, lower activation barrier and a greater number of mobile charge carriers. Isovalent doping emerges as another strategy in deconvoluting the impacts of mobile ion concentration and activation barrier on conductivity. As seen in the Li section, Sb substitutions has seen positive impacts in both ionic conductivity and air stability, which is also applied to the Na based systems. Lee *et al.* [255] in their very recent study have studied the impact of doping lighter and heavier iso-valent transition elements (V, Nb, Ta) on the Sb site in $Na_3Sb_{1-x}M_xS_4$ (M = V, Nb, Ta) to understand the impacts of mobile ion concentration and mobility (altered migration barrier) on conductivity. Complete substitution of these ions have been reported previously reported in the literature [256–258]. The tetragonality, as indicated by the higher c/a ratio, has been found to be lowest for the V^{5+} substituted sample due to its smaller size than Sb^{5+} ion and higher shrinking c-axis in contrast to a-axis lattices. The conductivity plot also displays the impact of tetragonality on the ionic conductivity (Fig. 16a-b). Nb and Ta doping displays a monotonic

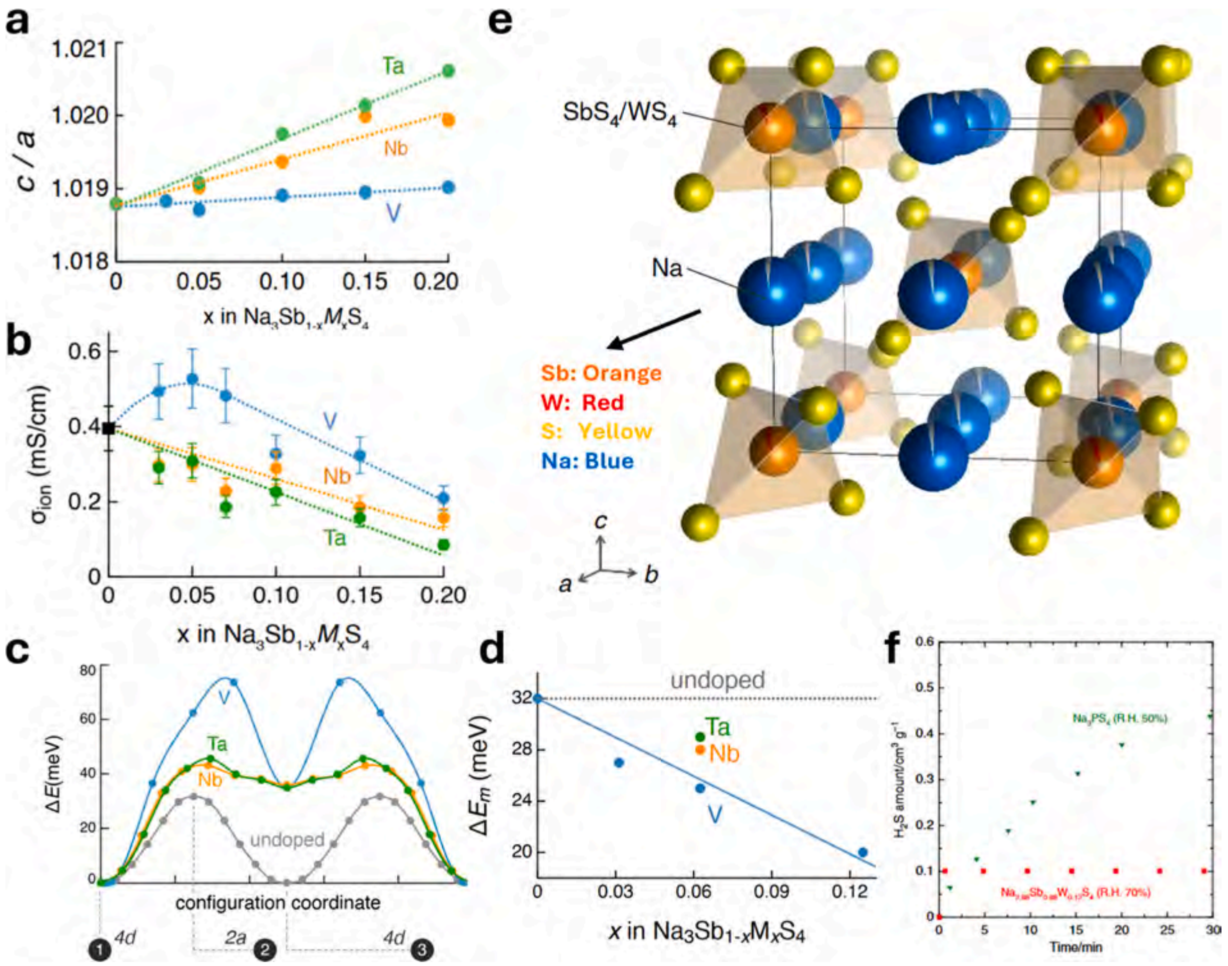

Fig. 16. (a) Variation in the tetragonality parameter (c/a) and (b) ionic conductivity with iso-valent doping of M = (V, Nb, and Ta) in $Na_3Sb_{1-x}M_xS_4$. (c) Impact of local effect (motion of mobile ions in doped-SSE while maintaining undoped-SSE cell parameters for simulation) on the migration barrier of Na ions. (d) Impact of global effect (motion of mobile ions in an undoped-SSE while maintaining the doped-SSE cell parameters for simulation) on ion migration. (e) Crystal structure of c-$Na_{2.88}Sb_{0.88}W_{0.12}S_4$ synthesized from ball milling and heat treated at 275 °C for 12 hours. (f) Evolution of H_2S gas amounts for Na_3PS_4 and c-$Na_{2.88}Sb_{0.88}W_{0.12}S_4$ with relative humidity of 50 % and 70 %, respectively.
(a-d) Reproduced with permission from [255], copyright 2024, the authors. (e-f) Reproduced with permission from [260], copyright 2019, Nature.

decrease in the conductivity whereas V^{5+} ($x = 0.05$) shows increased conductivity followed by steep decrease. To investigate the competing local and global effects, the energy barrier has been calculated in two different scenarios: the motion of Na ions in the presence of dopants while maintaining the cell parameters of an undoped SSE (local effect), and the motion of Na ions in a cell with volume adjusted to reflect the presence of dopants without explicitly placing the dopants nearby (global effect). From the Fig. 16c-d, the local migration barrier increases in the order of the Nb>Ta>V, indicating that the Na ions in the vicinity of these dopants face higher migration barrier. Whereas the global migration barrier decreases with all dopants, but V doping reduces the migration barrier 2X times due to shrinking volume of the unit cell. The global effect barrier does not account for the presence of the dopants. It indicates that for iso valent doping, competing effects are at play that influences the conductivity. The local effects generally dominate at higher concentrations as shown by decreasing conductivity for V^{5+} at higher doping levels. In contrast, the global effects start to prevail at lower concentrations and account for much larger decrease in the barrier. Smaller iso-valent dopants on P/Sb site can also be a good strategy for enhanced conductivity and lower barrier. These dopants facilitate global structural effects, even at low concentrations, where the reduction in migration barrier outweighs any competing local effects that may be caused. Possibility of ion percolating pathways with local structural changes have been previously shown by [259]. In addition, smaller dopants are found to make stiffer bond with sulfur ions, thereby loosening the SbS_4^{3-} tetrahedra and can also help in softening of the parent framework and reduce the interactions with mobile ions.

4.5. Air stability in phosphorus substituted SSEs

Phosphorus substitutions play a pivotal role in enhancing air and moisture stability, offering advantages not typically observed with the other strategies as discussed earlier. These substitutions directly address the primary challenge in sodium-ion SSEs—namely, their susceptibility to hydrolysis and instability against sodium metal—like the issues faced by lithium-ion SSEs. The application of the hard acid base theory (HSAB) offers insights into addressing these concerns. A hard acid (P^{5+}) interacts with a hard base (O^{2-}) from the water molecule and tends to displace a soft base (S^{2-}), forming H_2S gas and a defective crystal structure. This significantly impedes the overall ionic conductivity [261]. To enhance air and moisture stability and promote Na mobility, substituting the hard acid (P^{5+}) ion with softer acid ions like Sb^{5+} or As^{5+} to reduce the interaction with O^{2-} (hard base) emerges as a promising strategy in the sodium ion SSEs as well. In the crystal structure of Na_3MS_4 (M = Sb, As), this substitution also weakens the bond strength between the M-S bonds in the MS_4^{3-} tetrahedra, facilitating easier Na^+ diffusion. Substitution of larger M^{5+} for P^{5+} ions also broaden the diffusion channels that could benefit the movement of Na ions. To test the hypothesis of HSAB in the sodium sulfide SSEs, Zhang *et al.* [262] synthesized the t-Na_3SbS_4 for the first time through solid-state reaction, which was indexed to $P42_1c$ space group with a = b= 7.1597 Å, c = 7.2906 Å. Interestingly, it presented an ionic conductivity of 3 mS cm^{-1} at RT compared to 0.2 mS cm^{-1} obtained for Na_3PS_4. In addition, unlike the stoichiometric Na_3PS_4, the new t-Na_3SbS_4 reveals an existence of 2.5 mol% Na vacancies at Na1(*2a*) sites from the XRD data [121]. Existence of these Na vacancies benefit towards the ionic conductivity, as shown by Klerk *et al.* [235]. This synthesis of replacing Sb^{5+} with P^{5+} led to several different researchers exploring this avenue. For instance, the same group [112] synthesized a c-Na_3SbS_4 (a = b = c = 7.191 Å) that proved be a stable phase at RT as well as have superior stability at even 200 °C. Fig. 17a shows the diffraction pattern of the t-Na_3SbS_4 and c-Na_3SbS_4. The inset in Fig. 17a is the diffraction pattern of t-Na_3SbS_4 where two small tetragonal peaks at 28° and 37.5° are visible in contrast to the cubic XRD pattern. The Ionic conductivity of the cubic phase is 2.8 mS cm^{-1}, approximately same as the tetragonal phase however they differ significantly in the activation energy. The activation energy calculated for c-Na_3SbS_4 is 0.06 eV, significantly lower than 0.25 eV of t-Na_3SbS_4. In addition, Wang *et al.* [261] synthesized Na_3SbS_4 from $Na_3SbS_4.9H_2O$, also known as Schlippe's salt, and proved its stability in ambient atmosphere. They exposed Na_3SbS_4 to air at 70 % humidity for 48 hours and conducted Raman and XRD tests on the pristine $Na_3SbS_4.9H_2O$, as-prepared Na_3SbS_4, as-exposed Na_3SbS_4, and reheated Na_3SbS_4 (Fig. 17b). Both the Raman and XRD spectrums of the air-exposed sample resembles that of the pristine $Na_3SbS_4.9H_2O$ sample. These results reaffirm the HSAB theory that Sb^{5+} (soft acid) can strongly bond with a soft base S^{2-} and maintain its chemical properties. Moreover, the air-exposed sample's reversible water absorption/desorption behaviour is further highlighted by heating it to 150°C that helps to restore the pure Na_3SbS_4 phase.

Apart from the typical solid-state method of synthesizing sodium sulfide SSEs, Banerjee *et al.* [263] synthesized the Na_3SbS_4 SSE with a scalable solution liquid-phase synthesis method using methanol or water. This method, however, fails to achieve the crystallinity as observed by the typical solid-state methods, thus, the conductivity observed is around 0.2 mS cm^{-1} at RT. Very recently, Yan et al. [264] developed a low-cost synthesis method to produce high purity Na_2S used in the synthesis in Na_3SbS_4 (Fig. 17c). They prepared their Na_2S by performing hydrogen reduction reaction on Na_2SO_4 by supplying Ar/H_2 gas at 750 °C for 20 hr during sintering. Crude Na_2S was dissolved in ethanol to remove impurities and later distilled to separate both the compounds. Pure Na_2S was obtained after heat treatment at 400 °C for 2 hours, which was verified by XRD results and the white colour of the product. It showed superior ionic conductivities and low activation barrier in the range of 30–100 °C compared to commercial ones. Full cells performance with TiS_2/NaSn electrodes was also found to be superior in contrast to commercially obtained Na_3SbS_4 (C-NSS-L), shown in Fig. 17d. Moreover, Liang *et al.* [261] produced a pure c-Na_3SbS_4 SSE from the naturally occurring salt (Na_3SbS_4·9 H_2O), which is also a precursor for the preparation of antimony pentasulfide (Sb_2S_3). By removing the crystalline water molecules from the Na_3SbS_4·9 H_2O salt by heating it to 150 °C in vacuum, they could create c-Na_3SbS_4 with

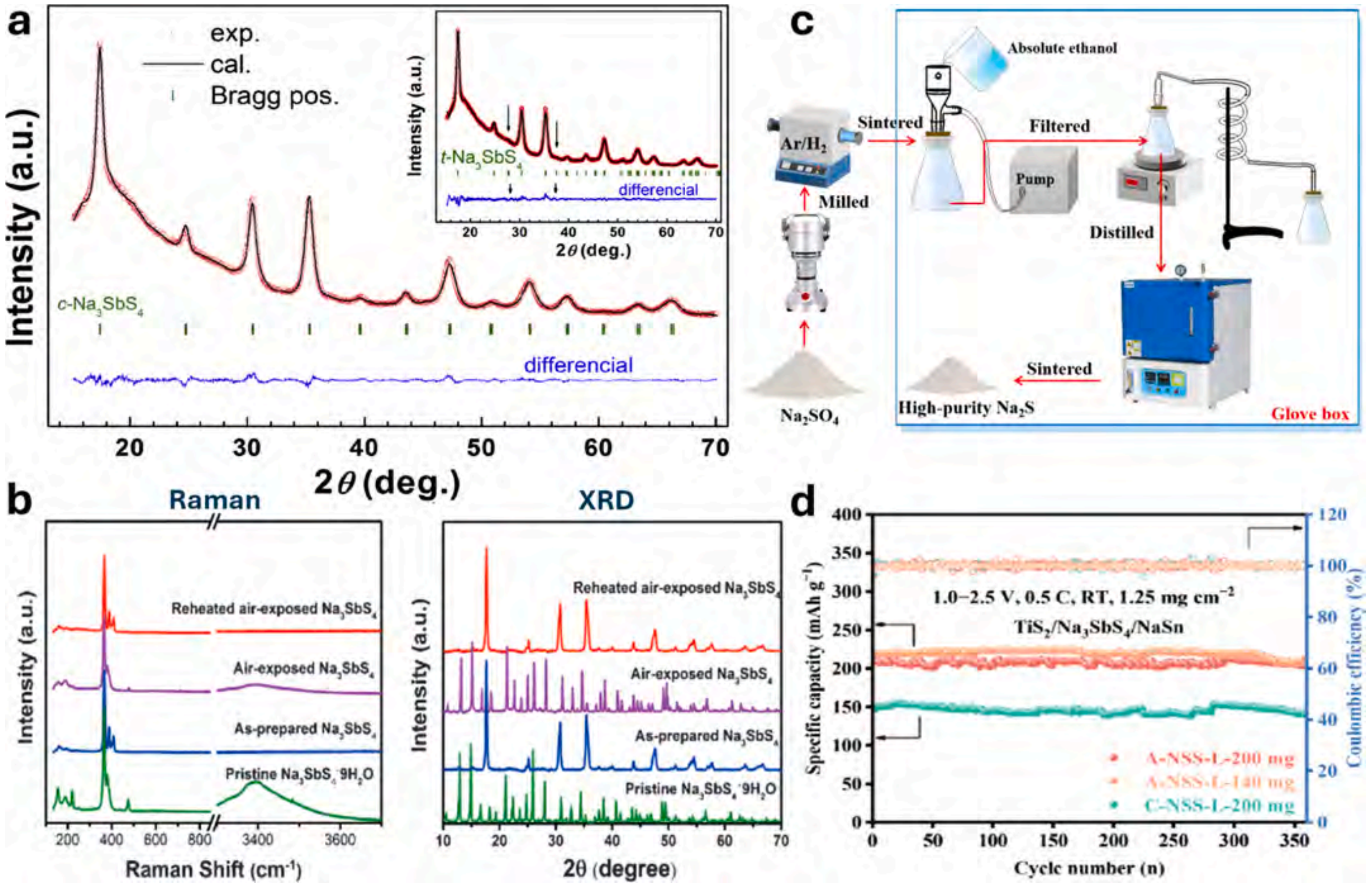

Fig. 17. (a) Rietveld refinements patterns from X-ray diffraction of ball milled c/t-Na_3SbS_4. (b) Raman and XRD spectrums of pristine $Na_3SbS_4.9H_2O$, as-prepared Na_3SbS_4, as-exposed Na_3SbS_4 in air (48 h), and reheated Na_3SbS_4 after air exposure (150 °C for 1 h in vacuum). (c) Schematic of a low-cost synthesis and purification process to synthesize Na_2S in glovebox. (d) Full cell cycling performance of NaSn/TiS_2 electrodes at RT using commercially obtained Na_3SbS_4 (C-NSS-L-200mg) and as-synthesized Na_3SbS_4 SSEs (A-NSS-L-200mg and lower loading 140 mg). The voltage windows and c-rate are 1.0–2.5 V and 0.5 C, respectively.
(a) Reproduced with permission from [112], copyright 2018, Elsevier. (b) Reproduced with permission from [261], copyright 2016, Wiley. (c-d) Reproduced with permission from [264], copyright 2024, Elsevier.

improved stability in moist air and a high conductivity of 1 mS cm^{-1} [265].

The following year of the first synthesis of t-Na_3SbS_4, Yu *et al.* [266] reported a new SSE with partial substitution of As^{5+} on P^{5+} with the general formula of $Na_3P_{1-x}As_xS_4$ (x = 0–1). They reported a RT conductivity of 1.46 mS cm^{-1} for $Na_3P_{0.62}As_{0.38}S_4$ (x = 0.38), which was higher than the 0.2 mS cm^{-1} of c-Na_3PS_4. As^{5+} substituted SSE also displays far superior moisture stability, thereby supporting the HSAB theory. Full substitution of As^{5+} in $Na_3P_1.xAs_xS_4$, i.e. x = 1 or 100 mol%, generates a lower conductivity of 0.027 mS cm^{-1}. The Na-S bond length emerges as a critical determinant of Na-ion diffusivity and conductivity (Fig. 18a). The presence of the partial As^{5+} ions introduce lattice expansion, promoting longer bond lengths between Na-S in the initial state (IS) of the migration step. In the transition state (TS), the Na-S bond length is maximum at x = 0.5 as well as show an inverse relationship with the migration energy. Conversely, at higher As^{5+} concentrations, more As^{5+} ions are available than the P^{5+} ions to interact with S^{2-} ions. Since As-S bonds would be longer and weaker compared to P-S bonds due to HSAB theory, this results in the creation of more loosened and freer S^{2-} ions from the AsS_4^{3-} tetrahedra that instead gets strongly attracted to the Na^+ ions. This creates stronger Na-S bond strength that shortens the Na-S bond lengths. Stronger and shorter Na-S bonds (maximum As^{5+} substitution) increase the minimum migration energy of Na^+ ion diffusion through the SSE, causing lower conductivity. This work was further supported by computational work involving first principles and phonon calculations from the same group [267]. They demonstrated that $Na_3P_{1-x}As_xS_4$ exhibits notable moisture stability when x > 0.25 because the reaction products change from easily forming oxysulfide's to more difficult-forming hydrates because of As–O bonds lower affinity of formation than P–O bonds. As a result of promising features showcased by the replacement of P^{5+} ions by individual As^{5+} and Sb^{5+} ions, Yin et al. [268] combined the dopants to form a high conducting $Na_3Sb_{1-x}As_xS_4$. Partial doping of As^{5+} on Sb^{5+} creates a greater number of cubic phases and crystalline crystal structure. While the $Na_3Sb_{0.75}As_{0.25}S_4$ possesses a conductivity of 2.42 mS cm^{-1} that is slightly higher than their Na_3SbS_4 version, the major improvement is observed on the air and moisture stability. Upon exposure to air at RH 50 % for 30 mins, the $Na_3Sb_{0.75}As_{0.25}S_4$ releases 0.017 cm^3/g of H_2S gas as compared to very higher amount of 0.05 cm^3 g^{-1} of H_2S for the undoped Na_3SbS_4 (Fig. 18b). In addition, the unchanged Raman spectra after air exposure clearly displays the structural stability of this As-doped Na SSEs (Fig. 18c).

While HSAB theory has proven valuable in the design of solid-state electrolytes (SSEs) with enhanced moisture stability and long-term cyclability, achieving the desired level of ionic conductivity remains a challenge. Several work on the aliovalent substitution on the newly developed Na_3YS_4 (Y = Sb, As) has been performed to learn the impact of partial substitution, introduction of excess Na, or inducing Na vacancies. For example, Yu *et al.* [269] partially substituted Ge^{4+} in $Na_{3+x}Sb_{1-x}Ge_xS_4$ and obtained a doubled conductivity of 5 mS cm^{-1} at

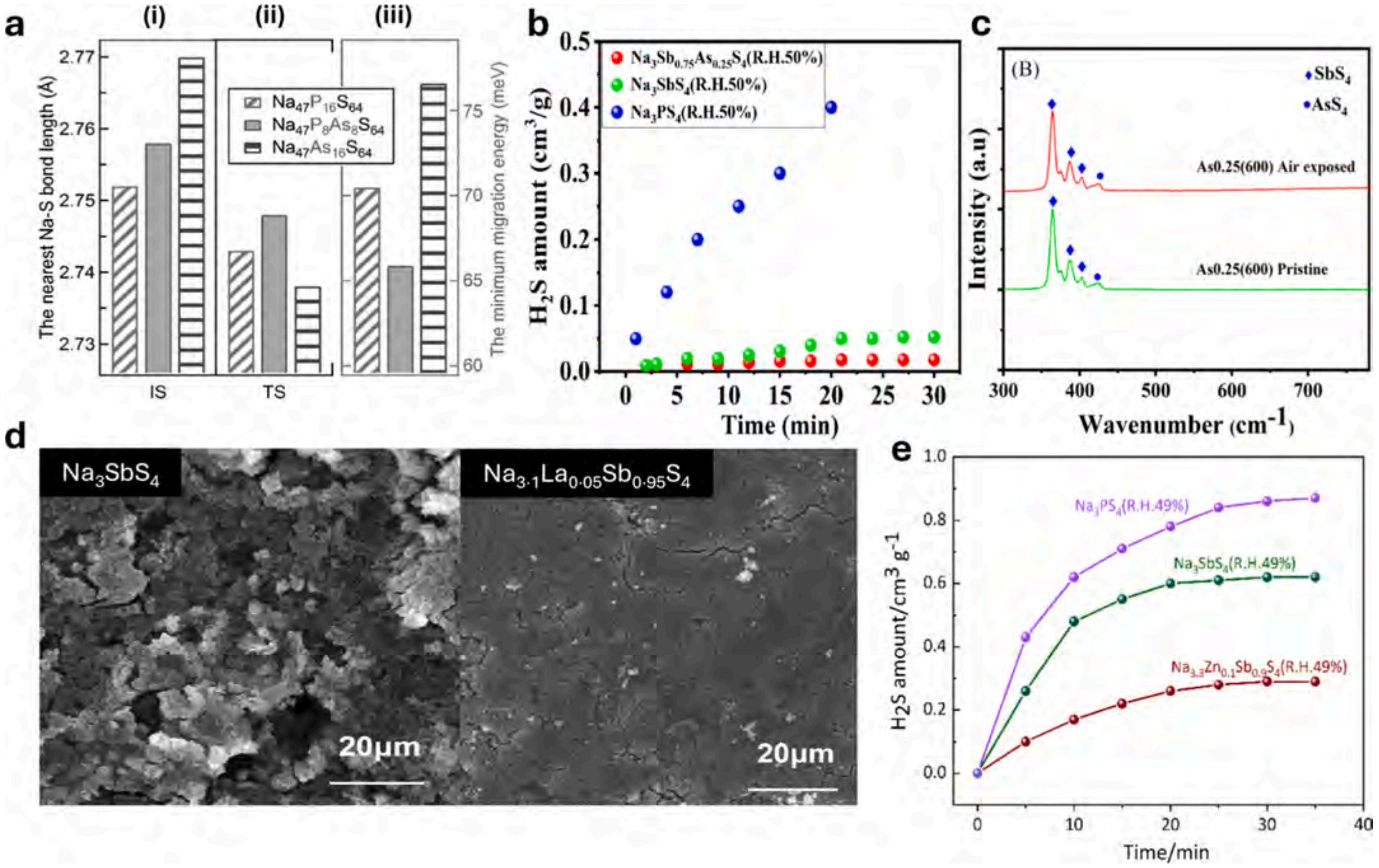

Fig. 18. (a) Comparison of nearest Na-S bond lengths (Å) and (a-iii) the minimum migration energy (eV) for $Na_{47}P_{16}S_{64}$, $Na_{47}P_8As_8S_{64}$ (partially doped with As^{5+}), and $Na_{47}As_{16}S_{64}$ (fully doped with As^{5+}) at the initial states (IS) (a-i) and transition states (TS) (a-ii) of Na migration. Compositions are adjusted to reflect one Na vacancy. Partial As^{5+} doping is equivalent to $Na_3P_{0.5}As_{0.5}S_4$. (b) Amount of H_2S gas generated for three compositions of Na_3PS_4, Na_3SbS_4 and $Na_3Sb_{0.75}As_{0.25}S_4$ upon exposure to humid air with relative humidity of 50 %. (c) Raman spectra comparison of $Na_3Sb_{0.75}As_{0.25}S_4$ before and after exposure to air. (d) SEM images of Na_3SbS_4 and $Na_{3.1}La_{0.05}Sb_{0.95}S_4$. (e) The correlation between H_2S release and time for three distinct samples—Na_3PS_4, Na_3SbS_4, and $Na_{3.3}Zn_{0.1}Sb_{0.9}S_4$—measured at RH of 49 %.

(a) Reproduced with permission from [266], copyright 2017, Wiley. (b-c) Reproduced with permission from [268], copyright 2024, Wiley. (d) Reproduced with permission from [270], copyright 2024, Elsevier. (e) Reproduced with permission from [271], copyright 2024, Springer.

RT for x = 0.1, compared to pristine 2 mS cm^{-1} of Na_3SbS_4. This proved possible by interstitial sodium defects caused by higher number of mobile charge carriers in a larger unit cell size of Na_3SbS_4. Lowered energy barrier of 0.156 eV was reported. Recently, Lu *et al.* [270] studied the impacts of doping lower valence rare earth element La^{3+} on Sb^{5+} site. La^{3+} possesses a larger radius than Sb^{5+} (103.2 pm vs 60 pm), and so broadening of the diffusion channels and concomitant increase in the Na^{+} interstitials were directly observed [100]. Due to significantly larger size of the La^{3+} ion, doping above 0.05 mol% restrained the formation of Na_3SbS_4 units. SEM images reveals a key difference by La^{3+} doping (Fig. 18d). Without any doping, isolated particles of Na SSE are visible that also are random and irregular in shapes. With La-doping, a more uniform crystal growth and densified surface can be observed that also reduces the grain boundary resistance in the cold pressed state. The $Na_{3.1}La_{0.05}Sb_{0.95}S_4$ stoichiometry heat treated at 450 °C displays a modest conductivity of 0.52 mS cm^{-1} with an extremely low barrier of 0.069 eV and enhanced air stability. As a result of very low energy barrier, the 450 °C treated La-doped Na_3SbS_4 can maintain its conductivity for a wide range of temperatures. Fu *et al.* [271] tested a lower valent Zn^{2+} ion (74 pm) as an aliovalent dopant in the same class of SSEs to synthesize $Na_{3+3x}Zn_xSb_{1-x}S_4$ ($0 \leq x \leq 0.2$). Zn^{2+} leads to overcrowding of the Na^{+} interstitials and charge carrier density. Doping results in a uniformly distributed surface, and enhances conductivity to 1.48 mS cm^{-1} with a 0.128 eV barrier at 550°C. It also improved air stability, reducing H_2S release by half compared to the undoped sample (Fig. 18e).

Given the significant performance improvements achieved by substituting higher valence state ions at the P^{5+} sites in Na_3PS_4, applying a similar strategy to Na_3SbS_4 as the base solid electrolyte is promising. Hayashi *et al.* [260] performed mechanochemical method with heat treatment to dope W^{6+} ions on the Sb^{5+} sites to synthesize c-$Na_{3-x}Sb_{1-x}W_xS_4$. For x = 0.12, they achieved a highest conductivity of 32 mS cm^{-1} at RT, which is till date superior to the state-of-the-art Li^{+} SSEs [86,215]. Fig. 16e shows the crystal structure of $Na_{2.88}Sb_{0.88}W_{0.12}S_4$. The introduction of W^{6+} stabilizes the cubic phase thereby allowing easier diffusion. Further, the heat treatment directly impacts ionic conductivity and energy barrier. Moreover, the $Na_{2.88}Sb_{0.88}W_{0.12}S_4$ electrolyte was found to be more resistant to the production of H_2S gas at an RH of 70 % in an ambient environment compared to the Na_3PS_4 at a lower RH of 50 % (Fig. 16 f). Fuchs *et al.* [253] synthesized solid solutions of $Na_{3-x}Sb_{1-x}W_xS_4$, and as well achieved the highest reported conductivity of 41±8 mS cm^{-1} for x = 0.1. Introduction of W^{6+} has proved to decrease the tetragonal distortion by increasing *a* lattice and decreasing *c* lattice of the structure. This leads to better Na⁺ diffusion and improved conductivity. While the ionic conductivity of both $Na_{2.88}Sb_{0.88}W_{0.12}S_4$ and $Na_{2.9}Sb_{0.9}W_{0.1}S_4$ SSEs were higher, the authors also reported a higher activation barrier of 0.21 eV and 0.18 eV compared to the pristine Na_3SbS_4 SSE with only 0.06 eV. Feng et al. [272] further tuned the local environment of these SSEs to achieve lesser activation barrier by heavy W-doping. Their stoichiometry possessed an orthorhombic structure and displaced a conductivity of 14.5 mS cm^{-1} with a low barrier of 0.12 eV. Interestingly, the synthesis did not display WS_2 impurities in the SSEs from Raman spectra (Fig. 19a). From the theoretical study, the fast-ion conduction has been explained by evolution in spatial structural features. The heavy W-doped system consist of four types of cationic rows: first - Na-Na-Na-Na, second - Na-Sb-Na-Sb, third – Na-Sb-Na-W, fourth – Na-W-Na-W. Only first and second rows are found in Na_3SbS_4, the presence of third and fourth rows

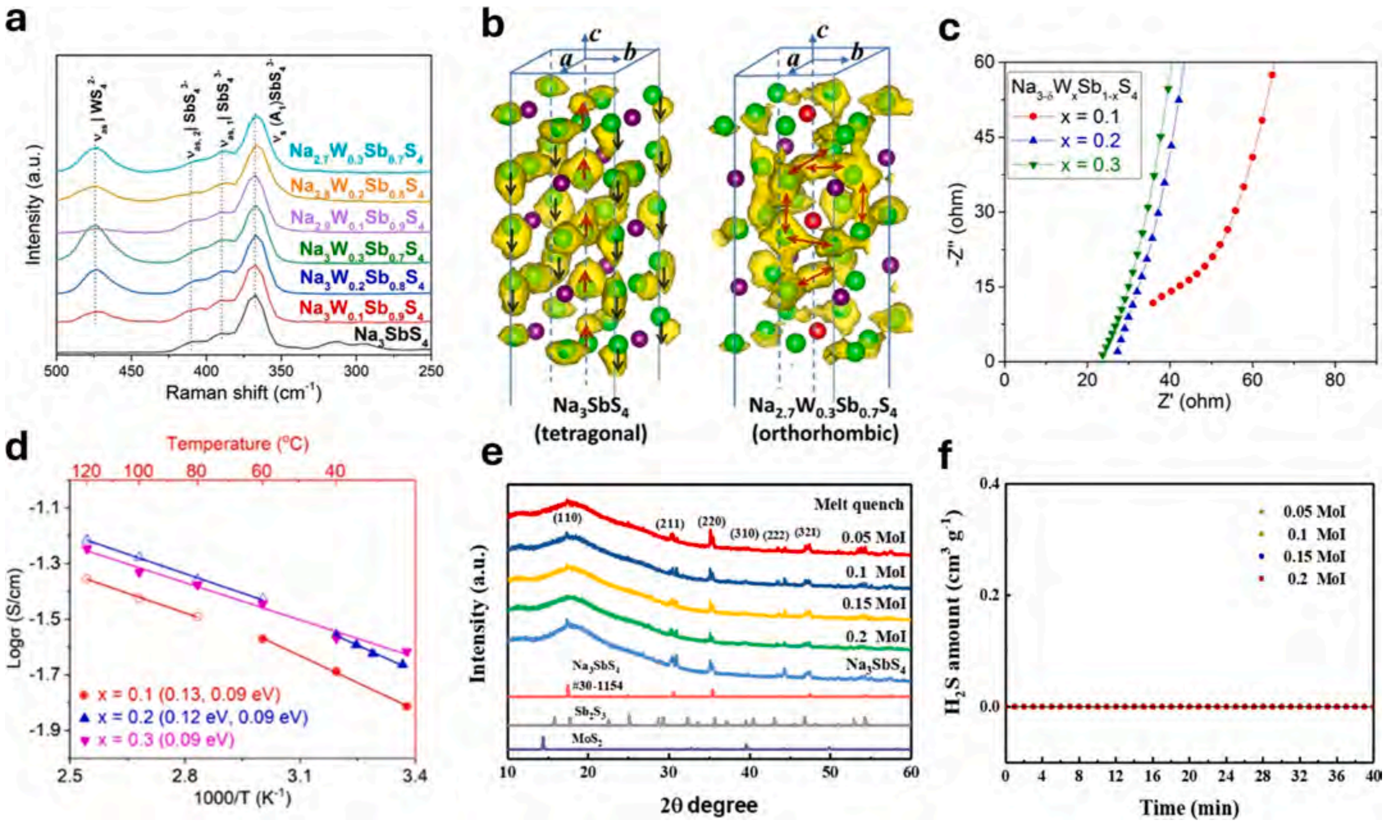

Fig. 19. (a) Comparison of Raman spectrums of pristine Na_3SbS_4 and as-synthesized $Na_{3-x}W_xSb_{1-x}S_4$, $Na_{3-y}W_xSb_{1-x}S_4$ (x = 0.1, 0.2, 0.3; 0<y<x). (b) Probability distribution functions and iso-surfaces (in yellow) for the pristine Na_3SbS_4 and vacancy induced $Na_{2.7}W_{0.3}Sb_{0.7}S_4$. Different atoms are indicated by: Na (light green), Sb (purple), W (red). (c) EIS values for the excess Na and pseudo cubic structured SSE with the stoichiometry $Na_{3-y}W_xSb_{1-x}S_4$ (x = 0.1, 0.2, 0.3; 0<y<x) and (d) Ionic conductivity plots for the same SSE in the temperature range of 20 °C to 120 °C. Reproduced with permission from [272], copyright 2021, Wiley. (e) XRD patterns of $Na_{(3-2x)}Sb_{(1-x)}Mo_xS_{(4-x)}I_x$ (x = 0.05, 0.1, 0.15, 0.2) prepared via melt-quenching method using excess S. (f) Monitoring of H_2S gas by MoI-doped Na_3SbS_4 when exposed to moist air for 40 mins. Reproduced with permission from [274], copyright 2021, Elsevier.

enable strong correlation between Na ions and these ions can jump into the indued Na vacancies in the Na-Na-Na first row to achieve correlated motion. The impact of these correlated motions is also shown in the calculated probability distribution functions iso-surfaces of Na ion movement in Fig. 19b. In the case of t-Na_3SbS_4, the Na-ion movement is only possible in the cationic rows aligned in the c-axis (Na-Na-Na), thus making it a 1-D conduction. In the c-axis, each Na ion is coordinated by 6 S atoms with longer Na-S bond lengths. However, along the a and b axes, the Na ions are coordinated by 6 and 8 S atoms with shorter Na-S bond lengths, making it difficult for 3-D conduction. In the case of W-doped SSE, W^{6+} interacts very strongly with the four S bonds and forms shorter W-S bonds. As a result, W atoms in the third and fourth row can attract the S ions much strongly thereby reducing the Na-S attractions. This drops the Na ion activation barrier in $Na_{2.7}W_{0.3}Sb_{0.7}S_4$ significantly and causes conduction in a and b axes. This experimental data is also supported in the computational simulation by Ravalli *et al.* [273]. They propose that the diffusion coefficient significantly increases as the W content increases. This is primarily supported by increasing interconnection between the *ab* planes because of shrinking c-axis, which is a symbol of lower tetragonal distortion by W-doping. Building on this and with the idea that excess mobile ions can improve correlated motion, the authors synthesized $Na_{2\text{-}y}W_xSb_{1\text{-}x}S_4$ ($x = 0.1, 0.2, 0.3$; $0<y<x$) SSE with a pseudo-cubic structure and excess Na ions. The $Na_{2.895}W_{0.3}Sb_{0.7}S_4$ stoichiometry showed the lowest bulk resistance of 23.7 ohms and RT

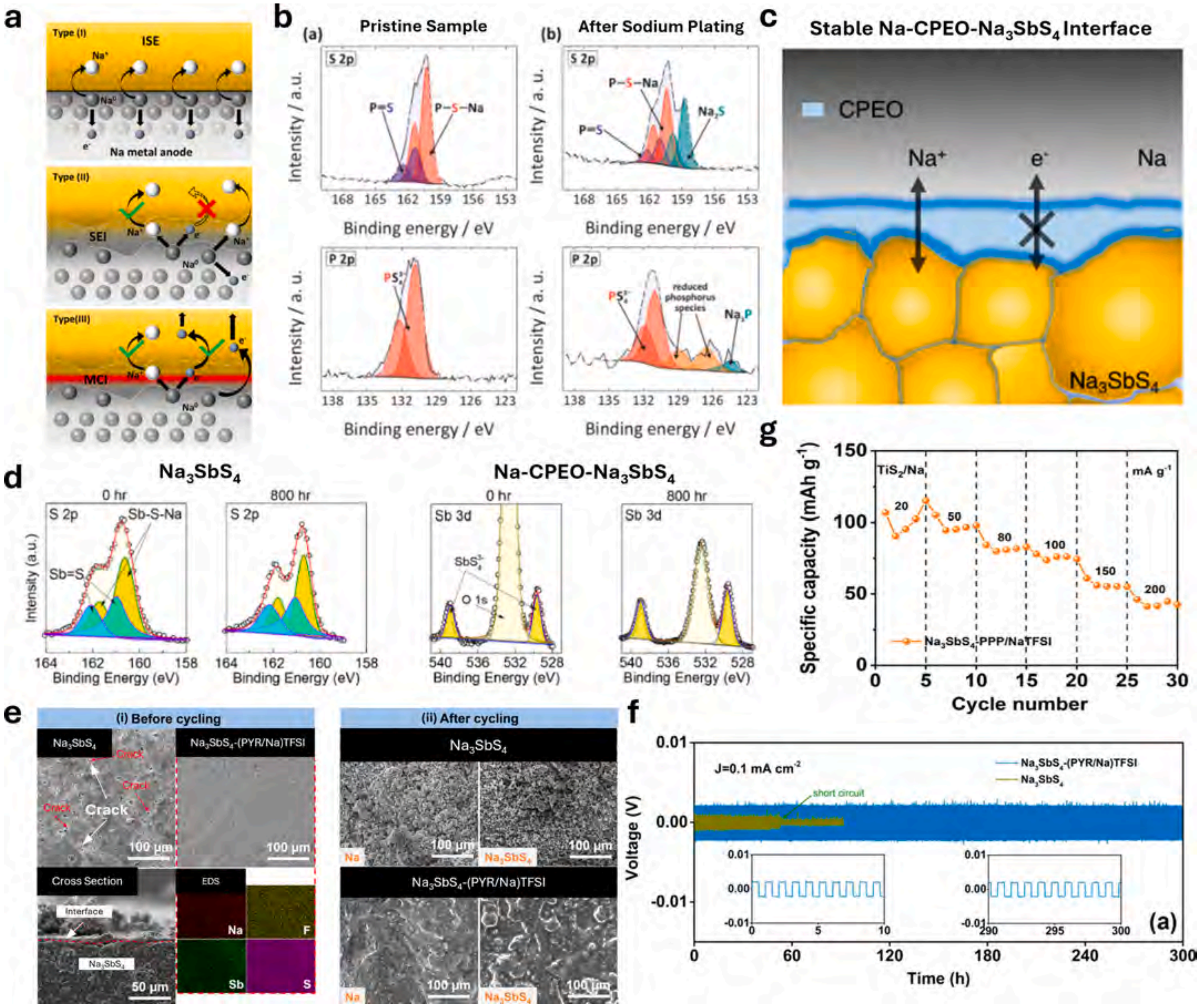

Fig. 20. (a) Diagram representing the three typical in-situ interface types resulting from the interaction of SSE with a Na metal anode: (i) thermodynamic stable interface; (ii) kinetically stable SEI layer; and (iii) unstable MCI layer. (b) S 2p and P 2p XPS spectra with matching fits of a Na_3PS_4 sample, before (a) and after (b) sodium metal plating. (c) Schematic of the formation of kinetically stable SEI layer by the addition of cellulose-poly (ethylene oxide) (CPEO) interlayer. (d) S 2p and P 2p XPS spectra for the Na_3SbS_4 pellet surface after the removal of the CPEO layer. The absence of Na_2S and Sb peaks at 800 hours indicates reduced Na_3SbS_4 decomposition. (e) SEM images before stripping/plating (i) for Na_3SbS_4 and ionic liquid interlayered Na_3SbS_4(PYR/Na)TFSI SSE. Cross section of Na_3SbS_4(PYR/Na) TFSI and EDS mapping are shown in bottom two SEM images, and after stripping/plating are indicated in (ii). (f) At a current density of 0.1 mA cm^{-2}, the galvanostatic cycling performance of the Na/Na_3SbS_4/Na and Na/Na_3SBS_4-(PYR/Na)TFSI/Na cell is shown, along with magnified voltage profiles. (g) The rate capabilities of the TiS_2/Na_3SbS_4-PPP|NaTFSI/Na batteries are assessed at 50 °C across varying current densities of 20, 50, 80, 100, 150, and 200 mA g^{-1}.

(a) Reproduced with permission from [119], copyright 2023, Royal Society of Chemistry. (b) Reproduced with permission from [280], copyright 2016, American Chemical Society. (c-d) Reproduced with permission from [283], copyright 2019, American Chemical Society. (e-f) Reproduced with permission from [284], copyright 2022, Elsevier. (g) Reproduced with permission from [285], copyright 2021, Wiley.

conductivity of 24.2 mS cm^{-1} with record lowest activation barrier of 0.088 eV as shown in Fig. 19c-d. Weak Na-S interactions and better Na ions correlated motion by higher Na-Na repulsions through excess Na doping are the key reasons behind this improvement. Due to enhancements observed in the conductivity and ion transport mechanisms by doping with +6 oxidation state transition metal elements, He *et al.* [274] synthesized a series of Molybdenum doped-Na_3SbS_4 via methods of ball milling and melt quenching. In addition, I^- was also introduced to help with poor interfacial stability with Na metal anode and enhance electrochemical performance. Currently, there has been no record of enhanced stripping/plating with W^{6+} doping alone. Melt quenching method has been deemed as most efficient in synthesizing $Na_{(3-2x)}Sb_{(1-x)}Mo_xS_{(4-x)}I_x$ (x = 0.05, 0.1, 0.15, 0.2) with excess S. No impurity of MoS_2 is observed even for 0.2 mol% of Mo-doping via melt quenching [275](Fig. 19e), while the other method indicated MoS_2 impurity at 0.2 mol% doping. From the XPS spectra of Mo 3d, the Mo $3d_{5/2}$ and Mo $3d_{3/2}$ peak at 225.43 eV, 228.83 eV and 231.78 eV indicate that Mo remains as Mo^{4+} instead of Mo^{6+}. This is likely due to higher thermal stability of MoS_2 than MoS_3. While the conductivity could not reach expected heights (0.54 mS cm^{-1}), the $Na_{2.9}Sb_{0.95}Mo_{0.05}S_{3.95}I_{0.05}$ SSE for all mol% generated no significant H_2S after air exposure (Fig. 19 f)

4.6. Electrochemical stability of sodium sulfide SSEs

While the developments in Na sulfide SSEs through various doping strategies have shown to be promising in respect to robust ionic conductivity, the enhancement in interfacial stability with Na metal anode remains a concern for the development of SSBs [276,277]. Sulfide SSEs are known to possesses narrow electrochemical voltage window, which in contact with very reactive Na metal anode generates mixed conducting interfaces that continuously deteriorates the SSE and increases the impedance of the cell [278,279]. While the sulfide-based SSEs do not show rigid behaviour in contrast to other oxides or NASICON SSEs, the issue of contact loss between the Na metal anode and sulfide SSE still exists upon cycling. With repeated cycling, the interface undergoes severe irreversible reactions that leads to generation of reactive interphases and even contact loss in few cases. To ensure both the thermodynamic and kinetic stability of the interface between electrolytes and metal anodes, three distinct types of interfaces are generally observed as shown in Fig. 20a. These include (I) an inherently stable interface with no reaction, (II) a reactive interface that forms a passivating solid electrolyte interphase (SEI) layer to prevent further reactions and allow kinetic stability, and (III) an unstable, mixed conducting interface (MCI) that facilitates the conduction of both ions and electrons. While the first option is ideal, achieving it is challenging, making the second a more practical solution for maintaining long-term interface stability [119]. The presence of a mixed ion-electronic conducting (MCI) interface, the third type, would result in continuous reactions between the Na metal and the solid-state electrolyte (SSE). This can lead to rapid capacity loss and increase the risk of a short circuit. From the XPS data of Na_3PS_4 by Wenzel et al. [280] (Fig. 20b), the S 2p and P 2p spectrums of before and after Na deposition in Na_3PS_4 SSE clearly show the formation of mixed conducting interphases like Na_2S (ionically conducting) and Na_3P (electronically and ionically conducting). The P-S-Na chemical state also shows significantly decreased intensity along with the PS_4^{3-} units of the SSE. These by-products lead to degradation of the Na SSE and continuous formation of Na dendrites upon reaction with the Na metal anode [280,281]. In the similar manner, Na_3SbS_4 SSE forms Na_2S and Na_3Sb products that impede the cell performance [282].

4.6.1. Artificial SEI interfaces to enhance electrochemical stability of SSEs

To combat this, stable artificial SEI interphases that are only ionically conducting are created such as done by Hu *et al.* [283] in which a polymer electrolyte cellulose-poly(ethylene oxide) (CPEO) interlayer can act as an effective stabilizer between the Na/Na_3SbS_4 interface by blocking every electronic pathway that could lead to SSE decomposition (Fig. 20c). The XPS spectra of the symmetric cell (Na/CPEO/-Na_3SbS_4/CPEO/Na) taken apart after stable 800 hr cycling at 0.1 mA cm^{-2} shows no traces of Na_2S and Sb as shown in Fig. 20d. Polyethylene oxide interlayer applied on the Na_3PS_4 surface has also shown to prevent the side reactions at the interface and deliver improving cycling performance with SnS_2/Na electrodes [286]. Using similar strategy, Li *et al.* [284] used an ionic liquid interlayer made from (PYR/Na)TFSI, which they applied on the side of SSE pellet in contact with the Na metal anode. This interlayer helped in reducing the interfacial resistance by improving the wettability and contact at the Na metal interface. Stable SEI formation was shown that showed stable Na stripping/plating for 300 hr at 0.1 mA cm^{-2} (Fig. 20 f). The before and after cycling SEM images of the Na_3SbS_4 SSE indicates rough surface with cracks during synthesis, which upon cycling leads to aggravated cracks and undesirable side products. Whereas the morphologies of interlayered-Na_3SbS_4 remain uniform and smooth (Fig. 20e). In another work by the same group, Li *et al.* [285] employed a phase-transition polymer electrolyte interlayer (PPP/NaTFSI) that could suppress the dendritic growth and prevent detrimental side reactions. Their full cell with TiS_2 cathode could cycle for 300 cycles at 20 mA g^{-1} rate and maintained a specific capacity of 100 mAh g^{-1}. Stable rate performance of this SSE is shown in the Fig. 20 g.

4.6.2. Effects of dopants on the electrochemical stability of SSEs

Introducing dopants into SSEs is a well-established technique for enhancing their properties. Among these methods, halogen doping has been frequently explored to mitigate side reactions that lead to cell failure. Cl-doped Na_3PS_4 forms NaCl at the interface that eases the uniform stripping/plating behaviour of Na ions [282]. Similarly, formation of NaBr at the interface is beneficial for Na ions conduction as it prevents the formation of Na dendrites and stops side reactions [287]. Apart from conventional dopants, Lazar *et al.* [288] tested doping O to form Na_3PS_3O. Without O, the Na/Na_3PS_4 interface has found to be very exfoliated, i.e., continuous reaction between the side products and Na metal takes place until the limiting reactant is fully consumed. Presence of O causes denser and less porous SSE surface that slows down the reaction between the Na/Na_3PS_3O and remains unreacted for longer periods. The optical photograph (Fig. 21a) displays the reaction products formed upon pressing the Na metal at 40 MPa on the surface of Na_3PS_4, $Na_3PS_{1.5}O_{2.5}$ and Na_3PS_3O SSE. For the former, a clear and separable layer of Na_3P is produced on the surface of SSE, while no significant reaction product could be observed for Na_3PS_3O SSE. The $Na_3PS_{1.5}O_{2.5}$ shows mild evolution of Na_3P after two weeks. In a similar approach, Chi *et al.* [289] synthesized $Na_3PS_{4-x}O_x$ (x = 0–0.6). At 60°C, $Na_3PS_{3.85}O_{0.15}$ exhibited the maximum ionic conductivity (0.27 mS cm^{-1}), whereas $Na_3PS_{3.4}O_{0.6}$ had lower conductivity (0.082 mS cm^{-1}) but greater electrochemical stability. A combination of these characteristics was achieved by a tri-layer SSE of $Na_3PS_{3.4}O_{0.6}$/$Na_3PS_{3.85}O_{0.15}$/$Na_3PS_{3.4}O_{0.6}$, which led to a stable cycling for 300 hours at 0.5 mA cm^{-2} without dendrites. The critical current density (CCD) test (current density increment of 0.05 mA cm^{-2} and cycle time of 1 hr for this tri-layer SSE is shown in the Fig. 21b. Highest CCD of 2.3 mA cm^{-2} can be achieved, which is comparable to the Li based systems. The full cell with Na-S cathode displays stable cycling even for increasing current densities as shown in the Fig. 21c. The cell could deliver near 900 mAh g^{-1} after 150 cycles at 0.10 mA cm^{-2} current density in a 60 °C environment. Most of the strategic modifications to enhance the interfacial stability does not necessarily also improve the ionic conductivity to enable higher rates cycling. So far, W-doped Na_3MS_4 (M = P, Sb) systems have reported the highest conductivity and look promising parent structures for further modification. However, W-doped SSEs induce significant deterioration of the interface and lead to cell failure. In an effort to stabilize the interface between Na/W-doped SSE, Weng *et al.* [290] synthesized a WO-doped version of the Na_3SbS_4 after promising results of O doping in previous literatures. Following the same trend, the $Na_{2.95}Sb_{0.95}W_{0.05}S_4$

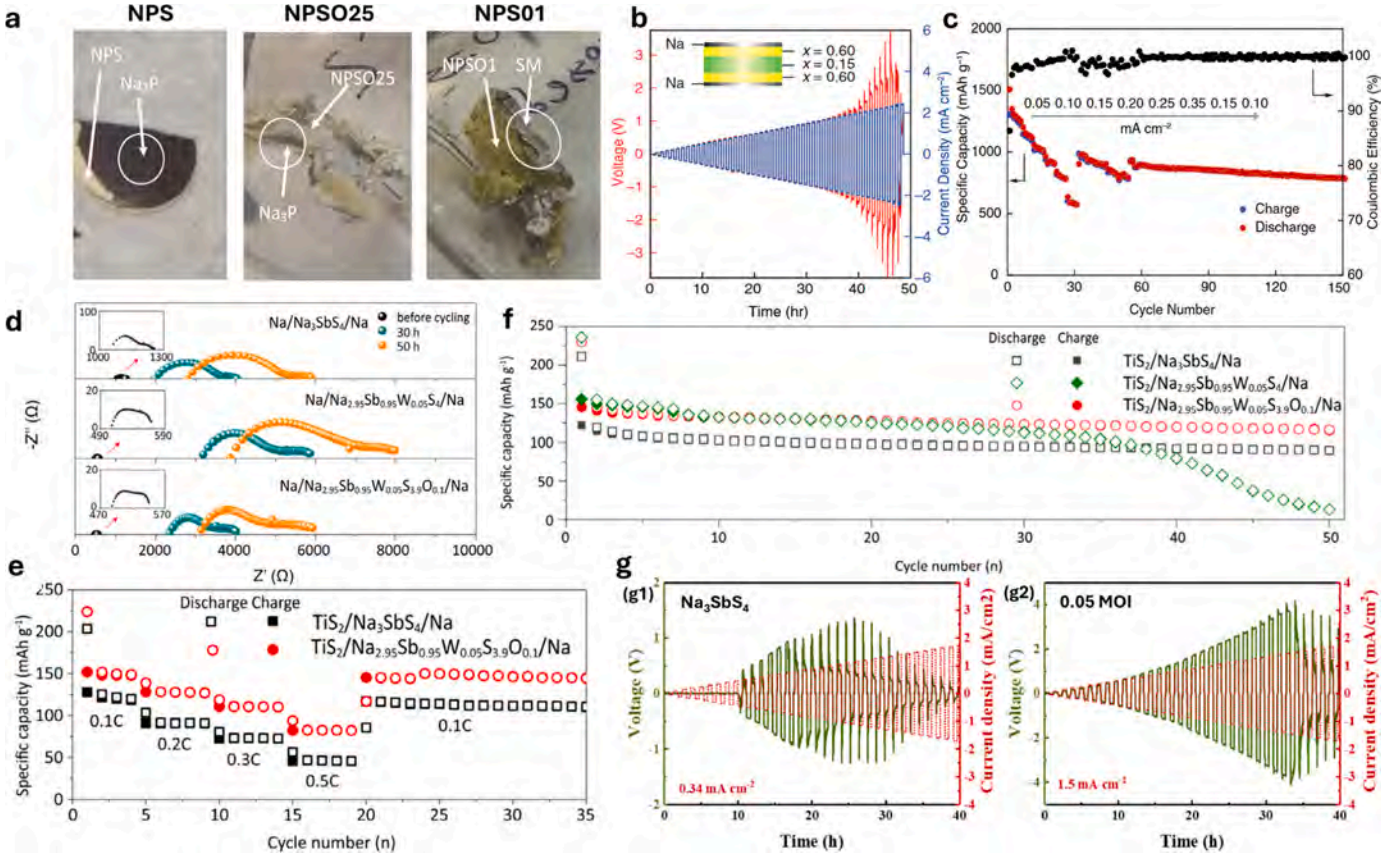

Fig. 21. (a) Optical microscope images of the reaction products produced upon pressing Na metal at 40 MPa against NPS, NPSO25, and NPSO1 pellets. (b) CCD test of the tri-layer solid electrolyte ($Na_3PS_{3.4}O_{0.6}/Na_3PS_{3.85}O_{0.15}/Na_3PS_{3.4}O_{0.6}$) conducted at 60 °C. Current density increments are of 0.05 mA cm^{-2}, each plating/stripping cycle lasts 30 minutes. (c) Rate performance of a Na-S/$Na_3PS_{3.85}O_{0.15}/Na_3PS_{3.4}O_{0.6}$/Na full cell at varying current densities at 60 °C. (d) AC impedance of the WO-doped symmetric cells before and after 30 h, 50 h cycling. (e) Rate performances of TiS_2/Na_3SbS_4/Na and $TiS_2/Na_{2.95}Sb_{0.95}W_{0.05}S_{3.9}O_{0.1}$/Na full cells. (f) Cycling performance of TiS_2/Na_3SbS_4/Na, $TiS_2/Na_{2.95}Sb_{0.95}W_{0.05}S_4$/Na, and $TiS_2/Na_{2.95}Sb_{0.95}W_{0.05}S_{3.9}O_{0.1}$/Na full cells at 0.1 C (1 C = 240 mAg^{-1}) in the voltage range of 1.0–2.5 V at RT 25°C. (g) CCD testing for Na/SSE/Na symmetric cells with (g1) Na_3SbS_4 and (g2) $Na_{2.9}Sb_{0.95}Mo_{0.05}S_{3.95}I_{0.05}$ SSE. Each cycle lasts for 1 hour and the current increments are 0.05 mA cm^{-2} per cycle.

(a) Reproduced with permission from [288], copyright 2020, American Chemical Society. (b-c) Reproduced with permission from [289], copyright 2022, Nature. (d-f) Reproduced with permission from [290], copyright 2022, Elsevier. (g) Reproduced with permission from [274], copyright 2024, Elsevier.

and $Na_{2.95}Sb_{0.95}W_{0.05}S_{3.9}O_{0.1}$ SSEs show a high conductivity of 10.37 and 8.49 mS cm^{-1}, respectively. Na/SSE/Na stripping plating results indicate slower increase in the polarization voltage with WO-doped SSE. From the EIS profiles (Fig. 21d) for before cycling and after 30 h, 50 h cycling, the WO-doped SSE shows lowest R_b before cycling and the increase in impedance is slower with cycling as compared to W-doped SSE. While the pristine Na_3SbS_4 shows smaller increase in impedance, it lacks by an order of magnitude in ionic conductivity, which is also a critical factor under consideration. In the full cell configuration with TiS_2/Na metal electrodes, the WO-doped SSE shows improved long-term cycling and higher specific capacity for different C-rates (Fig. 21e-f). While He *et al.* [274] could not achieve heightened conductivity with MoI doping in $Na_{2.9}Sb_{0.95}Mo_{0.05}S_{3.95}I_{0.05}$, they demonstrated higher critical current density of 1.5 mA cm^{-2} in contrast to 0.34 mA cm^{-2} of Na_3SbS_4. Stripping/plating for Na/0.05 MoI/Na could be made efficient and prolonged with I doping except for continuous increase in polarization in contrast to undoped version (Fig. 21 g).

5. Conclusion and perspective

This review comprehensively summarizes the structural engineering strategies used to improve ionic conductivity and electrochemical stability in lithium and sodium sulfide SSEs, by correlating their synthesis methods with structural features and diffusion mechanisms. The successful strategies are outlined in Table 3 (lithium) and Table 4 (sodium), including their respective ionic conductivities and electrochemical stability windows. Among these substituted argyrodite SSEs, some materials exhibit conductivities comparable to liquid electrolytes. The main strategies for developing SSEs with high ionic conductivity are summarized in Fig. 22. These techniques include manipulating the halogen content to induce anion disorder, creating vacancies, promoting concerted migration through excess lithiation or sodiation, increasing lattice polarizability through chalcogenide substitution, and expanding the lattice via phosphorus substitution.

In lithium argyrodites, the presence of multiple halogen atoms softens the anion sublattice and creates site disorder between S^{2-} and X^- ions. This softening effect lowers the activation energy by weakening bonds and expanding the unit cell, thereby enhancing ionic mobility and enabling diffusion at lower temperatures. Furthermore, excessive halogenation introduces mobile ion vacancies to maintain charge neutrality, which also enhances polarizability and reduces the energy barrier for ion transport. These vacancies shorten the inter-cage jump distances, facilitating concerted ion migration by lowering the energy barriers for ionic diffusion. Another effective approach involves doping on the phosphorus site with larger ions, which expands the unit cell and particularly widens ion migration bottlenecks, crucial for enabling low-energy migration pathways.

In contrast to lithium sulfide-based SSEs, structural engineering for sodium sulfide SSEs is less explored. This review highlights Na_3PS_4 and its derivatives as examples to examine existing structural engineering

Table 4
Summary of structural engineering strategies to sodium sulfide solid state electrolytes.

Substitution Sites	**Composition**	**Ionic Conductivity (RT)**	**Voltage *vs* Sodium**
Sodium Vacancy	t-Na_3PS_4 [111]	0.0001 mS cm^{-1}	1.39 V – 2.45 V
	c-Na_3PS_4 [227]	0.2 mS cm^{-1}	1.39 V – 2.45 V
	c-$Na_{2.73}Ca_{0.135}PS_4$ [241]	0.94 mS cm^{-1}	0.70 V – 4.00 V
	t-$Na_{47}P_{16}S_{16}Cl$ [239]	1.07 mS cm^{-1}	-
	t-$Na_{2.9375}PS_{3.9375}Cl_{0.0625}$ [238]	1.14 mS cm^{-1}	< 2.40 V
	t-$Na_{47}P_{16}S_{63}Br$ [239]	2.37 mS cm^{-1}	-
	t-$Na_{46}P_{16}S_{62}Br_2$ [239]	5.60 mS cm^{-1}	-
Chalcogenide	c-Na_3PSe_4 [121]	0.11 mS cm^{-1}	-
	c-Na_3SbSe_4 [245]	3.70 mS cm^{-1}	-
Phosphorus	c−$94Na_3PS_{4}.{}_6Na_4SiS_4$ [247]	0.74 mS cm^{-1}	-
	$Na_3P_{0.62}As_{0.38}S_4$ [266]	1.46 mS cm^{-1}	0.0 V – 5.0 V
	t-Na_3SbS_4 [262]	3.00 mS cm^{-1}	< 5.00 V
	$Na_{3.1}Sb_{0.9}Ge_{0.1}S_4$ [269]	5.00 mS cm^{-1}	-
	c-$Na_{2.85}P_{0.85}W_{0.15}S_4$ (SC) [254]	8.8 mS cm^{-1}	-
	c-$Na_{2.9}P_{0.9}W_{0.1}S_4$ [253]	13.0 mS cm^{-1}	-
	c-$Na_{2.85}P_{0.85}W_{0.15}S_4$ [254]	13.7 mS cm^{-1}	-
	c-$Na_{2.88}Sb_{0.88}W_{0.12}S_4$ [260]	32.0 mS cm^{-1}	-

strategies. As shown in Table 4, the summary of sodium sulfide-based SSEs is less extensive than that of lithium-based systems. However, the introduction of vacancies in Na_3PS_4-based structures has been well-documented, proving effective in improving conductivity. Vacancies can be introduced by doping higher-valence cations, such as Ca^{2+} or Al^{3+}, at the mobile ion sites. This progressively shrinks the unit cell, reducing ion jump distances and leading to enhanced ionic conductivity. Additionally, substituting sulfur with larger chalcogenide ions like Se^{2-} or Te^{2-} expands the unit cell, increasing polarizability and softening the lattice, which lowers the energy barrier for ion migration and provides an alternative pathway for improved ion transport. Both strategies—unit cell shrinkage through cation doping and unit cell expansion via anion substitution—offer distinct advantages. Shrinking the unit cell enhances kinetics by shortening jump distances, while expanding the unit cell increases ion mobility by creating a more flexible and less rigid structure. The choice between these approaches depends on the specific design goals of the electrolytes, and it is essential to view them not as conflicting, but as complementary strategies for improving SSEs performance.

Another challenge in developing sulfide SSEs is to maintain a low elastic modulus while retaining high conductivity and stability. Ideally, SSEs should be developed for both Li and Na, possessing high conductivity values and low elastic modulus to accommodate dynamic changes such as volumetric expansion, flexibility, and breakdown of electrode materials. A potential solution to this issue from computational studies is to develop fully halogenated SSEs, which would result in softer lattices. This strategy has been proven by recent work, demonstrating higher conductivity values with the lowest elastic modulus ($Li_{5.2}Si_{0.2}Sb_{0.8}S_4$-$Br_{0.25}I_{1.75}$ - 13.23 mS cm^{-1}) [220]. While these fully halogenated SSEs show promise, their overall electrochemical robustness still requires significant improvement for practical use. More attention needs to be given to the electrochemical stability window of sulfide SSEs. Without a sufficiently wide electrochemical stability window, Li argyrodites cannot be directly used in all-solid-state lithium-ion batteries. While a few studies have reported oxidative-resistant argyrodites that can withstand high-voltage cathodes, very few address reduction stability against lithium metal anodes. Surface modification and interface

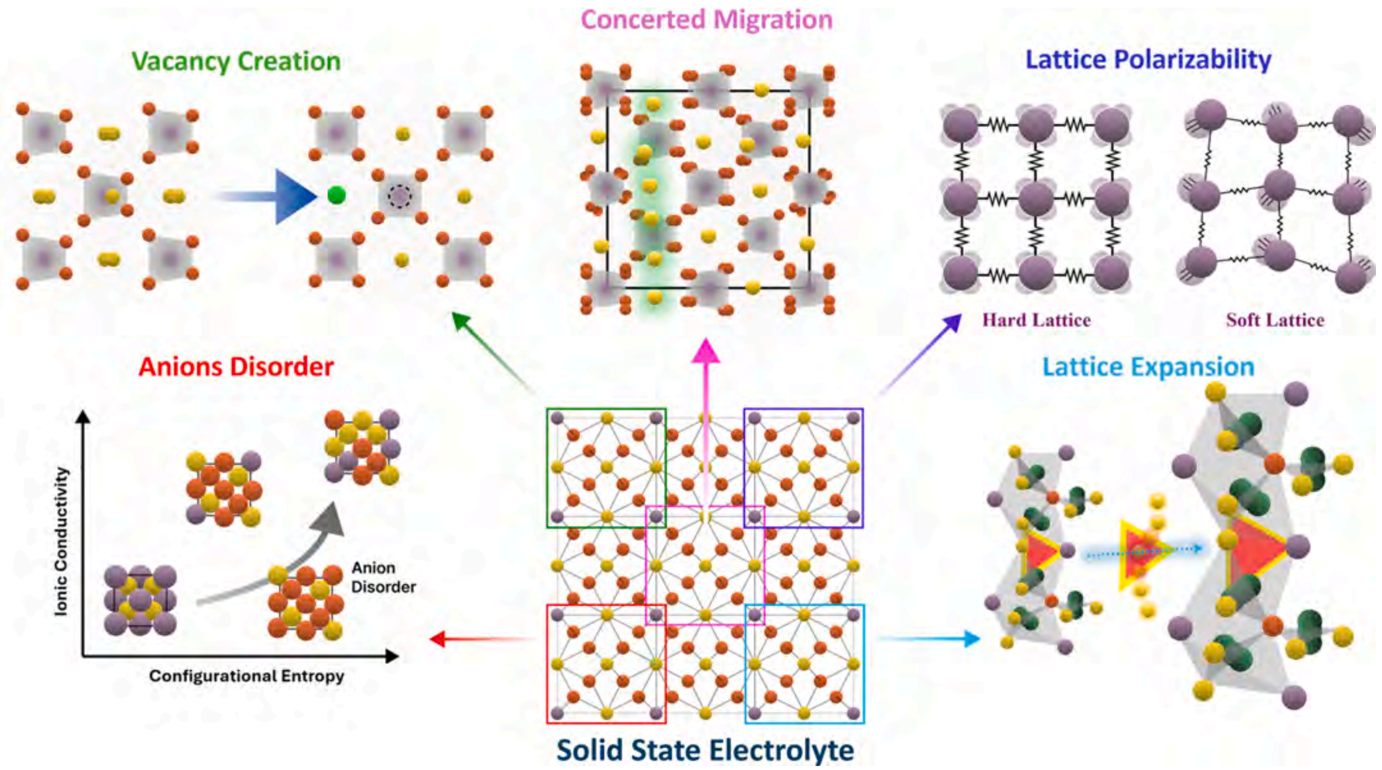

Fig. 22. Schematic summarizing key structural modification techniques applied to lithium and sodium sulfide SSEs, including anion disorder, vacancy creation, concerted ion migration, enhanced lattice polarizability, and lattice expansion. These modifications are aimed at optimizing ion transport and improving overall electrolyte performance.

engineering should therefore be prioritized alongside the development of new materials with wider electrochemical stability windows. As summarized in Table 4, only a few sodium-based SSEs are stable against both the Na anode and the cathode. Current research into Na-based SSEs is focused on developing new sulfide materials with improved electrochemical and air stability. Additionally, dual-SSE systems (using two types of SSEs) have been explored to address the narrow electrochemical stability windows in sodium-based batteries. Ultimately, improving electrochemical stability and moisture, high-performance SSEs that are suitable for commercial battery applications.

CRediT authorship contribution statement

Zhiming Liang: Writing – original draft, Investigation, Funding acquisition, Formal analysis, Conceptualization. **Sehee Lee:** Writing – review & editing, Supervision, Resources. **Chunmei Ban:** Writing – review & editing, Supervision, Investigation, Conceptualization. **Mohammad Nafis:** Writing – original draft, Investigation, Funding acquisition, Formal analysis, Conceptualization.

Declaration of Competing Interest

The authors declare the following financial interests/personal relationships which may be considered as potential competing interests: Chunmei Ban reports financial support was provided by National Science Foundation. If there are other authors, they declare that they have no known competing financial interests or personal relationships that could have appeared to influence the work reported in this paper.

Acknowledgements

Z.L., M.S.N., S.L., thank the funding from the University of Colorado Boulder. C.B. thanks the support from the National Science Foundation under Grant No. 2323065. Any opinions, findings, and conclusions or recommendations expressed in this material are those of the author(s) and do not necessarily reflect the views of the National Science Foundation. We acknowledge Rifaa Javed from the Polytechnic University of Milan for his assistance in designing Fig. 22.

Data availability

Data will be made available on request.

References

[1] Z. Liang, T. Li, H. Chi, J. Ziegelbauer, K. Sun, M. Wang, W. Zhang, T. Liu, Y.-T. Cheng, Z. Chen, X. Gayden, C. Ban, Solvent-free manufacturing of lithium-ion battery electrodes via cold plasma, ENERGY Environ. Mater. 7 (2024) e12503, https://doi.org/10.1002/eem2.12503.

[2] M. Armand, J.-M. Tarascon, Building better batteries, Nature 451 (2008) 652–657, https://doi.org/10.1038/451652a.

[3] W. Li, J.R. Dahn, D.S. Wainwright, Rechargeable lithium batteries with aqueous electrolytes, Science 264 (1994) 1115–1118, https://doi.org/10.1126/science.264.5162.1115.

[4] Y. Nishi, Lithium ion secondary batteries; past 10 years and the future, J. Power Sources 100 (2001) 101–106, https://doi.org/10.1016/S0378-7753(01)00887-4.

[5] Z. Liang, M.S. Nafis, D. Rodriguez, C. Ban, Surface science and engineering for electrochemical materials, Acc. Chem. Res. (2024), https://doi.org/10.1021/acs.accounts.4c00433.

[6] Z. Liang, Y. Wang, B. Pei, S.-B. Son, M. Nguyen, N.R. Singstock, S. Huang, M. Mo, J. Li, M.S. Whittingham, C. Ban, 3D-integrated, multi-functional carbon fibers for stable, high-areal-capacity batteries, Adv. Energy Mater. 13 (2023) 2301295, https://doi.org/10.1002/aenm.202301295.

[7] S. Shrestha, J. Kim, J. Jeong, H.J. Lee, S.C. Kim, H.J. Hah, K. Oh, S.-H. Lee, Effect of amorphous LiPON coating on electrochemical performance of LiNi0. 8Mn0. 1Co0. 1O2 (NMC811) in all solid-state batteries, J. Electrochem. Soc. 168 (2021) 060537.

[8] S. Shrestha, C. Carpenter, J. Kim, J. Jeong, H.J. Lee, S.C. Kim, H.J. Hah, M.-S. Song, K. Oh, S.-H. Lee, Effect of polyacrylonitrile surface coating on electrochemical performance of LiNi0. 8Mn0. 1Co0. 1O2 in all solid-state batteries, J. Electrochem. Soc. 169 (2022) 060541.

[9] J. Jeong, K. Lee, C. Carpenter, S. Shrestha, J. Kim, H.-S. Chung, J. Moon, K.H. Oh, J.-Y. Sun, S.-H. Lee, Improved cycle properties of all-solid-state Li-ion batteries with Al2O3 coating on the silicon-based anode, J. Energy Eng. 150 (2024) 04024003, https://doi.org/10.1061/JLEED9.EYENG-5168.

[10] F. Zheng, M. Kotobuki, S. Song, M.O. Lai, L. Lu, Review on solid electrolytes for all-solid-state lithium-ion batteries, J. Power Sources 389 (2018) 198–213, https://doi.org/10.1016/j.jpowsour.2018.04.022.

[11] Z. Jiang, J. Yang, C. Liu, C. Wei, Z. Wu, Q. Luo, L. Zhang, X. Chen, L. Li, G. Li, S. Cheng, C. Yu, Insights on Bi-O dual-doped Li5.5PS4.5Cl1.5 electrolyte with enhanced electrochemical properties for all-solid-state lithium metal batteries, Nano Energy 128 (2024) 109926, https://doi.org/10.1016/j.nanoen.2024.109926.

[12] K. Takada, Progress and prospective of solid-state lithium batteries, Acta Mater. 61 (2013) 759–770, https://doi.org/10.1016/j.actamat.2012.10.034.

[13] J.C. Bachman, S. Muy, A. Grimaud, H.-H. Chang, N. Pour, S.F. Lux, O. Paschos, F. Maglia, S. Lupart, P. Lamp, L. Giordano, Y. Shao-Horn, Inorganic solid-state electrolytes for lithium batteries: mechanisms and properties governing ion conduction, Chem. Rev. 116 (2016) 140–162, https://doi.org/10.1021/acs.chemrev.5b00563.

[14] B.A. Boukamp, R.A. Huggins, Lithium ion conductivity in lithium nitride, Phys. Lett. A 58 (1976) 231–233, https://doi.org/10.1016/0375-9601(76)90082-7.

[15] Y. Zhao, L.L. Daemen, Superionic conductivity in lithium-rich anti-perovskites, J. Am. Chem. Soc. 134 (2012) 15042–15047, https://doi.org/10.1021/ja305709z.

[16] Y. Wang, S. Song, C. Xu, N. Hu, J. Molenda, L. Lu, Development of solid-state electrolytes for sodium-ion battery–A short review, Nano Mater. Sci. 1 (2019) 91–100, https://doi.org/10.1016/j.nanoms.2019.02.007.

[17] G.E. Youngblood, G.R. Miller, R.S. Gordon, Relative effects of phase conversion and grain size on sodium ion conduction in polycrystalline, lithia-stabilized β-alumina, J. Am. Ceram. Soc. 61 (1978) 86–87, https://doi.org/10.1111/j.1151-2916.1978.tb09238.x.

[18] X. Lu, G. Xia, J.P. Lemmon, Z. Yang, Advanced materials for sodium-beta alumina batteries: Status, challenges and perspectives, J. Power Sources 195 (2010) 2431–2442, https://doi.org/10.1016/j.jpowsour.2009.11.120.

[19] J. Lu, Y. Li, Y. Kong, N. Zhang, Study of structure and conductivity of Li3/8Sr7/16-3x/2LaxZr1/4Nb3/4O3 solid electrolytes, Ceram. Int. 44 (2018) 4744–4750, https://doi.org/10.1016/j.ceramint.2017.12.058.

[20] D. Mazumdar, D.N. Bose, M.L. Mukherjee, Transport and dielectric properties of lisicon, Solid State Ion.-. 14 (1984) 143–147, https://doi.org/10.1016/0167-2738(84)90089-4.

[21] J. Kuwano, A.R. West, New Li+ ion conductors in the system, Li4GeO4-Li3VO4, Mater. Res. Bull. 15 (1980) 1661–1667, https://doi.org/10.1016/0025-5408(80)90249-4.

[22] S. Song, J. Lu, F. Zheng, H.M. Duong, L. Lu, A facile strategy to achieve high conduction and excellent chemical stability of lithium solid electrolytes, RSC Adv. 5 (2014) 6588–6594, https://doi.org/10.1039/C4RA11287C.

[23] H.Y.-P. Hong, Crystal structure and ionic conductivity of Li14Zn(GeO4)4 and other new Li+ superionic conductors, Mater. Res. Bull. 13 (1978) 117–124, https://doi.org/10.1016/0025-5408(78)90075-2.

[24] Y. Inaguma, C. Liquan, M. Itoh, T. Nakamura, T. Uchida, H. Ikuta, M. Wakihara, High ionic conductivity in lithium lanthanum titanate, Solid State Commun. 86 (1993) 689–693, https://doi.org/10.1016/0038-1098(93)90841-A.

[25] S. Stramare, V. Thangadurai, W. Weppner, Lithium Lanthanum Titanates: A Review, Chem. Mater. 15 (2003) 3974–3990, https://doi.org/10.1021/cm0300516.

[26] Y. Inaguma, L. Chen, M. Itoh, T. Nakamura, Candidate compounds with perovskite structure for high lithium ionic conductivity, Solid State Ion.-. 70–71 (1994) 196–202, https://doi.org/10.1016/0167-2738(94)90309-3.

[27] H.-T. Chung, J.-G. Kim, H.-G. Kim, Dependence of the lithium ionic conductivity on the B-site ion substitution in (Li0.5La0.5)Ti1−xMxO3 (M=Sn, Zr, Mn, Ge), Solid State Ion.-. 107 (1998) 153–160, https://doi.org/10.1016/S0167-2738(97)00525-0.

[28] R. Inada, K. Kimura, K. Kusakabe, T. Tojo, Y. Sakurai, Synthesis and lithium-ion conductivity for perovskite-type Li3/8Sr7/16Ta3/4Zr1/4O3 solid electrolyte by powder-bed sintering, Solid State Ion.-. 261 (2014) 95–99, https://doi.org/10.1016/j.ssi.2014.04.005.

[29] K. Kimura, K. Wagatsuma, T. Tojo, R. Inada, Y. Sakurai, Effect of composition on lithium-ion conductivity for perovskite-type lithium–strontium–tantalum–zirconium-oxide solid electrolytes, Ceram. Int. 42 (2016) 5546–5552, https://doi.org/10.1016/j.ceramint.2015.12.133.

[30] R. Yu, Q.-X. Du, B.-K. Zou, Z.-Y. Wen, C.-H. Chen, Synthesis and characterization of perovskite-type (Li,Sr)(Zr,Nb)O3 quaternary solid electrolyte for all-solid-state batteries, J. Power Sources 306 (2016) 623–629, https://doi.org/10.1016/j.jpowsour.2015.12.065.

[31] J.B. Bates, N.J. Dudney, G.R. Gruzalski, R.A. Zuhr, A. Choudhury, C.F. Luck, J. D. Robertson, Fabrication and characterization of amorphous lithium electrolyte thin films and rechargeable thin-film batteries, J. Power Sources 43 (1993) 103–110, https://doi.org/10.1016/0378-7753(93)80106-Y.

[32] Y. Su, J. Falgenhauer, A. Polity, T. Leichtweiß, A. Kronenberger, J. Obel, S. Zhou, D. Schlettwein, J. Janek, B.K. Meyer, LiPON thin films with high nitrogen content for application in lithium batteries and electrochromic devices prepared by RF magnetron sputtering, Solid State Ion.-. 282 (2015) 63–69, https://doi.org/10.1016/j.ssi.2015.09.022.

[33] T. Fujibayashi, Y. Kubota, K. Iwabuchi, N. Yoshii, Highly conformal and high-ionic conductivity thin-film electrolyte for 3D-structured micro batteries:

Characterization of LiPON film deposited by MOCVD method, AIP Adv. 7 (2017) 085110, https://doi.org/10.1063/1.4999915.

[34] L. Le Van-Jodin, A. Claudel, C. Secouard, F. Sabary, J.-P. Barnes, S. Martin, Role of the chemical composition and structure on the electrical properties of a solid state electrolyte: Case of a highly conductive LiPON, Electrochim. Acta 259 (2018) 742–751, https://doi.org/10.1016/j.electacta.2017.11.021.

[35] X. Xu, Z. Wen, X. Wu, X. Yang, Z. Gu, Lithium Ion-Conducting Glass–Ceramics of Li1.5Al0.5Ge1.5(PO4)3–xLi2O (x=0.0–0.20) with Good Electrical and Electrochemical Properties, J. Am. Ceram. Soc. 90 (2007) 2802–2806, https://doi.org/10.1111/j.1551-2916.2007.01827.x.

[36] J. Thokchom, N. Gupta, B. Kumar, Superionic Conductivity in a Lithium Aluminum Germanium Phosphate Glass–Ceramic, J. Electrochem. Soc. - J. Electrochem. Soc. 155 (2008), https://doi.org/10.1149/1.2988731.

[37] R. Murugan, V. Thangadurai, W. Weppner, Fast Lithium Ion Conduction in Garnet-Type Li7La3Zr2O12, Angew. Chem. Int. Ed. 46 (2007) 7778–7781, https://doi.org/10.1002/anie.200701144.

[38] S. Ohta, T. Kobayashi, T. Asaoka, High lithium ionic conductivity in the garnet-type oxide Li7−X La3(Zr2−X, NbX)O12 (X=0–2), J. Power Sources 196 (2011) 3342–3345, https://doi.org/10.1016/j.jpowsour.2010.11.089.

[39] R. Murugan, S. Ramakumar, N. Janani, High conductive yttrium doped Li7La3Zr2O12 cubic lithium garnet, Electrochem. Commun. 13 (2011) 1373–1375, https://doi.org/10.1016/j.elecom.2011.08.014.

[40] L. Buannic, B. Orayech, J.-M. López Del Amo, J. Carrasco, N.A. Katcho, F. Aguesse, W. Manalastas, W. Zhang, J. Kilner, A. Llordés, Dual Substitution Strategy to Enhance Li+ Ionic Conductivity in Li7La3Zr2O12 Solid Electrolyte, Chem. Mater. 29 (2017) 1769–1778, https://doi.org/10.1021/acs.chemmater.6b05369.

[41] J.-F. Wu, W.K. Pang, V.K. Peterson, L. Wei, X. Guo, Garnet-Type Fast Li-Ion Conductors with High Ionic Conductivities for All-Solid-State Batteries, ACS Appl. Mater. Interfaces 9 (2017) 12461–12468, https://doi.org/10.1021/acsami.7b00614.

[42] G. Larraz, A. Orera, M.L. Sanjuán, Cubic phases of garnet-type Li7La3Zr2O12: the role of hydration, J. Mater. Chem. A 1 (2013) 11419–11428, https://doi.org/10.1039/C3TA11996C.

[43] S. Liu, N. Imanishi, T. Zhang, A. Hirano, Y. Takeda, O. Yamamoto, J. Yang, Effect of nano-silica filler in polymer electrolyte on Li dendrite formation in Li/poly(ethylene oxide)–Li(CF3SO2)2N/Li, J. Power Sources 195 (2010) 6847–6853, https://doi.org/10.1016/j.jpowsour.2010.04.027.

[44] C.W. Lin, C.L. Hung, M. Venkateswarlu, B.J. Hwang, Influence of TiO2 nano-particles on the transport properties of composite polymer electrolyte for lithium-ion batteries, J. Power Sources 146 (2005) 397–401, https://doi.org/10.1016/j.jpowsour.2005.03.028.

[45] C. Yuan, J. Li, P. Han, Y. Lai, Z. Zhang, J. Liu, Enhanced electrochemical performance of poly(ethylene oxide) based composite polymer electrolyte by incorporation of nano-sized metal-organic framework, J. Power Sources 240 (2013) 653–658, https://doi.org/10.1016/j.jpowsour.2013.05.030.

[46] Y. An, X. Han, Y. Liu, A. Azhar, J. Na, A.K. Nanjundan, S. Wang, J. Yu, Y. Yamauchi, Progress in Solid Polymer Electrolytes for Lithium-Ion Batteries and Beyond, Small Weinh. Bergstr. Ger. 18 (2022) e2103617, https://doi.org/10.1002/smll.202103617.

[47] K.-H. Park, K. Kaup, A. Assoud, Q. Zhang, X. Wu, L.F. Nazar, High-Voltage Superionic Halide Solid Electrolytes for All-Solid-State Li-Ion Batteries, ACS Energy Lett. 5 (2020) 533–539, https://doi.org/10.1021/acsenergylett.9b02599.

[48] M. Zheng, X. Li, J. Sun, X. Wang, G. Liu, W. Yu, X. Dong, J. Wang, Research progress on chloride solid electrolytes for all-solid-state batteries, J. Power Sources 595 (2024) 234051, https://doi.org/10.1016/j.jpowsour.2024.234051.

[49] S. Wang, Q. Bai, A.M. Nolan, Y. Liu, S. Gong, Q. Sun, Y. Mo, Lithium Chlorides and Bromides as Promising Solid-State Chemistries for Fast Ion Conductors with Good Electrochemical Stability, Angew. Chem. Int. Ed. 58 (2019) 8039–8043, https://doi.org/10.1002/anie.201901938.

[50] R. Schlem, T. Bernges, C. Li, M.A. Kraft, N. Minafra, W.G. Zeier, Lattice Dynamical Approach for Finding the Lithium Superionic Conductor Li3ErI6, ACS Appl. Energy Mater. 3 (2020) 3684–3691, https://doi.org/10.1021/acsaem.0c00147.

[51] J.B. Goodenough, P. Singh, Review—Solid Electrolytes in Rechargeable Electrochemical Cells, J. Electrochem. Soc. 162 (2015) A2387, https://doi.org/10.1149/2.0021514jes.

[52] W. Zhou, Y. Li, S. Xin, J.B. Goodenough, Rechargeable Sodium All-Solid-State Battery, ACS Cent. Sci. 3 (2017) 52–57, https://doi.org/10.1021/acscentsci.6b00321.

[53] Z. Jiang, B. Carroll, K.M. Abraham, Studies of some poly(vinylidene fluoride) electrolytes, Electrochim. Acta 42 (1997) 2667–2677, https://doi.org/10.1016/S0013-4686(97)00005-4.

[54] D. Kumar, Mohd Suleman, S.A. Hashmi, Studies on poly(vinylidene fluoride-co-hexafluoropropylene) based gel electrolyte nanocomposite for sodium–sulfur batteries, Solid State Ion.-. 202 (2011) 45–53, https://doi.org/10.1016/j.ssi.2011.09.001.

[55] J.-K. Kim, Y.J. Lim, H. Kim, G.-B. Cho, Y. Kim, A hybrid solid electrolyte for flexible solid-state sodium batteries, Energy Environ. Sci. 8 (2015) 3589–3596, https://doi.org/10.1039/C5EE01941A.

[56] K.B.M. Isa, L. Othman, D. Hambali, Z. Osman, Electrical and electrochemical studies on sodium ion-based gel polymer electrolytes, AIP Conf. Proc. 1877 (2017) 040001, https://doi.org/10.1063/1.4999867.

[57] A. Boschin, P. Johansson, Characterization of NaX (X: TFSI, FSI) – PEO based solid polymer electrolytes for sodium batteries, Electrochim. Acta 175 (2015) 124–133, https://doi.org/10.1016/j.electacta.2015.03.228.

[58] F. Colò, F. Bella, J.R. Nair, M. Destro, C. Gerbaldi, Cellulose-based novel hybrid polymer electrolytes for green and efficient Na-ion batteries, Electrochim. Acta 174 (2015) 185–190, https://doi.org/10.1016/j.electacta.2015.05.178.

[59] Y.L. Ni'mah, M.-Y. Cheng, J.H. Cheng, J. Rick, B.-J. Hwang, Solid-state polymer nanocomposite electrolyte of TiO2/PEO/NaClO4 for sodium ion batteries, J. Power Sources 278 (2015) 375–381, https://doi.org/10.1016/j.jpowsour.2014.11.047.

[60] I. Villaluenga, X. Bogle, S. Greenbaum, I.G. de Muro, T. Rojo, M. Armand, Cation only conduction in new polymer–SiO2 nanohybrids: Na+ electrolytes, J. Mater. Chem. A 1 (2013) 8348–8352, https://doi.org/10.1039/C3TA11290J.

[61] K.-S. Ji, H.-S. Moon, J.-W. Kim, J.-W. Park, Role of functional nano-sized inorganic fillers in poly(ethylene) oxide-based polymer electrolytes, J. Power Sources 117 (2003) 124–130, https://doi.org/10.1016/S0378-7753(03)00159-9.

[62] Z. Zhang, Q. Zhang, C. Ren, F. Luo, Q. Ma, Y.-S. Hu, Z. Zhou, H. Li, X. Huang, L. Chen, A ceramic/polymer composite solid electrolyte for sodium batteries, J. Mater. Chem. A 4 (2016) 15823–15828, https://doi.org/10.1039/C6TA07590H.

[63] A. Bhide, K. Hariharan, Composite polymer electrolyte based on (PEO)6:NaPO3 dispersed with BaTiO3, Polym. Int. 57 (2008) 523–529, https://doi.org/10.1002/pi.2379.

[64] W. Wang, E. Yi, A.J. Fici, R.M. Laine, J. Kieffer, Lithium Ion Conducting Poly(ethylene oxide)-Based Solid Electrolytes Containing Active or Passive Ceramic Nanoparticles, J. Phys. Chem. C. 121 (2017) 2563–2573, https://doi.org/10.1021/acs.jpcc.6b11136.

[65] S.-T. LEE, D.-H. LEE, S.-M. LEE, S.-S. HAN, S.-H. LEE, S.-K. LIM, Effects of calcium impurity on phase relationship, ionic conductivity and microstructure of Na+- β / β″-alumina solid electrolyte, Bull. Mater. Sci. 39 (2016) 729–735, https://doi.org/10.1007/s12034-016-1199-6.

[66] S. Barison, S. Fasolin, C. Mortalò, S. Boldrini, M. Fabrizio, Effect of precursors on β-alumina electrolyte preparation, J. Eur. Ceram. Soc. 35 (2015) 2099–2107, https://doi.org/10.1016/j.jeurceramsoc.2015.01.006.

[67] T. Inoue, K. Mukai, Are All-Solid-State Lithium-Ion Batteries Really Safe?–Verification by Differential Scanning Calorimetry with an All-Inclusive Microcell, ACS Appl. Mater. Interfaces 9 (2017) 1507–1515, https://doi.org/10.1021/acsami.6b13224.

[68] T. Famprikis, J. Dawson, F. Fauth, E. Suard, B. Fleutot, M. Courty, J.-N. Chotard, S. Islam, C. Masquelier, A New Phase of the Na+ Ion Conductor Na3PS4, (2019). https://doi.org/10.26434/chemrxiv.8003717.v1.

[69] T. Famprikis, J.A. Dawson, F. Fauth, O. Clemens, E. Suard, B. Fleutot, M. Courty, J.-N. Chotard, M.S. Islam, C. Masquelier, A New Superionic Plastic Polymorph of the Na+ Conductor Na3PS4, ACS Mater. Lett. 1 (2019) 641–646, https://doi.org/10.1021/acsmaterialslett.9b00322.

[70] Y. Wu, J. Xu, P. Lu, J. Lu, L. Gan, S. Wang, R. Xiao, H. Li, L. Chen, F. Wu, Thermal Stability of Sulfide Solid Electrolyte with Lithium Metal, Adv. Energy Mater. 13 (2023) 2301336, https://doi.org/10.1002/aenm.202301336.

[71] Y. Wu, S. Wang, H. Li, L. Chen, F. Wu, Progress in thermal stability of all-solid-state-Li-ion-batteries, InfoMat 3 (2021) 827–853, https://doi.org/10.1002/inf2.12224.

[72] C. Wang, K. Adair, X. Sun, All-Solid-State Lithium Metal Batteries with Sulfide Electrolytes: Understanding Interfacial Ion and Electron Transport, Acc. Mater. Res. 3 (2022) 21–32, https://doi.org/10.1021/accountsmr.1c00137.

[73] G. Nazri, Preparation, structure and ionic conductivity of lithium phosphide, Solid State Ion.-. 34 (1989) 97–102, https://doi.org/10.1016/0167-2738(89)90438-4.

[74] Q. Luo, C. Liu, C. Wei, Z. Wu, Y. Wang, L. Li, Z. Jiang, L. Ming, J. Yang, L. Zhang, X. Chen, S. Cheng, C. Yu, Deep insight of interfacial stability of LiNi0.7Co0.1Mn0.2O2-based all-solid-state battery with superior performances, J. Power Sources 608 (2024) 234616, https://doi.org/10.1016/j.jpowsour.2024.234616.

[75] Q. Luo, C. Liu, L. Li, Z. Jiang, J. Yang, S. Chen, X. Chen, L. Zhang, S. Cheng, C. Yu, O-doping strategy enabling enhanced chemical/electrochemical stability of Li3InCl6 for superior solid-state battery performance, J. Energy Chem. 99 (2024) 484–494, https://doi.org/10.1016/j.jechem.2024.07.058.

[76] Y.-W. Hu, I.D. Raistrick, R.A. Huggins, Ionic conductivity of lithium phosphate-doped lithium orthosilicate, Mater. Res. Bull. 11 (1976) 1227–1230, https://doi.org/10.1016/0025-5408(76)90025-8.

[77] Y. Deng, C. Eames, B. Fleutot, R. David, J.-N. Chotard, E. Suard, C. Masquelier, M. S. Islam, Enhancing the Lithium Ion Conductivity in Lithium Superionic Conductor (LISICON) Solid Electrolytes through a Mixed Polyanion Effect, ACS Appl. Mater. Interfaces 9 (2017) 7050–7058, https://doi.org/10.1021/acsami.6b14402.

[78] V. Thangadurai, H. Kaack, W.J.F. Weppner, Novel Fast Lithium Ion Conduction in Garnet-Type Li5La3M2O12 (M = Nb, Ta), J. Am. Ceram. Soc. 86 (2003) 437–440, https://doi.org/10.1111/j.1151-2916.2003.tb03318.x.

[79] V. Thangadurai, W. Weppner, Li6ALa2Ta2O12 (A = Sr, Ba): Novel Garnet-Like Oxides for Fast Lithium Ion Conduction, Adv. Funct. Mater. 15 (2005) 107–112, https://doi.org/10.1002/adfm.200400044.

[80] Y. Li, J.-T. Han, C.-A. Wang, H. Xie, J.B. Goodenough, Optimizing Li+ conductivity in a garnet framework, J. Mater. Chem. 22 (2012) 15357–15361, https://doi.org/10.1039/C2JM31413D.

[81] J.-F. Wu, E.-Y. Chen, Y. Yu, L. Liu, Y. Wu, W.K. Pang, V.K. Peterson, X. Guo, Gallium-Doped Li7La3Zr2O12 Garnet-Type Electrolytes with High Lithium-Ion Conductivity, ACS Appl. Mater. Interfaces 9 (2017) 1542–1552, https://doi.org/10.1021/acsami.6b13902.

[82] V. Thangadurai, A.K. Shukla, J. Gopalakrishnan, LiSr1.650.35B1.3B‘1.7O9 (B = Ti, Zr; B‘ = Nb, Ta): New Lithium Ion Conductors Based on the Perovskite

Structure, Chem. Mater. 11 (1999) 835–839, https://doi.org/10.1021/cm9810382.

[83] C.H. Chen, S. Xie, E. Sperling, A.S. Yang, G. Henriksen, K. Amine, Stable lithium-ion conducting perovskite lithium–strontium–tantalum–zirconium–oxide system, Solid State Ion.-. 167 (2004) 263–272, https://doi.org/10.1016/j.ssi.2004.01.008.

[84] B. Huang, B. Xu, Y. Li, W. Zhou, Y. You, S. Zhong, C.-A. Wang, J.B. Goodenough, Li-Ion Conduction and Stability of Perovskite Li3/8Sr7/16Hf1/4Ta3/4O3, ACS Appl. Mater. Interfaces 8 (2016) 14552–14557, https://doi.org/10.1021/acsami.6b03070.

[85] A. Hayashi, S. Hama, H. Morimoto, M. Tatsumisago, T. Minami, High Lithium Ion Conductivity of Glass–Ceramics Derived from Mechanically Milled Glassy Powders, Chem. Lett. 30 (2001) 872–873, https://doi.org/10.1246/cl.2001.872.

[86] N. Kamaya, K. Homma, Y. Yamakawa, M. Hirayama, R. Kanno, M. Yonemura, T. Kamiyama, Y. Kato, S. Hama, K. Kawamoto, A. Mitsui, A lithium superionic conductor, Nat. Mater. 10 (2011) 682–686, https://doi.org/10.1038/nmat3066.

[87] S. Boulineau, M. Courty, J.-M. Tarascon, V. Viallet, Mechanochemical synthesis of Li-argyrodite Li6PS5X (X=Cl, Br, I) as sulfur-based solid electrolytes for all solid state batteries application, Solid State Ion.-. 221 (2012) 1–5, https://doi.org/10.1016/j.ssi.2012.06.008.

[88] R.P. Rao, S. Adams, Studies of lithium argyrodite solid electrolytes for all-solid-state batteries, Phys. Status Solidi A 208 (2011) 1804–1807, https://doi.org/10.1002/pssa.201001117.

[89] O. Pecher, S.-T. Kong, T. Goebel, V. Nickel, K. Weichert, C. Reiner, H.-J. Deiseroth, J. Maier, F. Haarmann, D. Zahn, Atomistic Characterisation of Li+ Mobility and Conductivity in Li7−xPS6−xIx Argyrodites from Molecular Dynamics Simulations, Solid-State NMR, and Impedance Spectroscopy, Chem. – Eur. J. 16 (2010) 8347–8354, https://doi.org/10.1002/chem.201000501.

[90] C.R. Milian Pila, E.P. Cappe, N.D.S. Mohallem, O.L. Alves, M.A. Aguilar Frutis, N. Sánchez-Ramírez, R.M. Torresi, H. León Ramírez, Y.M. Laffita, Effect of the LLTO nanoparticles on the conducting properties of PEO-based solid electrolyte, Solid State Sci. 88 (2019) 41–47, https://doi.org/10.1016/j.solidstatesciences.2018.10.014.

[91] Z. Li, H.-M. Huang, J.-K. Zhu, J.-F. Wu, H. Yang, L. Wei, X. Guo, Ionic Conduction in Composite Polymer Electrolytes: Case of PEO:Ga-LLZO Composites, ACS Appl. Mater. Interfaces 11 (2019) 784–791, https://doi.org/10.1021/acsami.8b17279.

[92] Z. Xu, X. Chen, K. Liu, R. Chen, X. Zeng, H. Zhu, Influence of Anion Charge on Li Ion Diffusion in a New Solid-State Electrolyte, Li3LaI6, Chem. Mater. 31 (2019) 7425–7433, https://doi.org/10.1021/acs.chemmater.9b02075.

[93] W.I. Archer, R.D. Armstrong, D.P. Sellick, W.G. Bugden, J.H. Duncan, The relationship between the a.c. impedance and microstructure of a sodium β-alumina ceramic, J. Mater. Sci. 15 (1980) 2066–2072, https://doi.org/10.1007/BF00550633.

[94] G.J. May, A. Hooper, The effect of microstructure and phase composition on the ionic conductivity of magnesium-doped sodium-beta-alumina, J. Mater. Sci. 13 (1978) 1480–1486, https://doi.org/10.1007/BF00553202.

[95] Y. Sheng, P. Sarkar, P.S. Nicholson, The mechanical and electrical properties of ZrO2-Naβ″-Al2O3 composites, J. Mater. Sci. 23 (1988) 958–967, https://doi.org/10.1007/BF01153995.

[96] J.P. Boilot, G. Collin, Ph Colomban, Relation structure-fast ion conduction in the NASICON solid solution, J. Solid State Chem. 73 (1988) 160–171, https://doi.org/10.1016/0022-4596(88)90065-5.

[97] J. Yang, G. Liu, M. Avdeev, H. Wan, F. Han, L. Shen, Z. Zou, S. Shi, Y.-S. Hu, C. Wang, X. Yao, Ultrastable All-Solid-State Sodium Rechargeable Batteries, ACS Energy Lett. 5 (2020) 2835–2841, https://doi.org/10.1021/acsenergylett.0c01432.

[98] Z. Zhang, Z. Zou, K. Kaup, R. Xiao, S. Shi, M. Avdeev, Y.-S. Hu, D. Wang, B. He, H. Li, X. Huang, L.F. Nazar, L. Chen, Correlated Migration Invokes Higher Na+-Ion Conductivity in NaSICON-Type Solid Electrolytes, Adv. Energy Mater. 9 (2019) 1902373, https://doi.org/10.1002/aenm.201902373.

[99] Z. Zhang, Q. Zhang, J. Shi, Y.S. Chu, X. Yu, K. Xu, M. Ge, H. Yan, W. Li, L. Gu, Y.-S. Hu, H. Li, X.-Q. Yang, L. Chen, X. Huang, A Self-Forming Composite Electrolyte for Solid-State Sodium Battery with Ultralong Cycle Life, Adv. Energy Mater. 7 (2017) 1601196, https://doi.org/10.1002/aenm.201601196.

[100] X. Wang, J. Chen, Z. Mao, D. Wang, Effective resistance to dendrite growth of NASICON solid electrolyte with lower electronic conductivity, Chem. Eng. J. 427 (2022) 130899, https://doi.org/10.1016/j.cej.2021.130899.

[101] C. Huang, G. Yang, W. Yu, C. Xue, Y. Zhai, W. Tang, N. Hu, Z. Wen, L. Lu, S. Song, Gallium-substituted Nasicon Na3Zr2Si2PO12 solid electrolytes, J. Alloy. Compd. 855 (2021) 157501, https://doi.org/10.1016/j.jallcom.2020.157501.

[102] Q. Ma, M. Guin, S. Naqash, C.-L. Tsai, F. Tietz, O. Guillon, Scandium-Substituted Na3Zr2(SiO4)2(PO4) Prepared by a Solution-Assisted Solid-State Reaction Method as Sodium-Ion Conductors, Chem. Mater. 28 (2016) 4821–4828, https://doi.org/10.1021/acs.chemmater.6b02059.

[103] J. Serra Moreno, M. Armand, M.B. Berman, S.G. Greenbaum, B. Scrosati, S. Panero, Composite PEOn:NaTFSI polymer electrolyte: Preparation, thermal and electrochemical characterization, J. Power Sources 248 (2014) 695–702, https://doi.org/10.1016/j.jpowsour.2013.09.137.

[104] C. Zhao, L. Liu, Y. Lu, M. Wagemaker, L. Chen, Y.-S. Hu, Revealing an Interconnected Interfacial Layer in Solid-State Polymer Sodium Batteries, Angew. Chem. Int. Ed. 58 (2019) 17026–17032, https://doi.org/10.1002/anie.201909877.

[105] X. Qi, Q. Ma, L. Liu, Y.-S. Hu, H. Li, Z. Zhou, X. Huang, L. Chen, Sodium Bis(fluorosulfonyl)imide/Poly(ethylene oxide) Polymer Electrolytes for Sodium-Ion Batteries, ChemElectroChem 3 (2016) 1741–1745, https://doi.org/10.1002/celc.201600221.

[106] H. Che, S. Chen, Y. Xie, H. Wang, K. Amine, X.-Z. Liao, Z.-F. Ma, Electrolyte design strategies and research progress for room-temperature sodium-ion batteries, Energy Environ. Sci. 10 (2017) 1075–1101, https://doi.org/10.1039/C7EE00524E.

[107] S.A. Hashmi, S. Chandra, Experimental investigations on a sodium-ion-conducting polymer electrolyte based on poly(ethylene oxide) complexed with NaPF6, Mater. Sci. Eng. B 34 (1995) 18–26, https://doi.org/10.1016/0921-5107(95)01219-2.

[108] Z. Osman, K.B. Md Isa, A. Ahmad, L. Othman, A comparative study of lithium and sodium salts in PAN-based ion conducting polymer electrolytes, Ionics 16 (2010) 431–435, https://doi.org/10.1007/s11581-009-0410-9.

[109] P.B. Bhargav, V.M. Mohan, A.K. Sharma, V.V.R.N. Rao, Characterization of poly(vinyl alcohol)/sodium bromide polymer electrolytes for electrochemical cell applications, J. Appl. Polym. Sci. 108 (2008) 510–517, https://doi.org/10.1002/app.27566.

[110] K. West, B. Zachau-Christiansen, T. Jacobsen, E. Hiort-Lorenzen, S. Skaarup, Poly(ethylene oxide)-sodium perchlorate electrolytes in solid-state sodium cells, Br. Polym. J. 20 (1988) 243–246, https://doi.org/10.1002/pi.4980200315.

[111] M. Jansen, U. Henseler, Synthesis, structure determination, and ionic conductivity of sodium tetrathiophosphate, J. Solid State Chem. 99 (1992) 110–119, https://doi.org/10.1016/0022-4596(92)90295-7.

[112] D. Zhang, X. Cao, D. Xu, N. Wang, C. Yu, W. Hu, X. Yan, J. Mi, B. Wen, L. Wang, L. Zhang, Synthesis of cubic Na3SbS4 solid electrolyte with enhanced ion transport for all-solid-state sodium-ion batteries, Electrochim. Acta 259 (2018) 100–109, https://doi.org/10.1016/j.electacta.2017.10.173.

[113] Z. Zhang, E. Ramos, F. Lalère, A. Assoud, K. Kaup, P. Hartman, L.F. Nazar, Na11Sn2PS12: a new solid state sodium superionic conductor, Energy Environ. Sci. 11 (2018) 87–93, https://doi.org/10.1039/C7EE03083E.

[114] K. Oh, D. Chang, I. Park, K. Yoon, K. Kang, First-Principles Investigations on Sodium Superionic Conductor $Na_{11}Sn_2PS_{12}$, Chem. Mater. 31 (2019) 6066–6075, https://doi.org/10.1021/acs.chemmater.8b04965.

[115] Y. Wang, W.D. Richards, S.-H. Bo, L.J. Miara, G. Ceder, Computational Prediction and Evaluation of Solid-State Sodium Superionic Conductors $Na_7P_3X_{11}$ (X = O, S, Se), Chem. Mater. 29 (2017) 7475–7482, https://doi.org/10.1021/acs.chemmater.7b02476.

[116] N. Tanibata, K. Noi, A. Hayashi, M. Tatsumisago, Preparation and characterization of highly sodium ion conducting Na 3 PS 4 –Na 4 SiS 4 solid electrolytes, RSC Adv. 4 (2014) 17120–17123, https://doi.org/10.1039/C4RA00996G.

[117] H. Mehrer, Diffusion in Solids: Fundamentals, Methods, Materials, Diffusion-Controlled Processes, Springer Science & Business Media, 2007.

[118] X. He, Y. Zhu, Y. Mo, Origin of fast ion diffusion in super-ionic conductors, Nat. Commun. 8 (2017) 15893, https://doi.org/10.1038/ncomms15893.

[119] J. Huang, K. Wu, G. Xu, M. Wu, S. Dou, C. Wu, Recent progress and strategic perspectives of inorganic solid electrolytes: fundamentals, modifications, and applications in sodium metal batteries, Chem. Soc. Rev. 52 (2023) 4933–4995, https://doi.org/10.1039/D2CS01029A.

[120] Z. Wang, G. Shao, Theoretical design of solid electrolytes with superb ionic conductivity: alloying effect on Li^+ transportation in cubic Li_6PA_5X chalcogenides, J. Mater. Chem. A 5 (2017) 21846–21857, https://doi.org/10.1039/C7TA06986C.

[121] S.-H. Bo, Y. Wang, J.C. Kim, W.D. Richards, G. Ceder, Computational and Experimental Investigations of Na-Ion Conduction in Cubic Na3PSe4, Chem. Mater. 28 (2016) 252–258, https://doi.org/10.1021/acs.chemmater.5b04013.

[122] Z. Zhang, P.-N. Roy, H. Li, M. Avdeev, L.F. Nazar, Coupled Cation–Anion Dynamics Enhances Cation Mobility in Room-Temperature Superionic Solid-State Electrolytes, J. Am. Chem. Soc. 141 (2019) 19360–19372, https://doi.org/10.1021/jacs.9b09343.

[123] Z. Zhang, H. Li, K. Kaup, L. Zhou, P.-N. Roy, L.F. Nazar, Targeting Superionic Conductivity by Turning on Anion Rotation at Room Temperature in Fast Ion Conductors, Matter 2 (2020) 1667–1684, https://doi.org/10.1016/j.matt.2020.04.027.

[124] J.G. Smith, D.J. Siegel, Low-temperature paddlewheel effect in glassy solid electrolytes, Nat. Commun. 11 (2020) 1483, https://doi.org/10.1038/s41467-020-15245-5.

[125] Y. Sun, Y. Wang, X. Liang, Y. Xia, L. Peng, H. Jia, H. Li, L. Bai, J. Feng, H. Jiang, J. Xie, Rotational Cluster Anion Enabling Superionic Conductivity in Sodium-Rich Antiperovskite Na3OBH4, J. Am. Chem. Soc. 141 (2019) 5640–5644, https://doi.org/10.1021/jacs.9b01746.

[126] Z. Zhang, L.F. Nazar, Exploiting the paddle-wheel mechanism for the design of fast ion conductors, Nat. Rev. Mater. 7 (2022) 389–405, https://doi.org/10.1038/s41578-021-00401-0.

[127] E.P. Ramos, Z. Zhang, A. Assoud, K. Kaup, F. Lalère, L.F. Nazar, Correlating Ion Mobility and Single Crystal Structure in Sodium-Ion Chalcogenide-Based Solid State Fast Ion Conductors: Na11Sn2PnS12 (Pn = Sb, P), Chem. Mater. 30 (2018) 7413–7417, https://doi.org/10.1021/acs.chemmater.8b02077.

[128] J. Heo, A. Banerjee, K.H. Park, Y.S. Jung, S.-T. Hong, New Na-Ion Solid Electrolytes Na 4− x Sn 1− x Sb x S 4 (0.02 ≤ x ≤ 0.33) for All-Solid-State Na-Ion Batteries, Adv. Energy Mater. 8 (2018) 1702716, https://doi.org/10.1002/aenm.201702716.

[129] M. Duchardt, U. Ruschewitz, S. Adams, S. Dehnen, B. Roling, Vacancy-Controlled Na+ Superion Conduction in Na11 Sn2 PS12, Angew. Chem. Int. Ed. Engl. 57 (2018) 1351–1355, https://doi.org/10.1002/anie.201712769.

[130] Z. Yu, S.-L. Shang, D. Wang, Y.C. Li, H.P. Yennawar, G. Li, H.-T. Huang, Y. Gao, T. E. Mallouk, Z.-K. Liu, D. Wang, Synthesis and understanding of Na11Sn2PSe12

with enhanced ionic conductivity for all-solid-state Na-ion battery, Energy Storage Mater. 17 (2019) 70–77, https://doi.org/10.1016/j.ensm.2018.11.027.

[131] I. Hanghofer, B. Gadermaier, H.M.R. Wilkening, Fast Rotational Dynamics in Argyrodite-Type Li6PS5X (X: Cl, Br, I) as Seen by 31P Nuclear Magnetic Relaxation—On Cation–Anion Coupled Transport in Thiophosphates, Chem. Mater. 31 (2019) 4591–4597, https://doi.org/10.1021/acs.chemmater.9b01435.

[132] N. Adelstein, B.C. Wood, Role of Dynamically Frustrated Bond Disorder in a Li+ Superionic Solid Electrolyte, Chem. Mater. 28 (2016) 7218–7231, https://doi.org/10.1021/acs.chemmater.6b00790.

[133] E. Wu, S. Banerjee, H. Tang, P.M. Richardson, J.-M. Doux, J. Qi, Z. Zhu, A. Grenier, Y. Li, E. Zhao, G. Deysher, H. Nguyen, R. Stephens, G. Verbist, K.W. Chapman, R.J. Clément, A. Banerjee, Y.S. Meng, S.P. Ong, A. Stable Cathode-Solid Electrolyte Composite for Long-Cycle-Life, High Voltage Solid-State Sodium-ion Batteries, (2020). https://doi.org/10.26434/chemrxiv.12730964.v1.

[134] H. Yamane, M. Shibata, Y. Shimane, T. Junke, Y. Seino, S. Adams, K. Minami, A. Hayashi, M. Tatsumisago, Crystal structure of a superionic conductor, Li7P3S11, Solid State Ion.-. 178 (2007) 1163–1167, https://doi.org/10.1016/j.ssi.2007.05.020.

[135] S.T. Kong, Ö. Gün, B. Koch, H.J. Deiseroth, H. Eckert, C. Reiner, Structural Characterisation of the Li Argyrodites Li7PS6 and Li7PSe6 and their Solid Solutions: Quantification of Site Preferences by MAS NMR Spectroscopy, Chem. – Eur. J. 16 (2010) 5138–5147, https://doi.org/10.1002/chem.200903023.

[136] R. Kanno, T. Hata, Y. Kawamoto, M. Irie, Synthesis of a new lithium ionic conductor, thio-LISICON–lithium germanium sulfide system, Solid State Ion.-. 130 (2000) 97–104, https://doi.org/10.1016/S0167-2738(00)00277-0.

[137] R. Kanno, M. Murayama, Lithium Ionic Conductor Thio-LISICON: The Li2 S - GeS2 - P 2 S 5 System, J. Electrochem. Soc. 148 (2001) A742, https://doi.org/10.1149/1.1379028.

[138] P. Bron, S. Johansson, K. Zick, J. Schmedt auf der Günne, S. Dehnen, B. Roling, Li10SnP2S12: An Affordable Lithium Superionic Conductor, J. Am. Chem. Soc. 135 (2013) 15694–15697, https://doi.org/10.1021/ja407393y.

[139] P. Bron, S. Dehnen, B. Roling, Li10Si0.3Sn0.7P2S12 – A low-cost and low-grain-boundary-resistance lithium superionic conductor, J. Power Sources 329 (2016) 530–535, https://doi.org/10.1016/j.jpowsour.2016.08.115.

[140] H.M. Chen, C. Maohua, S. Adams, Stability and ionic mobility in argyrodite-related lithium-ion solid electrolytes, Phys. Chem. Chem. Phys. 17 (2015) 16494–16506, https://doi.org/10.1039/C5CP01841B.

[141] L. Zhou, N. Minafra, W.G. Zeier, L.F. Nazar, Innovative Approaches to Li-Argyrodite Solid Electrolytes for All-Solid-State Lithium Batteries, Acc. Chem. Res. 54 (2021) 2717–2728, https://doi.org/10.1021/acs.accounts.0c00874.

[142] N. Minafra, M.A. Kraft, T. Bernges, C. Li, R. Schlem, B.J. Morgan, W.G. Zeier, Local Charge Inhomogeneity and Lithium Distribution in the Superionic Argyrodites Li6PS5X (X = Cl, Br, I), Inorg. Chem. 59 (2020) 11009–11019, https://doi.org/10.1021/acs.inorgchem.0c01504.

[143] C. Yu, S. Ganapathy, N.J.J. de Klerk, I. Roslon, E.R.H. van Eck, A.P.M. Kentgens, M. Wagemaker, Unravelling Li-Ion Transport from Picoseconds to Seconds: Bulk versus Interfaces in an Argyrodite Li6PS5Cl–Li2S All-Solid-State Li-Ion Battery, J. Am. Chem. Soc. 138 (2016) 11192–11201, https://doi.org/10.1021/jacs.6b05066.

[144] H.-J. Deiseroth, S.-T. Kong, H. Eckert, J. Vannahme, C. Reiner, T. Zaiß, M. Schlosser, Li6PS5X: A Class of Crystalline Li-Rich Solids With an Unusually High Li+ Mobility, Angew. Chem. Int. Ed. 47 (2008) 755–758, https://doi.org/10.1002/anie.200703900.

[145] M.A. Kraft, S.P. Culver, M. Calderon, F. Böcher, T. Krauskopf, A. Senyshyn, C. Dietrich, A. Zevalkink, J. Janek, W.G. Zeier, Influence of Lattice Polarizability on the Ionic Conductivity in the Lithium Superionic Argyrodites Li6PS5X (X = Cl, Br, I), J. Am. Chem. Soc. 139 (2017) 10909–10918, https://doi.org/10.1021/jacs.7b06327.

[146] M.A. Kraft, S. Ohno, T. Zinkevich, R. Koerver, S.P. Culver, T. Fuchs, A. Senyshyn, S. Indris, B.J. Morgan, W.G. Zeier, Inducing High Ionic Conductivity in the Lithium Superionic Argyrodites Li6+xP1–xGexS5I for All-Solid-State Batteries, J. Am. Chem. Soc. 140 (2018) 16330–16339, https://doi.org/10.1021/jacs.8b10282.

[147] S. Wenzel, S.J. Sedlmaier, C. Dietrich, W.G. Zeier, J. Janek, Interfacial reactivity and interphase growth of argyrodite solid electrolytes at lithium metal electrodes, Solid State Ion.-. 318 (2018) 102–112, https://doi.org/10.1016/j.ssi.2017.07.005.

[148] M.V. Reddy, C. Julien, A. Mauger, K. Zaghib, Sulfide and Oxide Inorganic Solid Electrolytes for All-Solid-State Li Batteries: A Review, Nanomaterials 10 (2020) 1606, https://doi.org/10.3390/nano10081606.

[149] N.J.J. De Klerk, I. Rosłoń, M. Wagemaker, Diffusion Mechanism of Li Argyrodite Solid Electrolytes for Li-Ion Batteries and Prediction of Optimized Halogen Doping: The Effect of Li Vacancies, Halogens, and Halogen Disorder, Chem. Mater. 28 (2016) 7955–7963, https://doi.org/10.1021/acs.chemmater.6b03630.

[150] R. Schlenker, A.-L. Hansen, A. Senyshyn, T. Zinkevich, M. Knapp, T. Hupfer, H. Ehrenberg, S. Indris, Structure and Diffusion Pathways in Li_6PS_5Cl Argyrodite from Neutron Diffraction, Pair-Distribution Function Analysis, and NMR, Chem. Mater. 32 (2020) 8420–8430, https://doi.org/10.1021/acs.chemmater.0c02418.

[151] G. Foran, N. Verdier, D. Lepage, C. Malveau, N. Dupré, M. Dollé, Use of Solid-State NMR Spectroscopy for the Characterization of Molecular Structure and Dynamics in Solid Polymer and Hybrid Electrolytes, Polymers 13 (2021), https://doi.org/10.3390/polym13081207.

[152] N.J. Dudney, W.C. West, J. Nanda, Handbook Of Solid State Batteries (Second Edition), World Scientific, 2015.

[153] M. Wilkening, P. Heitjans, From Micro to Macro: Access to Long-Range Li+ Diffusion Parameters in Solids via Microscopic 6, 7Li Spin-Alignment Echo NMR Spectroscopy, ChemPhysChem 13 (2012) 53–65, https://doi.org/10.1002/cphc.201100580.

[154] A. Kuhn, J.-Y. Choi, L. Robben, F. Tietz, M. Wilkening, P. Heitjans, Li Ion Dynamics in Al-Doped Garnet-Type Li7La3Zr2O12 Crystallizing with Cubic Symmetry, Z. F. üR. Phys. Chem. 226 (2012) 525–537, https://doi.org/10.1524/zpch.2012.0250.

[155] I. Hanghofer, M. Brinek, S.L. Eisbacher, B. Bitschnau, M. Volck, V. Hennige, I. Hanzu, D. Rettenwander, H.M.R. Wilkening, Substitutional disorder: structure and ion dynamics of the argyrodites Li6PS5Cl, Li6PS5Br and Li6PS5I, Phys. Chem. Chem. Phys. 21 (2019) 8489–8507, https://doi.org/10.1039/C9CP00664H.

[156] A. Einstein, Über die von der molekularkinetischen Theorie der Wärme geforderte Bewegung von in ruhenden Flüssigkeiten suspendierten Teilchen, Ann. Phys. 322 (1905) 549–560, https://doi.org/10.1002/andp.19053220806.

[157] M. Smoluchowski, Zur kinetischen Theorie der Brownschen Molekularbewegung und der Suspensionen, Ann. Phys. 326 (2006) 756–780, https://doi.org/10.1002/andp.19063261405.

[158] R.A. McKee, A generalization of the nernst-Einstein equation for self-diffusion in high defect concentration solids, Solid State Ion.-. 5 (1981) 133–136, https://doi.org/10.1016/0167-2738(81)90210-1.

[159] H.R. Zeller, P. Brüesch, L. Pietronero, S. Strässler, Lattice Dynamics and Ionic Motion in Superionic Conductors, in: G.D. Mahan, W.L. Roth (Eds.), Superionic Conduct, Springer US, Boston, MA, 1976, pp. 201–215, https://doi.org/10.1007/978-1-4615-8789-7_22.

[160] M.J. Rice, W.L. Roth, Ionic transport in super ionic conductors: a theoretical model, J. Solid State Chem. 4 (1972) 294–310, https://doi.org/10.1016/0022-4596(72)90121-1.

[161] S. Ghosh, S. Chatterjee, A.N. Basu, Phase Transition and Soft Mode Behaviour in Superionic Copper Halides, Phys. Status Solidi B 123 (1984) 445–451, https://doi.org/10.1002/pssb.2221230206.

[162] P.R. Rayavarapu, N. Sharma, V.K. Peterson, S. Adams, Variation in structure and Li+-ion migration in argyrodite-type Li6PS5X (X = Cl, Br, I) solid electrolytes, J. Solid State Electrochem. 16 (2012) 1807–1813, https://doi.org/10.1007/s10008-011-1572-8.

[163] R.D. Shannon, Revised effective ionic radii and systematic studies of interatomic distances in halides and chalcogenides, Acta Crystallogr. A 32 (1976) 751–767, https://doi.org/10.1107/S0567739476001551.

[164] L.L. Baranowski, C.M. Heveran, V.L. Ferguson, C.R. Stoldt, Multi-Scale Mechanical Behavior of the Li3PS4 Solid-Phase Electrolyte, ACS Appl. Mater. Interfaces 8 (2016) 29573–29579, https://doi.org/10.1021/acsami.6b06612.

[165] K.-D. Kreuer, H. Kohler, J. Maier, Sodium ion conductors with nasicon framework structure. in: High Conduct. Solid Ion. Conduct., WORLD SCIENTIFIC, 1989, pp. 242–279, https://doi.org/10.1142/9789814434294_0011.

[166] R. Metselaar, G. Oversluizen, The meyer-neldel rule in semiconductors, J. Solid State Chem. 55 (1984) 320–326, https://doi.org/10.1016/0022-4596(84)90284-6.

[167] K.L. Ngai, Meyer–Neldel rule and anti Meyer–Neldel rule of ionic conductivity: Conclusions from the coupling model, Solid State Ion.-. 105 (1998) 231–235, https://doi.org/10.1016/S0167-2738(97)00469-4.

[168] A.S. Nowick, W.-K. Lee, H. Jain, Survey and interpretation of pre-exponentials of conductivity, Solid State Ion.-. 28–30 (1988) 89–94, https://doi.org/10.1016/S0167-2738(88)80013-4.

[169] D. Knödler, P. Pendzig, W. Dieterich, Ion dynamics in structurally disordered materials: effects of random Coulombic traps, Solid State Ion.-. 86–88 (1996) 29–39, https://doi.org/10.1016/0167-2738(96)00089-6.

[170] H. Wang, C. Yu, S. Ganapathy, E.R.H. van Eck, L. van Eijck, M. Wagemaker, A lithium argyrodite Li6PS5Cl0.5Br0.5 electrolyte with improved bulk and interfacial conductivity, J. Power Sources 412 (2019) 29–36, https://doi.org/10.1016/j.jpowsour.2018.11.029.

[171] C. Yu, L. van Eijck, S. Ganapathy, M. Wagemaker, Synthesis, structure and electrochemical performance of the argyrodite Li6PS5Cl solid electrolyte for Li-ion solid state batteries, Electrochim. Acta 215 (2016) 93–99, https://doi.org/10.1016/j.electacta.2016.08.081.

[172] C. Yu, S. Ganapathy, E.R.H. van Eck, H. Wang, S. Basak, Z. Li, M. Wagemaker, Accessing the bottleneck in all-solid state batteries, lithium-ion transport over the solid-electrolyte-electrode interface, Nat. Commun. 8 (2017) 1086, https://doi.org/10.1038/s41467-017-01187-y.

[173] C. Yu, S. Ganapathy, E.R.H. van Eck, L. van Eijck, S. Basak, Y. Liu, L. Zhang, H. W. Zandbergen, M. Wagemaker, Revealing the relation between the structure, Li-ion conductivity and solid-state battery performance of the argyrodite Li6PS5Br solid electrolyte, J. Mater. Chem. A 5 (2017) 21178–21188, https://doi.org/10.1039/C7TA05031C.

[174] Y. Zhang, R. Chen, T. Liu, Y. Shen, Y. Lin, C.-W. Nan, High Capacity, Superior Cyclic Performances in All-Solid-State Lithium-Ion Batteries Based on 78Li2S-22P2S5 Glass-Ceramic Electrolytes Prepared via Simple Heat Treatment, ACS Appl. Mater. Interfaces 9 (2017) 28542–28548, https://doi.org/10.1021/acsami.7b06038.

[175] M. Eom, S. Son, C. Park, S. Noh, W.T. Nichols, D. Shin, High performance all-solid-state lithium-sulfur battery using a Li2S-VGCF nanocomposite, Electrochim. Acta 230 (2017) 279–284, https://doi.org/10.1016/j.electacta.2017.01.155.

[176] E. Gil-González, L. Ye, Y. Wang, Z. Shadike, Z. Xu, E. Hu, X. Li, Synergistic effects of chlorine substitution in sulfide electrolyte solid state batteries, Energy Storage Mater. 45 (2022) 484–493, https://doi.org/10.1016/j.ensm.2021.12.008.

[177] P. Wang, H. Liu, S. Patel, X. Feng, P.-H. Chien, Y. Wang, Y.-Y. Hu, Fast Ion Conduction and Its Origin in Li6–xPS5–xBr1+x, Chem. Mater. 32 (2020) 3833–3840, https://doi.org/10.1021/acs.chemmater.9b05331.

[178] P. Wang, S. Patel, H. Liu, P.-H. Chien, X. Feng, L. Gao, B. Chen, J. Liu, Y.-Y. Hu, Configurational and Dynamical Heterogeneity in Superionic Li5.3PS4.3Cl1.7−xBrx, Adv. Funct. Mater. n/a (n.d.) 2307954. https://doi.org/10.1002/adfm.202307954.

[179] T. Asano, A. Sakai, S. Ouchi, M. Sakaida, A. Miyazaki, S. Hasegawa, Solid Halide Electrolytes with High Lithium-Ion Conductivity for Application in 4V Class Bulk-Type All-Solid-State Batteries, Adv. Mater. 30 (2018) 1803075, https://doi.org/10.1002/adma.201803075.

[180] Z. Zhu, I.-H. Chu, S.P. Ong, Li3Y(PS4)2 and Li5PS4Cl2: New Lithium Superionic Conductors Predicted from Silver Thiophosphates using Efficiently Tiered Ab Initio Molecular Dynamics Simulations, Chem. Mater. 29 (2017) 2474–2484, https://doi.org/10.1021/acs.chemmater.6b04049.

[181] P. Adeli, J.D. Bazak, K.H. Park, I. Kochetkov, A. Huq, G.R. Goward, L.F. Nazar, Boosting Solid-State Diffusivity and Conductivity in Lithium Superionic Argyrodites by Halide Substitution, Angew. Chem. Int. Ed. 58 (2019) 8681–8686, https://doi.org/10.1002/anie.201814222.

[182] X. Feng, P.-H. Chien, Y. Wang, S. Patel, P. Wang, H. Liu, M. Immediato-Scuotto, Y.-Y. Hu, Enhanced ion conduction by enforcing structural disorder in Li-deficient argyrodites Li6−xPS5−xCl1+x, Energy Storage Mater. 30 (2020) 67–73, https://doi.org/10.1016/j.ensm.2020.04.042.

[183] C. Yu, Y. Li, M. Willans, Y. Zhao, K.R. Adair, F. Zhao, W. Li, S. Deng, J. Liang, M. N. Banis, R. Li, H. Huang, L. Zhang, R. Yang, S. Lu, Y. Huang, X. Sun, Superionic conductivity in lithium argyrodite solid-state electrolyte by controlled Cl-doping, Nano Energy 69 (2020) 104396, https://doi.org/10.1016/j.nanoen.2019.104396.

[184] C. Yu, Y. Li, W. Li, K.R. Adair, F. Zhao, M. Willans, J. Liang, Y. Zhao, C. Wang, S. Deng, R. Li, H. Huang, S. Lu, T.-K. Sham, Y. Huang, X. Sun, Enabling ultrafast ionic conductivity in Br-based lithium argyrodite electrolytes for solid-state batteries with different anodes, Energy Storage Mater. 30 (2020) 238–249, https://doi.org/10.1016/j.ensm.2020.04.014.

[185] J. Duan, Y. Zheng, W. Luo, W. Wu, T. Wang, Y. Xie, S. Li, J. Li, Y. Huang, Is graphite lithiophobic or lithiophilic? Natl. Sci. Rev. 7 (2020) 1208–1217, https://doi.org/10.1093/nsr/nwz222.

[186] C. Wei, Y. Xiao, Z. Wu, C. Liu, Q. Luo, Z. Jiang, L. Li, L. Ming, J. Yang, S. Cheng, C. Yu, Construction of LiCl/LiF/LiZn hybrid SEI interface achieving high-performance sulfide-based all-solid-state lithium metal batteries, Sci. China Chem. 67 (2024) 1990–2001, https://doi.org/10.1007/s11426-024-2055-4.

[187] Z. Wu, C. Liu, Z. Jiang, L. Li, S. Li, C. Wei, Q. Luo, X. Chen, L. Zhang, S. Cheng, C. Yu, Enhancing solid-state lithium metal battery performance via indium-based modification of electrolytes and lithium metal surfaces: mechanistic insights and optimization, Sci. China Chem. (2024), https://doi.org/10.1007/s11426-024-2275-2.

[188] Z. Zhang, J. Zhang, H. Jia, L. Peng, T. An, J. Xie, Enhancing ionic conductivity of solid electrolyte by lithium substitution in halogenated Li-Argyrodite, J. Power Sources 450 (2020) 227601, https://doi.org/10.1016/j.jpowsour.2019.227601.

[189] P. Adeli, J.D. Bazak, A. Huq, G.R. Goward, L.F. Nazar, Influence of Aliovalent Cation Substitution and Mechanical Compression on Li-Ion Conductivity and Diffusivity in Argyrodite Solid Electrolytes, Chem. Mater. 33 (2021) 146–157, https://doi.org/10.1021/acs.chemmater.0c03090.

[190] T. Bernges, S.P. Culver, N. Minafra, R. Koerver, W.G. Zeier, Competing Structural Influences in the Li Superionic Conducting Argyrodites Li6PS5–xSexBr ($0 \leq x \leq 1$) upon Se Substitution, Inorg. Chem. 57 (2018) 13920–13928, https://doi.org/10.1021/acs.inorgchem.8b02443.

[191] R. Schlem, M. Ghidiu, S.P. Culver, A.-L. Hansen, W.G. Zeier, Changing the Static and Dynamic Lattice Effects for the Improvement of the Ionic Transport Properties within the Argyrodite Li6PS5–xSexI, ACS Appl. Energy Mater. 3 (2020) 9–18, https://doi.org/10.1021/acsaem.9b01794.

[192] M. Xuan, W. Xiao, H. Xu, Y. Shen, Z. Li, S. Zhang, Z. Wang, G. Shao, Ultrafast solid-state lithium ion conductor through alloying induced lattice softening of Li6PS5Cl, J. Mater. Chem. A 6 (2018) 19231–19240, https://doi.org/10.1039/C8TA07240J.

[193] Z. Deng, Z. Zhu, I.-H. Chu, S.P. Ong, Data-Driven First-Principles Methods for the Study and Design of Alkali Superionic Conductors, Chem. Mater. 29 (2017) 281–288, https://doi.org/10.1021/acs.chemmater.6b02648.

[194] N. Minafra, S.P. Culver, T. Krauskopf, A. Senyshyn, W.G. Zeier, Effect of Si substitution on the structural and transport properties of superionic Li-argyrodites, J. Mater. Chem. A 6 (2018) 645–651, https://doi.org/10.1039/C7TA08581H.

[195] R. Shannon, C. Prewitt, Revised Values of Effective Ionic Radii, Acta Crystallogr. B 26 (1970) 1046–1048, https://doi.org/10.1107/S0567740870003576.

[196] J. Zhang, L. Li, C. Zheng, Y. Xia, Y. Gan, H. Huang, C. Liang, X. He, X. Tao, W. Zhang, Silicon-Doped Argyrodite Solid Electrolyte Li6PS5I with Improved Ionic Conductivity and Interfacial Compatibility for High-Performance All-Solid-State Lithium Batteries, ACS Appl. Mater. Interfaces 12 (2020) 41538–41545, https://doi.org/10.1021/acsami.0c11683.

[197] S. Ohno, B. Helm, T. Fuchs, G. Dewald, M.A. Kraft, S.P. Culver, A. Senyshyn, W. G. Zeier, Further Evidence for Energy Landscape Flattening in the Superionic Argyrodites Li6+xP1–xMxS5I (M = Si, Ge, Sn), Chem. Mater. 31 (2019) 4936–4944, https://doi.org/10.1021/acs.chemmater.9b01857.

[198] J. Lin, G. Cherkashinin, M. Schäfer, G. Melinte, S. Indris, A. Kondrakov, J. Janek, T. Brezesinski, F. Strauss, A High-Entropy Multicationic Substituted Lithium Argyrodite Superionic Solid Electrolyte, ACS Mater. Lett. 4 (2022) 2187–2194, https://doi.org/10.1021/acsmaterialslett.2c00667.

[199] H.-M. Kim, Y. Subramanian, K.-S. Ryu, I-Rich Thioantimonate Argyrodite Glass-Ceramic Electrolyte with High Air Stability and Compatibility with Lithium, ACS Appl. Energy Mater. 6 (2023) 6072–6079, https://doi.org/10.1021/acsaem.3c00551.

[200] A. Behera, High Entropy Materials, in: 2022: pp. 291–320. https://doi.org/10.1007/978-3-030-80359-9_9.

[201] S.J. Sedlmaier, S. Indris, C. Dietrich, M. Yavuz, C. Dräger, F. von Seggern, H. Sommer, J. Janek, Li4PS4I: A Li+ Superionic Conductor Synthesized by a Solvent-Based Soft Chemistry Approach, Chem. Mater. 29 (2017) 1830–1835, https://doi.org/10.1021/acs.chemmater.7b00013.

[202] P. Adeli, J.D. Bazak, K.H. Park, I. Kochetkov, A. Huq, G.R. Goward, L.F. Nazar, Boosting Solid-State Diffusivity and Conductivity in Lithium Superionic Argyrodites by Halide Substitution, Angew. Chem. Int. Ed. 58 (2019) 8681–8686, https://doi.org/10.1002/anie.201814222.

[203] Y. Lee, J. Jeong, H.-D. Lim, S.-O. Kim, H.-G. Jung, K.Y. Chung, S. Yu, Superionic Si-Substituted Lithium Argyrodite Sulfide Electrolyte Li6+xSb1–xSixS5I for All-Solid-State Batteries, ACS Sustain. Chem. Eng. 9 (2021) 120–128, https://doi.org/10.1021/acssuschemeng.0c05549.

[204] L. Zhou, A. Assoud, Q. Zhang, X. Wu, L.F. Nazar, New Family of Argyrodite Thioantimonate Lithium Superionic Conductors, J. Am. Chem. Soc. 141 (2019) 19002–19013, https://doi.org/10.1021/jacs.9b08357.

[205] Y. Lee, J. Jeong, H.J. Lee, M. Kim, D. Han, H. Kim, J.M. Yuk, K.-W. Nam, K. Y. Chung, H.-G. Jung, S. Yu, Lithium Argyrodite Sulfide Electrolytes with High Ionic Conductivity and Air Stability for All-Solid-State Li-Ion Batteries, ACS Energy Lett. 7 (2022) 171–179, https://doi.org/10.1021/acsenergylett.1c02428.

[206] T. Kimura, R. Izawa, C. Hotehama, K. Fujii, A. Sakuda, M. Yashima, M. Tatsumisago, A. Hayashi, Synthesis and ionic conductivity of an argyrodite-type Li6SbS5I electrolyte, Solid State Ion.-. 399 (2023) 116287, https://doi.org/10.1016/j.ssi.2023.116287.

[207] Y. Liu, H. Peng, H. Su, Y. Zhong, X. Wang, X. Xia, C. Gu, J. Tu, Ultrafast Synthesis of I-Rich Lithium Argyrodite Glass–Ceramic Electrolyte with High Ionic Conductivity, Adv. Mater. 34 (2022) 2107346, https://doi.org/10.1002/adma.202107346.

[208] Z. Zhang, C. Yu, R. Xu, L. Peng, H. Ren, J. Zhang, L. Zhang, S. Cheng, J. Xie, Iodine-rich lithium argyrodite with enhanced ionic conductivity for solid-state batteries, Scr. Mater. 210 (2022) 114475, https://doi.org/10.1016/j.scriptamat.2021.114475.

[209] Y. Seino, T. Ota, K. Takada, A. Hayashi, M. Tatsumisago, A sulphide lithium super ion conductor is superior to liquid ion conductors for use in rechargeable batteries, Energy Environ. Sci. 7 (2014) 627–631, https://doi.org/10.1039/C3EE41655K.

[210] Y. Sun, K. Suzuki, S. Hori, M. Hirayama, R. Kanno, Superionic Conductors: $Li_{10+\delta}[Sn_ySi_{1-y}]_{1+\delta}P_{2-\delta}S_{12}$ with a $Li_{10}GeP_2S_{12}$-type Structure in the Li_3PS_4–Li_4SnS_4–Li_4SiS_4 Quasi-ternary System, Chem. Mater. 29 (2017) 5858–5864, https://doi.org/10.1021/acs.chemmater.7b00886.

[211] J.A. Dawson, P. Canepa, T. Famprikis, C. Masquelier, M.S. Islam, Atomic-Scale Influence of Grain Boundaries on Li-Ion Conduction in Solid Electrolytes for All-Solid-State Batteries, J. Am. Chem. Soc. 140 (2018) 362–368, https://doi.org/10.1021/jacs.7b10593.

[212] S. Ganapathy, C. Yu, E.R.H. van Eck, M. Wagemaker, Peeking across Grain Boundaries in a Solid-State Ionic Conductor, ACS Energy Lett. 4 (2019) 1092–1097, https://doi.org/10.1021/acsenergylett.9b00610.

[213] A. Sakuda, A. Hayashi, M. Tatsumisago, Sulfide Solid Electrolyte with Favorable Mechanical Property for All-Solid-State Lithium Battery, Sci. Rep. 3 (2013) 2261, https://doi.org/10.1038/srep02261.

[214] A. Sakuda, A. Hayashi, Y. Takigawa, K. Higashi, M. Tatsumisago, Evaluation of elastic modulus of Li_2S–P_2S_5 glassy solid electrolyte by ultrasonic sound velocity measurement and compression test, J. Ceram. Soc. Jpn. 121 (2013) 946–949, https://doi.org/10.2109/jcersj2.121.946.

[215] Y. Kato, S. Hori, T. Saito, K. Suzuki, M. Hirayama, A. Mitsui, M. Yonemura, H. Iba, R. Kanno, High-power all-solid-state batteries using sulfide superionic conductors, Nat. Energy 1 (2016) 1–7, https://doi.org/10.1038/nenergy.2016.30.

[216] S.V. Patel, S. Banerjee, H. Liu, P. Wang, P.-H. Chien, X. Feng, J. Liu, S.P. Ong, Y.-Y. Hu, Tunable Lithium-Ion Transport in Mixed-Halide Argyrodites Li6–xPS5–xClBrx: An Unusual Compositional Space, Chem. Mater. 33 (2021) 1435–1443, https://doi.org/10.1021/acs.chemmater.0c04650.

[217] W.D. Jung, J.-S. Kim, S. Choi, S. Kim, M. Jeon, H.-G. Jung, K.Y. Chung, J.-H. Lee, B.-K. Kim, J.-H. Lee, H. Kim, Superionic Halogen-Rich Li-Argyrodites Using In Situ Nanocrystal Nucleation and Rapid Crystal Growth, Nano Lett. 20 (2020) 2303–2309, https://doi.org/10.1021/acs.nanolett.9b04597.

[218] Z.A. Grady, C.J. Wilkinson, C.A. Randall, J.C. Mauro, Emerging Role of Non-crystalline Electrolytes in Solid-State Battery Research, Front. Energy Res. 8 (2020). ⟨https://www.frontiersin.org/articles/10.3389/fenrg.2020.00218⟩ (accessed February 5, 2024).

[219] C. Yu, F. Zhao, J. Luo, L. Zhang, X. Sun, Recent development of lithium argyrodite solid-state electrolytes for solid-state batteries: Synthesis, structure, stability and dynamics, Nano Energy 83 (2021) 105858, https://doi.org/10.1016/j.nanoen.2021.105858.

[220] W.D. Jung, J.-S. Kim, Y.J. Kim, H. Jeong, D. Han, K.-W. Nam, D. Ahn, D.-H. Kwon, H.-G. Jung, J.-H. Lee, H. Kim, Annealing-Free Thioantimonate Argyrodites with High Li-Ion Conductivity and Low Elastic Modulus, Adv. Funct. Mater. 33 (2023) 2211185, https://doi.org/10.1002/adfm.202211185.

[221] H. Kim, H. Kim, Z. Ding, M.H. Lee, K. Lim, G. Yoon, K. Kang, Recent Progress in Electrode Materials for Sodium-Ion Batteries, Adv. Energy Mater. 6 (2016) 1600943, https://doi.org/10.1002/aenm.201600943.

[222] S.-W. Kim, D.-H. Seo, X. Ma, G. Ceder, K. Kang, Electrode Materials for Rechargeable Sodium-Ion Batteries: Potential Alternatives to Current Lithium-Ion Batteries, Adv. Energy Mater. 2 (2012) 710–721, https://doi.org/10.1002/aenm.201200026.

[223] X. Zhu, S.V. Savilov, J. Ni, L. Li, Carbon nanoflakes as a promising anode for sodium-ion batteries, Funct. Mater. Lett. 11 (2018) 1840011, https://doi.org/10.1142/S1793604718400118.

[224] C. Li, R. Li, K. Liu, R. Si, Z. Zhang, Y.-S. Hu, NaSICON: A promising solid electrolyte for solid-state sodium batteries, Interdiscip. Mater. 1 (2022) 396–416, https://doi.org/10.1002/idm2.12044.

[225] N. Yabuuchi, K. Kubota, M. Dahbi, S. Komaba, Research Development on Sodium-Ion Batteries, Chem. Rev. 114 (2014) 11636–11682, https://doi.org/10.1021/cr500192f.

[226] C. Cao, Z.-B. Li, X.-L. Wang, X.-B. Zhao, W.-Q. Han, Recent Advances in Inorganic Solid Electrolytes for Lithium Batteries, Front. Energy Res. 2 (2014). ⟨https://www.frontiersin.org/articles/10.3389/fenrg.2014.00025⟩ (accessed February 18, 2024).

[227] A. Hayashi, K. Noi, A. Sakuda, M. Tatsumisago, Superionic glass-ceramic electrolytes for room-temperature rechargeable sodium batteries, Nat. Commun. 3 (2012) 856, https://doi.org/10.1038/ncomms1843.

[228] S.Ping Ong, Y. Mo, W.Davidson Richards, L. Miara, H.Sug Lee, G. Ceder, Phase stability, electrochemical stability and ionic conductivity of the Li 10±1 MP 2 X 12 (M = Ge, Si, Sn, Al or P, and X = O, S or Se) family of superionic conductors, Energy Environ. Sci. 6 (2013) 148–156, https://doi.org/10.1039/C2EE23355J.

[229] V.S. Kandagal, M.Dixit Bharadwaj, U.V. Waghmare, Theoretical prediction of a highly conducting solid electrolyte for sodium batteries: Na 10 GeP 2 S 12, J. Mater. Chem. A 3 (2015) 12992–12999, https://doi.org/10.1039/C5TA01616A.

[230] W.D. Richards, T. Tsujimura, L.J. Miara, Y. Wang, J.C. Kim, S.P. Ong, I. Uechi, N. Suzuki, G. Ceder, Design and synthesis of the superionic conductor Na10SnP2S12, Nat. Commun. 7 (2016) 11009, https://doi.org/10.1038/ncomms11009.

[231] F. Tsuji, N. Tanibata, A. Sakuda, A. Hayashi, M. Tatsumisago, Preparation of Sodium Ion Conductive Na10GeP2S12 Glass-ceramic Electrolytes, Chem. Lett. 47 (2018) 13–15, https://doi.org/10.1246/cl.170836.

[232] A. Nasu, T. Inaoka, F. Tsuji, K. Motohashi, A. Sakuda, M. Tatsumisago, A. Hayashi, Formation of Passivate Interphases by Na3BS3-Glass Solid Electrolytes in All-Solid-State Sodium-Metal Batteries, ACS Appl. Mater. Interfaces 14 (2022) 24480–24485, https://doi.org/10.1021/acsami.2c05090.

[233] L. Zhou, J.D. Bazak, B. Singh, C. Li, A. Assoud, N.M. Washton, V. Murugesan, L.F. Nazar, A New Sodium Thioborate Fast Ion Conductor: Na3B5S9, (n.d.). https://doi.org/10.1002/ange.202300404.

[234] B. Ouyang, Y. Wang, Y. Sun, G. Ceder, Computational Investigation of Halogen-Substituted Na Argyrodites as Solid-State Superionic Conductors, Chem. Mater. 32 (2020) 1896–1903, https://doi.org/10.1021/acs.chemmater.9b04541.

[235] N.J.J. de Klerk, M. Wagemaker, Diffusion Mechanism of the Sodium-Ion Solid Electrolyte Na3PS4 and Potential Improvements of Halogen Doping, Chem. Mater. 28 (2016) 3122–3130, https://doi.org/10.1021/acs.chemmater.6b00698.

[236] Y. Wang, G. Li, K. Shen, E. Tian, The effect of grain boundary on Na ion transport in polycrystalline solid-state electrolyte cubic Na 3 PS 4, Mater. Res. Express 8 (2021), https://doi.org/10.1088/2053-1591/abe7b1.

[237] T. Krauskopf, C. Pompe, M.A. Kraft, W.G. Zeier, Influence of Lattice Dynamics on Na+ Transport in the Solid Electrolyte Na3PS4–xSex, Chem. Mater. 29 (2017) 8859–8869, https://doi.org/10.1021/acs.chemmater.7b03474.

[238] I.-H. Chu, C.S. Kompella, H. Nguyen, Z. Zhu, S. Hy, Z. Deng, Y.S. Meng, S.P. Ong, Room-Temperature All-solid-state Rechargeable Sodium-ion Batteries with a Cl-doped Na3PS4 Superionic Conductor, Sci. Rep. 6 (2016) 33733, https://doi.org/10.1038/srep33733.

[239] H. Huang, H.-H. Wu, X. Wang, B. Huang, T.-Y. Zhang, Enhancing sodium ionic conductivity in tetragonal-Na3PS4 by halogen doping: a first principles investigation, Phys. Chem. Chem. Phys. 20 (2018) 20525–20533, https://doi.org/10.1039/C8CP02383B.

[240] X. Feng, P.-H. Chien, Z. Zhu, I.-H. Chu, P. Wang, M. Immediato-Scuotto, H. Arabzadeh, S.P. Ong, Y.-Y. Hu, Studies of Functional Defects for Fast Na-Ion Conduction in Na3−yPS4−xClx with a Combined Experimental and Computational Approach, Adv. Funct. Mater. 29 (2019) 1807951, https://doi.org/10.1002/adfm.201807951.

[241] C.K. Moon, H.-J. Lee, K.H. Park, H. Kwak, J.W. Heo, K. Choi, H. Yang, M.-S. Kim, S.-T. Hong, J.H. Lee, Y.S. Jung, Vacancy-Driven Na+ Superionic Conduction in New Ca-Doped Na3PS4 for All-Solid-State Na-Ion Batteries, ACS Energy Lett. 3 (2018) 2504–2512, https://doi.org/10.1021/acsenergylett.8b01479.

[242] S.-H. Bo, Y. Wang, G. Ceder, Structural and Na-ion conduction characteristics of Na 3 PS x Se 4−x, J. Mater. Chem. A 4 (2016) 9044–9053, https://doi.org/10.1039/C6TA03027K.

[243] T. Krauskopf, S. Muy, S.P. Culver, S. Ohno, O. Delaire, Y. Shao-Horn, W.G. Zeier, Comparing the Descriptors for Investigating the Influence of Lattice Dynamics on Ionic Transport Using the Superionic Conductor Na3PS4–xSex, J. Am. Chem. Soc. 140 (2018) 14464–14473, https://doi.org/10.1021/jacs.8b09340.

[244] L. Zhang, K. Yang, J. Mi, L. Lu, L. Zhao, L. Wang, Y. Li, H. Zeng, Solid Electrolytes: Na3PSe4: A Novel Chalcogenide Solid Electrolyte with High Ionic Conductivity (Adv. Energy Mater. 24/2015), Adv. Energy Mater. 5 (2015), https://doi.org/10.1002/aenm.201570133.

[245] N. Wang, K. Yang, L. Zhang, X. Yan, L. Wang, B. Xu, Improvement in ion transport in Na3PSe4–Na3SbSe4 by Sb substitution, J. Mater. Sci. 53 (2018) 1987–1994, https://doi.org/10.1007/s10853-017-1618-0.

[246] P. Till, M.T. Agne, M.A. Kraft, M. Courty, T. Famprikis, M. Ghidiu, T. Krauskopf, C. Masquelier, W.G. Zeier, Two-Dimensional Substitution Series Na3P1−xSbxS4−ySey: Beyond Static Description of Structural Bottlenecks for Na+ Transport, Chem. Mater. 34 (2022) 2410–2421, https://doi.org/10.1021/acs.chemmater.1c04445.

[247] N. Tanibata, K. Noi, A. Hayashi, N. Kitamura, Y. Idemoto, M. Tatsumisago, X-ray Crystal Structure Analysis of Sodium-Ion Conductivity in 94 Na3PS4⋅6 Na4SiS4 Glass-Ceramic Electrolytes, ChemElectroChem 1 (2014) 1130–1132, https://doi.org/10.1002/celc.201402016.

[248] N. Tanibata, K. Noi, A. Hayashi, M. Tatsumisago, Preparation and characterization of Na3PS4–Na4GeS4 glass and glass-ceramic electrolytes, Solid State Ion.-. 320 (2018) 193–198, https://doi.org/10.1016/j.ssi.2018.02.042.

[249] R.Prasada Rao, H. Chen, L.Loong Wong, S. Adams, Na 3+x M x P 1−x S 4 (M = Ge 4+, Ti 4+, Sn 4+) enables high rate all-solid-state Na-ion batteries Na 2+2δ Fe 2−δ (SO 4) 3 |Na 3+x M x P 1−x S 4 |Na 2 Ti 3O 7, J. Mater. Chem. A 5 (2017) 3377–3388, https://doi.org/10.1039/C6TA09809F.

[250] Z. Zhu, I.-H. Chu, Z. Deng, S.P. Ong, Role of Na+ Interstitials and Dopants in Enhancing the Na+ Conductivity of the Cubic Na3PS4 Superionic Conductor, Chem. Mater. 27 (2015) 8318–8325, https://doi.org/10.1021/acs.chemmater.5b03656.

[251] K.H. Park, D.H. Kim, H. Kwak, S.H. Jung, H.-J. Lee, A. Banerjee, J.H. Lee, Y.S. Jung, Solution-derived glass-ceramic NaI⋅Na3SbS4 superionic conductors for all-solid-state Na-ion batteries, J. Mater. Chem. A 6 (2018) 17192–17200, https://doi.org/10.1039/C8TA05537H.

[252] H. Cao, M. Yu, L. Zhang, Z. Zhang, X. Yan, P. Li, C. Yu, Stabilizing Na3SbS4/Na interface by rational design via Cl doping and aqueous processing, J. Mater. Sci. Technol. 70 (2021) 168–175, https://doi.org/10.1016/j.jmst.2020.08.035.

[253] T. Fuchs, S.P. Culver, P. Till, W.G. Zeier, Defect-Mediated Conductivity Enhancements in Na3−xPn1−xWxS4 (Pn = P, Sb) Using Aliovalent Substitutions, ACS Energy Lett. 5 (2020) 146–151, https://doi.org/10.1021/acsenergylett.9b02537.

[254] F. Tsuji, A. Nasu, A. Sakuda, M. Tatsumisago, A. Hayashi, Mechanochemical synthesis and characterization of Na3−xP1−xWxS4 solid electrolytes, J. Power Sources 506 (2021) 230100, https://doi.org/10.1016/j.jpowsour.2021.230100.

[255] C.-W. Lee, M. Maegawa, H. Akamatsu, K. Hayashi, S. Ohno, P. Gorai, Local and Global Structural Effects of Doping on Ionic Conductivity in Na3SbS4 Solid Electrolyte, (2024). https://doi.org/10.26434/chemrxiv-2024-v52q7.

[256] Y. He, F. Lu, X. Kuang, Enhanced sodium ion conductivity in Na 3 VS 4 by P-doping, RSC Adv. 9 (2019) 39180–39186, https://doi.org/10.1039/C9RA08900D.

[257] R. Niewa, G.V. Vajenine, F.J. DiSalvo, Synthesis and Crystal Structure of Ternary Sulfides*A*3*M*S4withA=Na, Rb andM=Nb, Ta, J. Solid State Chem. 139 (1998) 404–411, https://doi.org/10.1006/jssc.1998.7872.

[258] S. Herzog, C. Näther, P. Dürichen, W. Bensch, Synthesis and Crystal Structure of a New Alkali Metal Tantalum Sulfide: Na3TaS4, Z. F. üR. Anorg. Allg. Chem. 624 (1998) 2021–2024, https://doi.org/10.1002/(SICI)1521-3749(1998120)624:12<2021::AID-ZAAC2021>3.0.CO;2-0.

[259] Y. Zeng, B. Ouyang, J. Liu, Y.-W. Byeon, Z. Cai, L.J. Miara, Y. Wang, G. Ceder, High-entropy mechanism to boost ionic conductivity, Science 378 (2022) 1320–1324, https://doi.org/10.1126/science.abq1346.

[260] A. Hayashi, N. Masuzawa, S. Yubuchi, F. Tsuji, C. Hotehama, A. Sakuda, M. Tatsumisago, A sodium-ion sulfide solid electrolyte with unprecedented conductivity at room temperature, Nat. Commun. 10 (2019) 5266, https://doi.org/10.1038/s41467-019-13178-2.

[261] H. Wang, Y. Chen, Z.D. Hood, G. Sahu, A.S. Pandian, J.K. Keum, K. An, C. Liang, An Air-Stable Na3SbS4 Superionic Conductor Prepared by a Rapid and Economic Synthetic Procedure, Angew. Chem. 128 (2016) 8693–8697, https://doi.org/10.1002/ange.201601546.

[262] L. Zhang, D. Zhang, K. Yang, X. Yan, L. Wang, J. Mi, B. Xu, Y. Li, Vacancy-Contained Tetragonal Na3SbS4 Superionic Conductor, Adv. Sci. 3 (2016) 1600089, https://doi.org/10.1002/advs.201600089.

[263] A. Banerjee, K.H. Park, J.W. Heo, Y.J. Nam, C.K. Moon, S.M. Oh, S.-T. Hong, Y.S. Jung, Na3SbS4: A Solution Processable Sodium Superionic Conductor for All-Solid-State Sodium-Ion Batteries, Angew. Chem. 128 (2016) 9786–9790, https://doi.org/10.1002/ange.201604158.

[264] Y. Yan, Y. Guo, H. Zheng, L. Qi, Y. Yang, Y. Miao, X. Shi, L. Zhang, C. Li, D. Song, A simple approach through reduction of Na2SO4 to prepare high-purity Na2S for sulfide electrolytes toward all-solid-state sodium batteries, J. Power Sources 620 (2024) 235264, https://doi.org/10.1016/j.jpowsour.2024.235264.

[265] G. Liu, J. Yang, J. Wu, Z. Peng, X. Yao, Inorganic Sodium Solid Electrolytes: Structure Design, Interface Engineering and Application, Adv. Mater. n/a (n.d.) 2311475. https://doi.org/10.1002/adma.202311475.

[266] Z. Yu, S.-L. Shang, J.-H. Seo, D. Wang, X. Luo, Q. Huang, S. Chen, J. Lu, X. Li, Z.-K. Liu, D. Wang, Exceptionally High Ionic Conductivity in Na3P0.62As0.38S4 with Improved Moisture Stability for Solid-State Sodium-Ion Batteries, Adv. Mater. 29 (2017) 1605561, https://doi.org/10.1002/adma.201605561.

[267] S.-L. Shang, Z. Yu, Y. Wang, D. Wang, Z.-K. Liu, Origin of Outstanding Phase and Moisture Stability in a Na3P1−xAsxS4 Superionic Conductor, ACS Appl. Mater. Interfaces 9 (2017) 16261–16269, https://doi.org/10.1021/acsami.7b03606.

[268] J. Yin, L. Yu, Z. Gong, L. Shu, C. Gao, Y. Liu, X. Shen, C. Lin, Q. Jiao, Double regulatory effect of As-designed Na3Sb1-xAsxS4 sodium superionic conductors, J. Am. Ceram. Soc. 107 (2024) 1315–1323, https://doi.org/10.1111/jace.19487.

[269] L. Yu, Q. Jiao, B. Liang, H. Shan, C. Lin, C. Gao, X. Shen, S. Dai, Exceptionally high sodium ion conductivity and enhanced air stability in Na3SbS4 via germanium doping, J. Alloy. Compd. 913 (2022) 165229, https://doi.org/10.1016/j.jallcom.2022.165229.

[270] J. Lu, L. Shu, B. Liang, Y. Shen, T. Huan, Y. Liu, X. Zhou, Y. Yang, C. Lin, B. Wang, Q. Jiao, Economical sodium source prepared Na3SbS4 electrolyte with improved electrochemical performance by La doping, Ceram. Int. 50 (2024) 21800–21807, https://doi.org/10.1016/j.ceramint.2024.03.292.

[271] Y. Fu, Z. Gong, D. Li, Y. Liu, X. Zhou, Y. Yang, Q. Jiao, Zn doping for enhanced sodium-ion conductivity and air stability in Na3SbS4 solid electrolyte, J. Mater. Sci. 59 (2024) 3009–3017, https://doi.org/10.1007/s10853-023-09263-z.

[272] X. Feng, H. Fang, P. Liu, N. Wu, E.C. Self, L. Yin, P. Wang, X. Li, P. Jena, J. Nanda, D. Mitlin, Heavily Tungsten-Doped Sodium Thioantimonate Solid-State Electrolytes with Exceptionally Low Activation Energy for Ionic Diffusion, Angew. Chem. 133 (2021) 26362–26370, https://doi.org/10.1002/ange.202110699.

[273] M. Ravalli, M. Soleimanzade, M. Scavini, S.Chiara Tarantino, M. Radaelli, C. Tealdi, Unveiling the relationship between polymorphism and ionic conductivity in Na 3−x Sb 1−x W x S 4 solid electrolyte for Na-ion batteries, J. Mater. Chem. A (2024), https://doi.org/10.1039/D4TA04541F.

[274] C. He, C. Gao, J. Zhang, X. Li, T. Zhou, W. Tao, S. Kang, L. Tan, Q. Jiao, S. Dai, C. Lin, Valence state of Mo and electrochemical properties of Na3-2xSb1-xMoxS4-xIx based solid-state electrolytes, Ceram. Int. 50 (2024) 2541–2548, https://doi.org/10.1016/j.ceramint.2023.07.137.

[275] S. Yubuchi, A. Ito, N. Masuzawa, A. Sakuda, A. Hayashi, M. Tatsumisago, Aqueous solution synthesis of Na3SbS4–Na2WS4 superionic conductors, J. Mater. Chem. A 8 (2020) 1947–1954, https://doi.org/10.1039/C9TA02246E.

[276] J.A.S. Oh, L. He, B. Chua, K. Zeng, L. Lu, Inorganic sodium solid-state electrolyte and interface with sodium metal for room-temperature metal solid-state batteries, Energy Storage Mater. 34 (2021) 28–44, https://doi.org/10.1016/j.ensm.2020.08.037.

[277] B. Tang, P.W. Jaschin, X. Li, S.-H. Bo, Z. Zhou, Critical interface between inorganic solid-state electrolyte and sodium metal, Mater. Today 41 (2020) 200–218, https://doi.org/10.1016/j.mattod.2020.08.016.

[278] S. Lou, F. Zhang, C. Fu, M. Chen, Y. Ma, G. Yin, J. Wang, Interface Issues and Challenges in All-Solid-State Batteries: Lithium, Sodium, and Beyond, Adv. Mater. 33 (2021) 2000721, https://doi.org/10.1002/adma.202000721.

[279] Y. Zhu, X. He, Y. Mo, Origin of Outstanding Stability in the Lithium Solid Electrolyte Materials: Insights from Thermodynamic Analyses Based on First-Principles Calculations, ACS Appl. Mater. Interfaces 7 (2015) 23685–23693, https://doi.org/10.1021/acsami.5b07517.

[280] S. Wenzel, T. Leichtweiss, D.A. Weber, J. Sann, W.G. Zeier, J. Janek, Interfacial Reactivity Benchmarking of the Sodium Ion Conductors Na3PS4 and Sodium β-Alumina for Protected Sodium Metal Anodes and Sodium All-Solid-State Batteries, ACS Appl. Mater. Interfaces 8 (2016) 28216–28224, https://doi.org/10.1021/acsami.6b10119.

[281] G. Deysher, Y.-T. Chen, B. Sayahpour, S.W.-H. Lin, S.-Y. Ham, P. Ridley, A. Cronk, E.A. Wu, D.H.S. Tan, J.-M. Doux, J.A.S. Oh, J. Jang, L.H.B. Nguyen, Y.S. Meng, Evaluating Electrolyte–Anode Interface Stability in Sodium All-Solid-State Batteries, ACS Appl. Mater. Interfaces 14 (2022) 47706–47715, https://doi.org/10.1021/acsami.2c12759.

[282] E.A. Wu, C.S. Kompella, Z. Zhu, J.Z. Lee, S.C. Lee, I.-H. Chu, H. Nguyen, S.P. Ong, A. Banerjee, Y.S. Meng, New Insights into the Interphase between the Na Metal Anode and Sulfide Solid-State Electrolytes: A Joint Experimental and Computational Study, ACS Appl. Mater. Interfaces 10 (2018) 10076–10086, https://doi.org/10.1021/acsami.7b19037.

[283] P. Hu, Y. Zhang, X. Chi, K. Kumar Rao, F. Hao, H. Dong, F. Guo, Y. Ren, L. C. Grabow, Y. Yao, Stabilizing the Interface between Sodium Metal Anode and Sulfide-Based Solid-State Electrolyte with an Electron-Blocking Interlayer, ACS Appl. Mater. Interfaces 11 (2019) 9672–9678, https://doi.org/10.1021/acsami.8b19984.

[284] Y. Li, S. Halacoglu, V. Shreyas, W. Arnold, X. Guo, Q. Dou, J.B. Jasinski, B. Narayanan, H. Wang, Highly efficient interface stabilization for ambient-temperature quasi-solid-state sodium metal batteries, Chem. Eng. J. 434 (2022) 134679, https://doi.org/10.1016/j.cej.2022.134679.

[285] Y. Li, W. Arnold, S. Halacoglu, J.B. Jasinski, T. Druffel, H. Wang, Phase-Transition Interlayer Enables High-Performance Solid-State Sodium Batteries with Sulfide Solid Electrolyte, Adv. Funct. Mater. 31 (2021) 2101636, https://doi.org/10.1002/adfm.202101636.

[286] X. Xu, Y. Li, J. Cheng, G. Hou, X. Nie, Q. Ai, L. Dai, J. Feng, L. Ci, Composite solid electrolyte of Na3PS4-PEO for all-solid-state SnS2/Na batteries with excellent interfacial compatibility between electrolyte and Na metal, J. Energy Chem. 41 (2020) 73–78, https://doi.org/10.1016/j.jechem.2019.05.003.

[287] S. Choudhury, Designing Solid-Liquid Interphases for Sodium Batteries, in: S. Choudhury (Ed.), Ration. Des. Nanostructured Polym. Electrolytes Solid–Liquid Interphases Lithium Batter., Springer International Publishing, Cham, 2019, pp. 95–116, https://doi.org/10.1007/978-3-030-28943-0_6.

[288] M. Lazar, S. Kmiec, A. Joyce, S.W. Martin, Investigations into Reactions between Sodium Metal and Na3PS4–xOx Solid-State Electrolytes: Enhanced Stability of the Na3PS3O Solid-State Electrolyte, ACS Appl. Energy Mater. 3 (2020) 11559–11569, https://doi.org/10.1021/acsaem.0c00914.

[289] X. Chi, Y. Zhang, F. Hao, S. Kmiec, H. Dong, R. Xu, K. Zhao, Q. Ai, T. Terlier, L. Wang, L. Zhao, L. Guo, J. Lou, H.L. Xin, S.W. Martin, Y. Yao, An electrochemically stable homogeneous glassy electrolyte formed at room temperature for all-solid-state sodium batteries, Nat. Commun. 13 (2022) 2854, https://doi.org/10.1038/s41467-022-30517-y.

[290] W. Weng, G. Liu, Y. Li, L. Shen, X. Yao, Tungsten and oxygen co-doped stable tetragonal phase Na3SbS4 with ultrahigh ionic conductivity for all-solid-state sodium batteries, Appl. Mater. Today 27 (2022) 101448, https://doi.org/10.1016/j.apmt.2022.101448.

Mohammad Sufiyan Nafis earned his bachelor's degree from Aligarh Muslim University and an M.S. degree in Mechanical Engineering from the University of Colorado, Boulder. He is currently pursuing a Ph.D. in Mechanical Engineering under Dr. Se-Hee Lee and Dr. Chunmei Ban at the University of Colorado Boulder, specializing in solid-state battery materials for cathodes, solid electrolytes, and anodes for all-solid-state-batteries.

Zhiming Liang earned his bachelor's degree from Sichuan University, China, and his Ph.D. in physical chemistry from the University of Kentucky, USA. He is currently a research associate at the University of Colorado Boulder. His research focuses on redox flow batteries, lithium (sodium)-ion batteries, and solid-state batteries.

Sehee Lee received his B.S., M.S. and Ph.D. (1997), all in materials science and engineering, from Seoul National University in Korea. He was a post-doctoral fellow, scientist, senior scientist at National Renewable Energy Laboratory from 1997-2007 before joining the department of mechanical engineering at the University of Colorado at Boulder in 2007. His research efforts have concentrated on the investigation of the electrochemical properties of nanostructured materials as well as their micro-structural characteristics.

Chunmei Ban is an Associate Professor at the Paul M. Rady Department of Mechanical Engineering and affiliated with Materials Science and Engineering Program at University of Colorado Boulder, Boulder, CO. Prior to 2019, Ban was a Senior Scientist (V) in the Chemistry and Nanoscience Center at National Renewable Energy Laboratory (NREL), Golden, CO, has led DOE-awarded projects in intermetallic anodes, high-energy cathodes, and direct recycling process for battery materials. Ban received a Bachelor's and Master's degree from the Department of Chemical Engineering from Tianjin University, China and holds a PhD in Chemistry from the State University of New York at Binghamton, supervised by Prof. M Stanley Whittingham, a 2019 Nobel Laureate in Chemistry. Her current research efforts revolve around enhancing the fundamental understanding of chemical and physical properties during the electrochemical process, with the aim of developing next-generation electrochemical materials for energy storage applications.